# Biodiesel Spray Characterization: A Combined Numerical and Experimental Analysis

EHSAN FARVARDIN

A Thesis

in

the Department

of

Mechanical and Industrial Engineering

Presented in Partial Fulfillment of the Requirements
for the Degree of Doctor of Philosophy (Mechanical Engineering) at
Concordia University
Montreal, Quebec, Canada

August 2013

**CONCORDIA UNIVERSITY**

**SCHOOL OF GRADUATE STUDIES**

This is to certify that the thesis prepared

By: **Ehsan Farvardin**

Entitled: **Biodiesel Spray Characterization: A Combined Numerical and Experimental Analysis**

and submitted in partial fulfillment of the requirements for the degree of

DOCTOR OF PHILOSOPHY (Mechanical Engineering)

complies with the regulations of the University and meets the accepted standards with respect to originality and quality.

Signed by the final examining committee:

_____ Chair
Dr. A. Ben Hamza

_____ External Examiner
Dr. M. Birouk

_____ External to Program
Dr. F. Haghighat

_____ Examiner
Dr. H.D. Ng

_____ Examiner
Dr. L. Kadem

_____ Thesis Supervisor
Dr. A. Dolatabadi

Approved by _____
Dr. A. Dolatabadi, Graduate Program Director

September 12, 2013

_____
Dr. C. Trueman, Interim Dean
Faculty of Engineering & Computer Science

# Abstract

**BIODIESEL SPRAY CHARACTERIZATION: A COMBINED NUMERICAL AND EXPERIMENTAL ANALYSIS**

Ehsan Farvardin, Ph.D.

Concordia University, 2013

A fundamental study on the characteristics of biodiesel spray is performed and compared with diesel spray at the same condition. In this vein, the liquid jet in cross flow problem is applied to compare the spray penetration depth, droplet size distribution, spatial flux distribution and breakup study of biodiesel, diesel and their blends. Both experimental and numerical analyses have been performed to shed more light on the physics of atomization of liquid jets in cross flow.

In the experimental part, shadowgraph technique and image processing have been used in order to capture the penetration of the spray. In addition, droplet size measurement and spatial flux distribution are found by using Phase Doppler Particle Analysis (PDPA). The experimental study shows less penetration depth for biodiesel in comparison with diesel. On the other hand, the droplets' mass flux distribution with biodiesel is less in the vicinity of the windward side of the spray. In the numerical part of this work, the near field of the injection is simulated using Volume of Fluid (VOF) coupled with the Large Eddy Simulation (LES) turbulence model. As a result a considerable dissimilarity has been found between the breakup regime of biodiesel and diesel. Namely, at Weber numbers of above 40, where the breakup regime of most liquids

including diesel occurs in atomization mode, the breakup regime of biodiesel is bag breakup. The main cause of this behavior can be attributed to the remarkably higher viscosity of biodiesel compared with many conventional fuels.

The geometry of the orifice can play an important role in controlling the atomization parameters. In this vein, elliptical jets with various aspect ratios between 1 (circular) and 3.85 is performed for several Weber numbers, ranging from 15 to 330. The elliptical jet is first characterized in free air in order to find its capillary behavior in Rayleigh instability regime. The axis-switching phenomenon and breakup length of the jets are the important parameters characterized in this research. Second, the elliptical jets in crossflow are simulated to find differences from the circular orifices in terms of penetration depth, surface waves and breakup length. The simulations of elliptical jets in crossflow were performed with relative gas–liquid Weber numbers of 11, 18 and 30, which cover the bag and multimode primary breakup regime in crossflow. The results show remarkable changes in liquid shapes before disintegration for different aspect ratios.

# Acknowledgements

I would like to, cordially, thank my supervisor Dr. Ali Dolatabadi for his helpful ideas, comments and supports during my PhD. His precious advice directed me towards my goals and results. I would also like to acknowledge Rolls Royce Canada, CRIAQ and NSERC for their financial support to several parts of this study. Especially, I thank Dr. Michael Johnson, Dr. Gilles Bourque and Dr. Rabi Tahir from Rolls Royce Canada and Dr. Alain de Champlain from University of Laval. Their helpful comments, regular meetings and their ideas enriched this study remarkably. I appreciate my committee members for their useful feedback during my proposal, which led me to define attainable and invaluable scientific milestones during the course of PhD. Hardworking of my colleagues, Hadi Alaee and Alfredo Martinez really facilitated the experimental work conditions. Their efforts and contributions are much appreciated. Furthermore trainings of my colleague, Khalid Koraitem, taught me the details of laser diagnostics. Courtesy of Dr. Ghobad Amini for using some of his experimental images, is acknowledged. Finally and most importantly, I would like to, warmly, appreciate my wife, Shima Ashouri for her priceless support during the last years.

# Table of Contents

# List of Figures

# List of Tables

# Nomenclature

$A$ = cross sectional area of the jet ($m^2$)

$AR$ = nozzle cross section aspect ratio ($b/a$)

$a$ = nozzle diameter parallel to the gas flow (m)

$b$ = nozzle diameter normal to the gas flow (m)

$C_\alpha$ = compression coefficient

$C_\varepsilon$ = constant value in Equation 3.10, Equation 4.14

$C_k$ = constant value in Equation 3.11, Equation 4.15

$D_{eq}$ = diameter of equal area circle, $\sqrt{\frac{4A}{\pi}}$ (m)

$D_{32}$ = Sauter mean diameter (m)

$d$ = jet diameter (m)

$F$ = surface tension force (N)

$Fr$ = Froude number ($V^2/gL$)

$I$ = turbulence intensity

$k_{sgs}$ = subgrid scale turbulent kinetic energy ($m^2/s^2$)

$L$ = liquid jet characteristic length, i.e. jet diameter (m)

$n_f$ = cell unit normal vector

$Oh$ = Ohnesorge number, ($\frac{\mu_l}{\sqrt{\rho_l \sigma L}}$)

$Q$ = gas to liquid density ratio ($\rho_g / \rho_l$)

$q$ = momentum flux ratio ( $\rho_l V_l^2 / \rho_g V_g^2$ )

$\bar{S}$ = mean strain rate (1/s)

$S_f$ = cell area vector ($m^2$)

$T_g$ = gas temperature (K)

$V_g$ = gas velocity (m/s)

$V_l$ = liquid velocity (m/s)

$v_r$ = compression velocity (m/s)

$We$ = liquid Weber number ( $\rho_l D_{eq} V_l^2 / \sigma$ )

$We_g$ = cross flow Weber number based on gas properties ( $\rho_g D_{eq} V_g^2 / \sigma$ )

$Z_b$ = breakup length of liquid jet (m)

$x$ = horizontal location (m)

$y$ = vertical location (m)

$\alpha$ = liquid to gas volume fraction

$\delta_n$ = constant in Equation 3.15, Equation 4.10

$\Delta$ = characteristic grid width (m)

$\varepsilon$ = turbulent energy dissipation rate ($m^2/s^3$)

$\varphi$ = face volume flux ($m^3/s$)

$\kappa$ = interface curvature

$\mu_g$ = gas viscosity (kg/s.m)

$\mu_l$ = liquid viscosity (kg/s.m)

$v_{sgs}$ = subgrid scale kinematic eddy viscosity ($m^2/s$)

$\lambda_{as}$ = axis-switching wavelength (m)

$\rho_g$ = gas density ($kg/m^3$)

$\rho_l$ = liquid density ($kg/m^3$)

$\sigma$ = gas-liquid surface tension (N/m)

## Chapter 1

# Introduction

Nowadays, high price of fuel, climatic change and air pollution are crucial problems facing the world. Several governments, industries and researchers have addressed the use of biofuels as a firm and attainable solution in the past decades [1]. Biofuel, practically, is defined as a fuel derived from biological materials, such as dead organisms or by-products of living organisms. In theory, biofuels are defined as fuels that gain their energy from a process called carbon fixation. Carbon fixation is the process of converting inorganic carbons (i.e., $CO_2$) to organic carbons (i.e., living material) [2]. Carbon fixation results in several compounds, including proteins, fats or alcohol.

Biofuels refer to solid (bio-char) and liquid fuels (ethanol, vegetable oil and biodiesel) as well as biogases [1]. Solid biofuels such as wood were in use since ancient times as a source of heating and making fire. Liquid biofuels such as olive oil also were a proved source of lighting, especially in China [2]. In terms of using biofuels in engines, Otto and Diesel, whose engines' cycles are the basis of various automotive engines ever since, used alcohol and peanut oil, respectively. Later on, in 1903, Henry Ford designed

his T model cars with hemp-derived biofuels [3]. During World War II, Germany and Britain faced a considerable shortage of imported fossil fuels. Therefore these two countries replaced their fuels with potato and grain alcohol, respectively. From 1970 to 1990, the US experienced several successive oil shortages due to OPEC's major cut (1973), the Iranian Revolution (1979) and the Gulf war (1990). Hence the US and many other countries started adding ethanol to their regular fuels [4].

Biofuels have been developed through three generations. First-generation biofuels are made from food crops such as corn starch, sugar cane, vegetable oil and animal fat. The most known biofuels of this type are bioethanol, biodiesel, green diesel, syngas, biogas, bioethers and solid biofuels. As can be seen, most of the fuels used for transportation purposes are placed in this category; however, since the source of this category of biofuels are food crops, it is not as green (sustainable) as the other generation of biofuels. Second-generation biofuels are made of more sustainable feedstocks that do not fulfill food uses. Identified sources of these biofuels are grass, Jathropa or other seeds and waste vegetable oils. Cellulosic ethanol, biohydrogen and biohydrogen diesel are the recognized second-generation biofuels [5]. Although the laboratory production of the second generation biofuels is completed, their mass production is still under development. The third generation of biofuel has been recently categorized as biofuels extracted from algaes. Algaes have been previously recognized as a good source of second-generation biofuels; however, due to the much higher yields for low resources, it has been suggested to categorize this usage as a new generation of biofuels [3].

## 1.1 Biodiesel versus Diesel

Biodiesel is a renewable, clean-burning diesel replacement produced from mono-alkyl esters of long-chain fatty acids. It is extracted from soybean oil, canola oil, vegetable oil, animal fat or grease and fulfills the requirements of American Society of Testing Material Standard, ASTM D6751 [6]. This standard briefly describes the technical properties of biodiesel as follows [7]:

- Common name — Biodiesel (bio-diesel)
- Common chemical name — Fatty acid (m)ethyl ester
- Chemical formula range — $C_{14\text{-}24}$ methyl-esters or $C_{15-25}\ H_{28-48}\ O_2$
- Kinematic viscosity ($mm^2/s$ at 313K) — 3.3−5.2
- Density range ($kg/m^3$, at 288K) — 860−894
- Boiling point range (K) — > 475
- Flash point range (K) — 430−455
- Distillation range (K) — 470−600
- Vapor pressure (mm Hg, at 295K) — < 5
- Solubility in water — Insoluble in water
- Physical appearance — Light to dark yellow, clear liquid
- Odor — Light musty/soapy odor
- Biodegradability — More biodegradable than diesel
- Reactivity — Stable, avoid strong oxidizing agents

Physical properties of diesel, biodiesel and their blends are compared in Table 1.1. Conventionally, pure biodiesel is called B100 and the blends are named based on the

mass fraction of biodiesel and diesel. For example, B20 is made by 20% by mass of biodiesel and 80% by mass of diesel.

**Table 1.1 Physical properties of biodiesel, diesel and blends in the present work**

| Properties | Unit | Diesel | B100 | B50 | B20 | B5 |
|---|---|---|---|---|---|---|
| Density | $kg/m^3$ | 850 | 884 | 867 | 856.8 | 851.7 |
| Surface Tension | N/m | 0.0252 | 0.0271 | 0.02615 | 0.0255 | 0.0253 |
| Kinematic Viscosity | $m^2/s$ | 1.40E-06 | 4.20E-06 | 2.8E-06 | 1.50E-06 | 1.43E-06 |
| Heat of Combustion | kJ/kg | 45757 | 38681 | 42219 | 44149 | 45403 |

As can be seen in Table 1.1, the viscosity of biodiesel differs considerably from the viscosity of diesel. In addition, the heat of combustion of biodiesel is 15% less than that of diesel. Surface tension and density of biodiesel and diesel show unremarkable differences.

Biodiesel has some advantages compared to diesel fuel. The outstanding advantages are its renewability, availability, higher combustion efficiency, lower sulfur and lower aromatic content [8] [9], higher Cetane number, and higher biodegradability [10] [11]. Furthermore having a high flash point increases its portability, and having inherent lubricity increases its usage as a dual-application fuel/lubricant in engines [12] [13].

On the other hand, there are some disadvantages of using biodiesel as an alternative for diesel fuel. Among these disadvantages, the most important are its higher viscosity, lower heat of combustion, and higher nitrogen oxide ($NO_x$) emissions. In addition, biodiesel causes greater engine wear. It also degrades under conditions of prolonged storage [7].

## 1.2 Fuel Atomization and Spray

Breakup of a liquid jet to fine droplets is referred to as "atomization". Atomization of liquids plays an important role in several applications, such as coating, spray drying, humidifiers, cooling towers, gas turbines, internal combustion engines, agricultural liquid dispensers, oil-fired furnaces, and ink-jet printing. In a nutshell, when a bulk liquid jet breaks up into smaller droplets the liquid surface increases. Consequently, mass and heat transfer increases. Several parameters have crucial effects on this process, including, but not limited to, nozzle internal flow, jet surface waves, velocity profile at the atomizer exit, surface tension, gas velocity, direction, and turbulence at the nozzle exit. Accordingly, four forces act on the liquid: inertia, $\rho L^2V^2$; surface tension force, $\sigma L$; viscous force, $\mu LV$; and gravity force, $\rho L^3 g$; where $L$, $V$, $g$, $\rho$, $\sigma$, and $\mu$ represent the characteristic length of the jet (i.e., diameter, $D$), mean axial jet velocity, gravity acceleration, density, surface tension, and dynamic viscosity, respectively [14]. Hence four non-dimensional groups, including the Reynolds number, $Re=\rho LV/\mu$; the Weber number, $We=\rho LV^2/\sigma$; the Froude number, $Fr=V^2/gL$; and the Ohnesorge number, $Oh=We^{0.5}/Re$ can be defined to address these forces.

The instabilities of these forces (i.e., hydrodynamic instabilities), are referred as the root of liquid jet breakup. Figure 1.1 schematically shows different types of instabilities, which can be categorized as follows.

a) Rayleigh: this mechanism is responsible for breakdown of ligaments for several operating conditions.
b) Kelvin-Helmholtz: defined as aerodynamic shear instabilities.
c) Tollmein-Schlicting: caused by the effect of gas-phase turbulence.

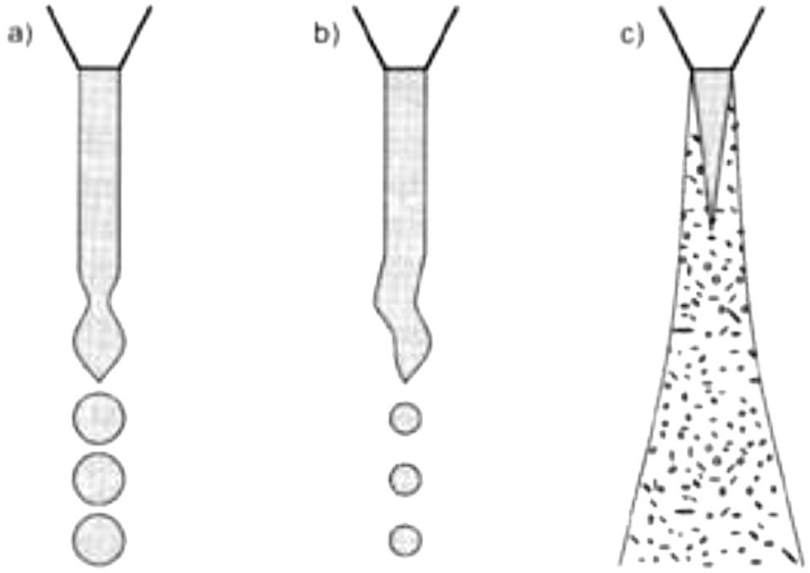


**Figure 1.1 Schematic of jet liquid breakup, a) Rayleigh, b) wind induced and c) atomization regime**

In studying the fundamental characteristics of spray and liquid atomization, the different modes of breakup should be considered. In order to investigate the different breakup modes usually two types of studies are performed; liquid jet injected into free ambient, and liquid jet in gaseous coaxial or crossflow. The former covers the effect of Rayleigh and Kelvin-Helmholtz instabilities and the latter covers the effect of Kelvin-Helmholtz and gas turbulence.

### *1.2.1 Free Liquid Jets*

The classical study of free liquid jet breakup was performed by Lord Rayleigh [15], to find the hydrodynamic instability breakups. In honor of his thorough and fundamental study, the capillary instabilities and their effects on the liquid jet breakup were named after him. During the 1930s, Weber [16] continued the study of Rayleigh by investigating the effect of liquid viscosity and gas density on liquid jet breakup. Basically, he defined a map of liquid jet breakup, using the ratio of inertia to surface tension force, which since

then has been called the Weber number. Taylor [17] performed an extensive study on the shear effect, especially at high velocities. Several researchers classified the breakup regimes of free liquid jet based on these studies (see Figure 1.2) [18] [14] [19].

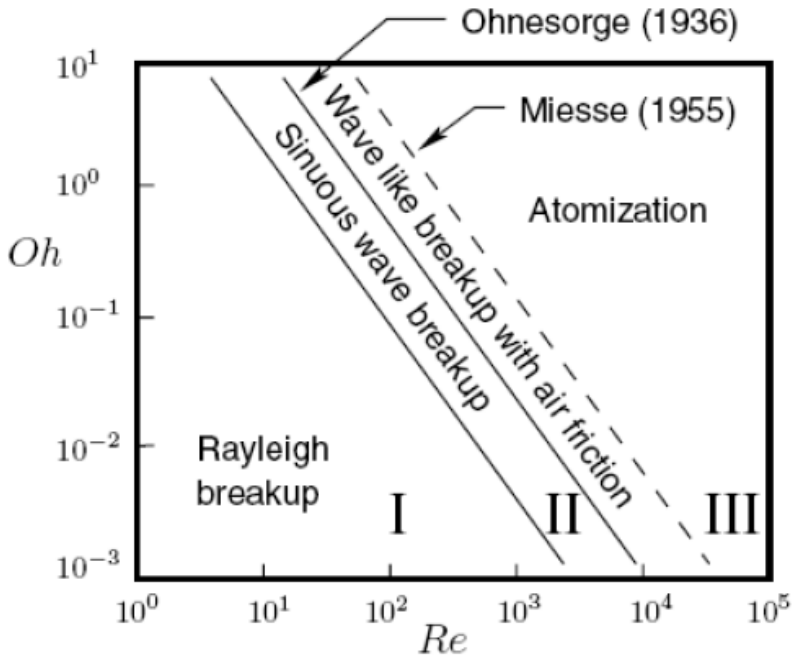


**Figure 1.2 Breakup regimes map proposed by [14], [19]**

Dumouchel [20] reviewed the breakup regimes of free liquid jet and stated the meaning of each regime as shown in Figure 1.3.

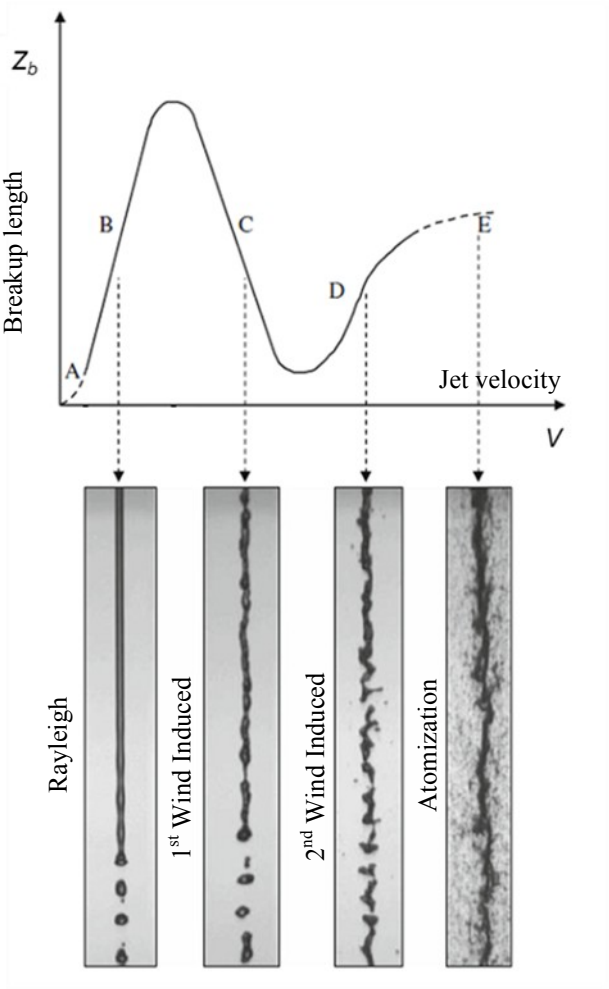


**Figure 1.3 Different breakup regimes of liquid jet in still-air, Dumouchel [20]**

Dripping regime (zone A), refers to the situation where individual drops are formed and emitted from the nozzle exit, without the formation of a continuous liquid column. By increasing the liquid inertia to greater than the surface tension force, the dripping no longer occurs [21]. In the Rayleigh regime (zone B) the liquid jet shows some capillary instability. The wavelengths of these instabilities are greater than the jet perimeter. In this regime, studies of [15] showed that the amplitude of the perturbations may increase as large as the jet radius. In this situation, the jet breaks up into droplets with the same diameter as the jet. By further increasing the jet velocity, the jet length reaches a

maximum. Then the first wind-induced regime begins (zone C). In this regime, the shear of the gas imposes some surface waves on the jet. These waves result in a reduction in the jet column length. It should be mentioned that in this regime, the size of the droplets is a little smaller than the droplets generated in zone B. During the second wind-induced regime (zone D), the inertia of the fluid dominates the gas-shearing force and once again the jet length increases [20].

### *1.2.2 Liquid Jet in Cross Flow (LJICF)*

Nowadays, Liquid Jet in Cross Flow (LJICF) is used in several applications and industries (e.g., gas turbine engines, ram jets, scram jets, film cooling, etc.). As mentioned before, four forces have contributions to the disintegration of LJICF: inertia, viscous, surface tension and gravity. Various injection parameters address these effects in both free and crossflow liquid jets such as injection angle, jet exit geometry and jet velocity profile at the orifice exit. The difference between a traverse liquid injection and free liquid jet is the added effect of second-phase inertia and turbulence. Therefore some additional parameters must be taken into account: jet to crossflow momentum flux ratio, and crossflow turbulence.

Generally, a liquid jet transversely injected into a gaseous stream is deflected by the drag force and can undergo different scenarios. Sallam et al. [22] clearly classified different scenarios based on the relative gas-to-liquid Weber number (see Nomenclature). Sallam et al. [22] introduced the various breakup regimes of LJICF happening at $We$ = 4, 30 and 110 for the transitions to bag, multimode and shear breakup regimes, respectively. Figure 1.4 shows these regimes visually.

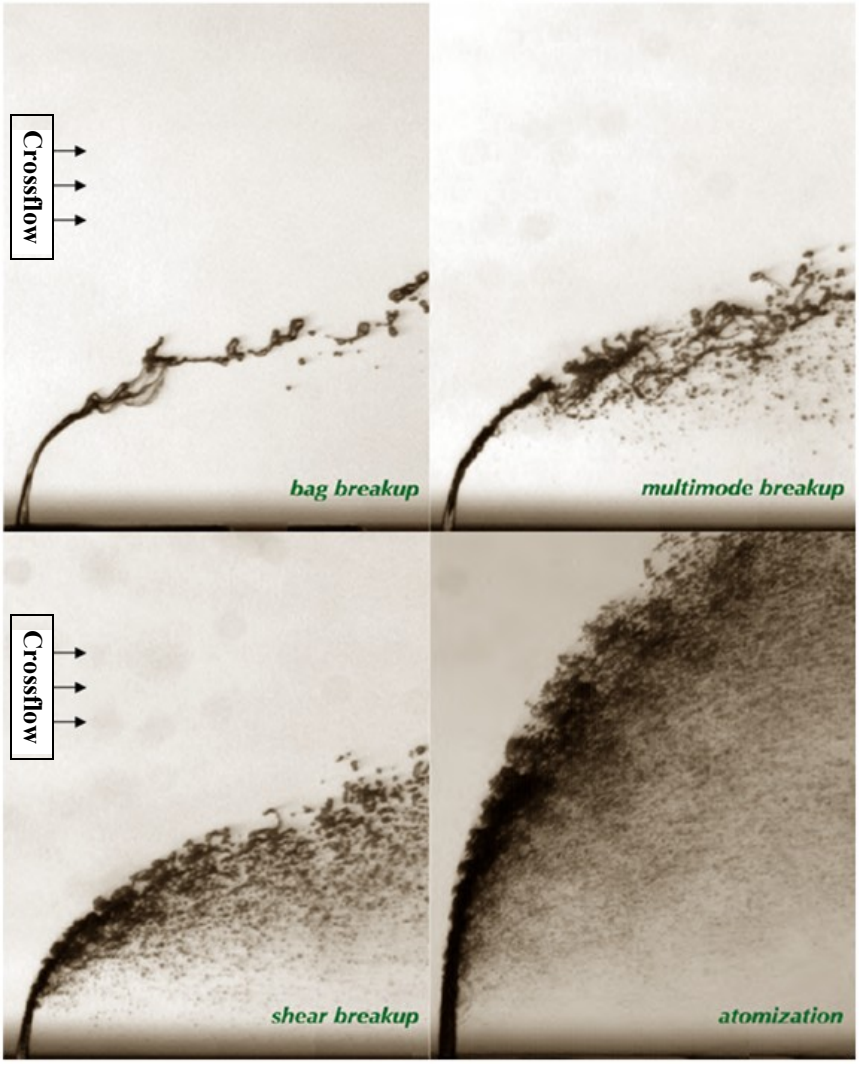


**Figure 1.4 Visualization of different modes of LJICF breakup [23]**

Technically, different regimes of LJICF breakup can be defined as follows [24].

- Column breakup happens when the aerodynamic forces are higher than viscous and surface tension forces.
- Bag breakup occurs when the jet is stretched into a thin bag shape such as two rims with entraining air into its pocket. In this regime, the bag pocket suddenly explodes when the air pressure force inside the bag becomes higher than the surface tension force.

- Multimode regime: a transitional regime between the bag and shear breakup regimes.
- Shear mode: fine droplets strip off the jet column side. It can be mentioned that this mode is analogous to the second wind-induced regime in the free liquid jet map.

One of the most important characteristics in different regimes of breakup is the liquid surface waves' wavelength $\lambda_s$, which is defined as the distance between each node on the liquid surface. Several studies including Sallam et al. [22] have used $\lambda_s$ as a definition for the transition of different breakup regimes. The wavelength non-dimensionalized by the original jet diameter, $\lambda_s/d_j$ for bag breakup regime is almost 1, which is consistent with the axisymmetric deflection of the flow to form a bag shape. This ratio, $\lambda_s/d_j$, for shear breakup ($We > 110$) is almost 0.1 because of the formation of ligaments; and finally, $\lambda_s/d_j$ for the multimode breakup regime ($30 < We < 110$) is between 1 and 0.1 due to the complex behavior of this regime ranging from bag to shear breakup. Further characteristics of LJICF breakup is presented in the chapters 2, 3, and 5. Therefore in order to avoid repetition of the literature review, a summary is given in Figure 1.5.

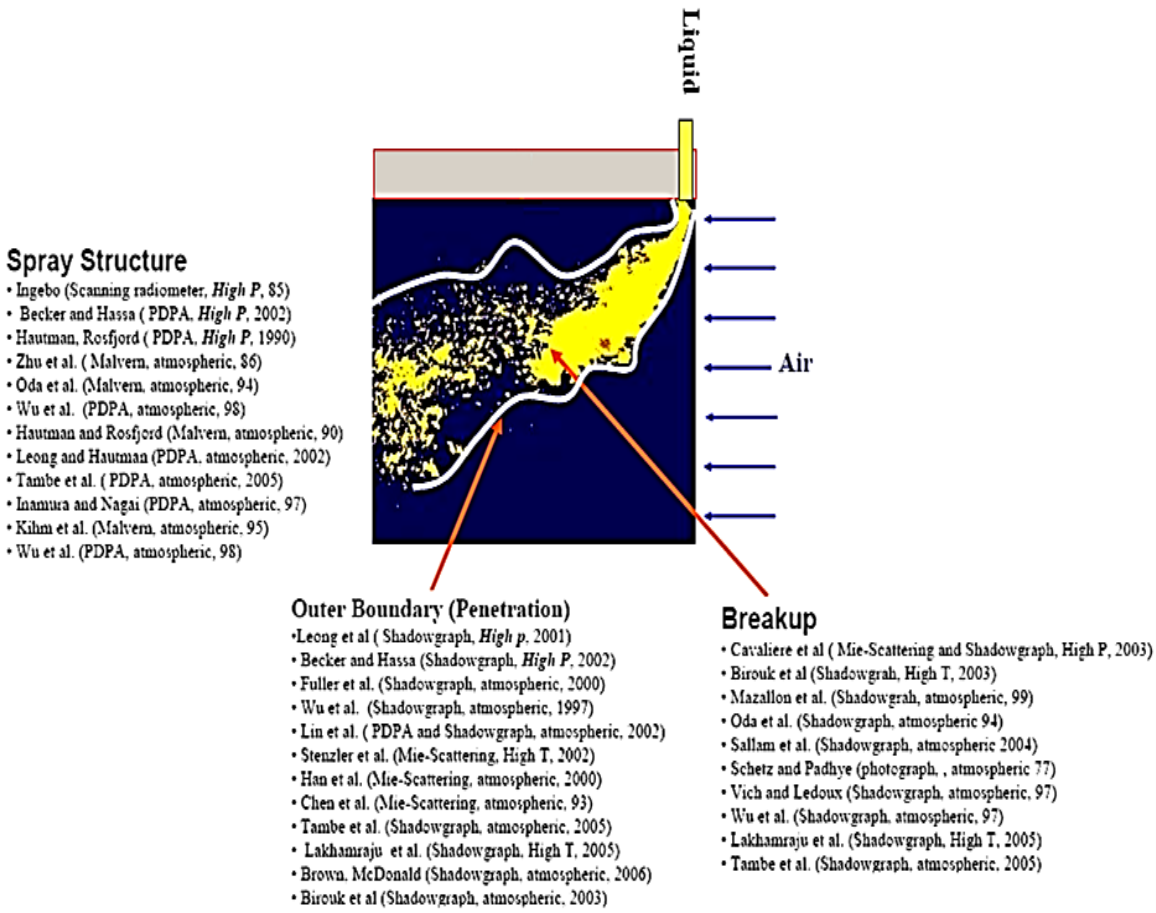


**Figure 1.5 Summary of the studies on LJICF [25]**

## 1.3 Effect of Orifice Ellipticity on Atomization

The spray droplet size, velocity and penetration directly influence the spray performance. In other words, being able to change the droplet size and control its penetration in the ambient lead to being able to change the combustion processes, coating efficiencies, spray drying outcomes, and so on. Currently, there are many attractions to replace conventional fuels to biofuel counterparts, as described in the previous sections. Changing the liquid in any combustion chamber, however, results in different physical properties and different atomization outcomes. For example, changing from diesel to biodiesel in any engine, as explained in the previous sections, results in 15% lower heat

of combustion for the same amount of fuel. Therefore, the simplest way to compensate for this shortage of combustion heat is to have a biased mass flow rate for biodiesel. Hence not only is the physical property of biodiesel different, but also its mass flow rate should be different. Imagine this in the combustion chamber of a gas turbine, for which the gas velocity is fixed according to the external parameters such as turbine and compressor. Considering this example, one should be able to adjust the penetration, droplet size, and so on.

One of the simplest ways to influence the penetration and droplet size distribution is by changing the orifice geometries. Among different types of atomizers, plain orifices have been extensively in service due to their ease of manufacturing. Recently, non-circular orifices attracted many researchers due to the fact that the corresponding jets may break up earlier than circular jets. Elliptical orifices rapidly found their way, among other non-circular orifices. Elliptical liquid jets emanating from these types of orifices always tend to configurations with minimum surface energy. Consequently, several inherent instabilities, such as axis switching, lead to breakup of these jets with less energy. In addition, the surface area of an elliptical jet is larger than that of the equivalent diameter circular jet. These effects result in faster disintegration of liquid jets. Husain and Hussain [26] found that in the atomization mode, elliptical jets have more rapid mixing, which is a remarkable profit in many combustor applications. Liquid jets emanating from elliptical orifices in air crossflow also have been studied by a few researchers, including but not limited to Song et al. [27]. They found that flames issuing from elliptical nozzles with major axis perpendicular to the crossflow have wider stability limits compared to flames

issuing from a circular nozzle, or elliptical nozzles with minor axis normal to the crossflow.

In addition, since the free surface of a liquid jet always seeks configurations with minimum surface energy, elliptical jets require less energy to break up due to the inherent instabilities [24]. Besides, the surface area of an elliptical jet is larger than its circular counterpart with the same equivalent diameter, hence it disintegrates faster; and an increase in orifice aspect ratio causes further destabilization of elliptical liquid jets. The benefit of such orifices is smaller breakup length and producing finer droplets at the end of the atomization process [24].

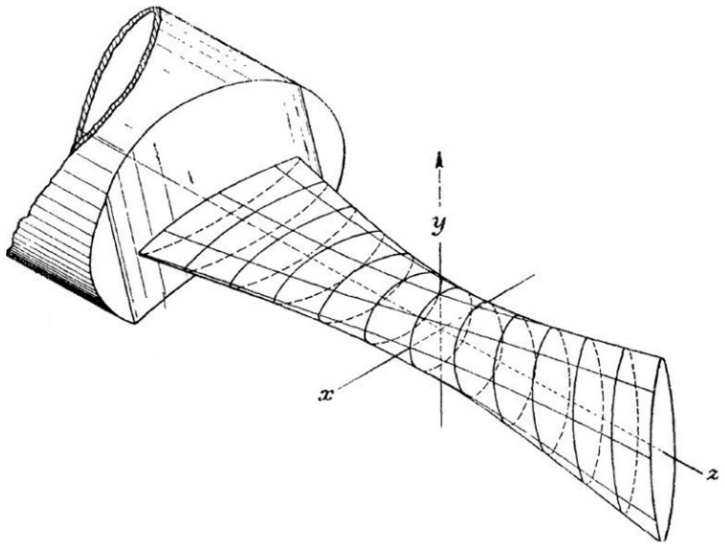


**Figure 1.6 Axis Switching Phenomenon [28]**

One of the interesting phenomena about elliptical jets that has been studied by researchers such as Kasyap et al. [29] is axis-switching of the jet column. At a sufficiently high Weber number the jet dilutes in one of its axes and contracts in the other direction and this will repeat periodically until it breaks up. The axis-switching

phenomenon is analogous to oscillation of a spring-mass system. The amplitude of disturbance overshoots several times until it becomes over-critical and rupture happens. Onset of the axis-switching process results in a significant reduction of the breakup length. By increasing the liquid Weber number the breakup length first increases until it reaches a maximum and drops rapidly after this point. An increase in nozzle aspect ratio results in shortening the length of breakup, and the presence of viscosity damps the axis-switching process.

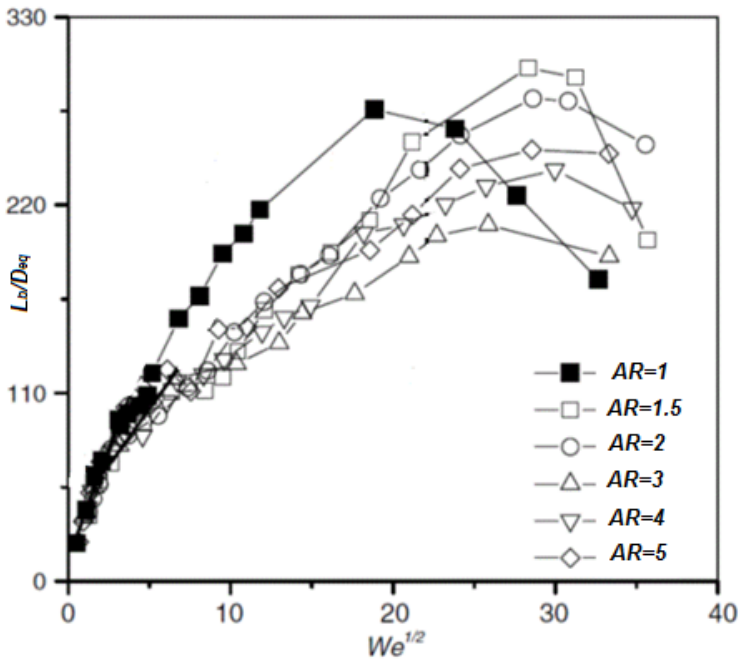


**Figure 1.7 Variation of the dimensionless breakup length ($L_b/D_{eq}$) versus $We^{0.5}$ for elliptical orifices [29]**

In addition to the researches on the effect of nozzle geometry on breakup of free liquid jets, some studies have been performed to investigate elliptical LJICF atomization. Marzbali [24] performed theoretical and numerical studies on elliptical liquid jets in crossflow. He found a logarithmic correlation for the windward trajectory of elliptical jets

based on the liquid jet column drag coefficient. The effect of viscosity is taken into account by using different drag coefficients for different materials.

$$\left(\frac{y}{a}\right)=\frac{\pi q}{C_D}\ln\left[1+\frac{C_D}{\pi q}\left(\frac{x}{a}\right)+\sqrt{\left(1+\frac{C_D}{\pi q}\left(\frac{x}{a}\right)\right)^2-1}\right]$$

**Equation 1.1 [24]**

Marzbali [24] also simulated elliptical LJICF and compared the results with the theoretical correlations. He modeled the multiphase flow using the Volume of Fluid (VOF) technique on a very fine mesh (without any dynamic mesh refinement). The results showed that the jets with lower aspect ratios, with major axis perpendicular to the gas flow, penetrate more into the crossflow since they have lower drag coefficients. In addition he showed the wakes upstream of the liquid jet. He found that the wake sizes on elliptical jets, with major axis perpendicular to the gas flow, are wider compared to a circular jet. Since he did not use any dynamic mesh refinement, the number of simulation cases is very limited and the results have some small discrepancies with the experimental tests.

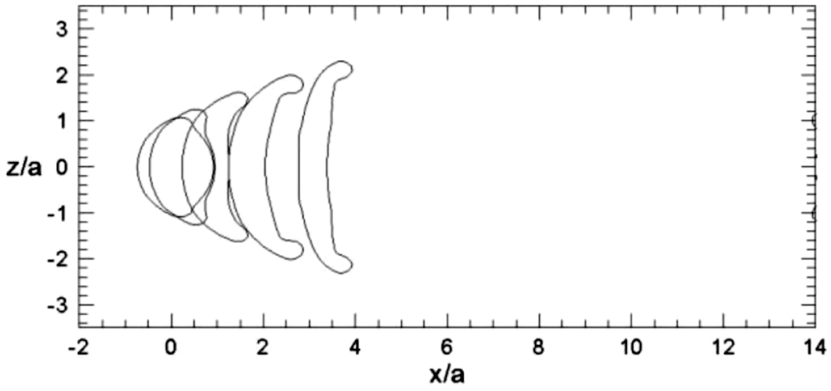


**Figure 1.8 Elliptical LJICF cross sections at different heights along its trajectory, *We*=10, *q*=10 [24]**

## 1.4 Objectives

In this thesis the behavior of biodiesel breakup from a bulk liquid jet to very fine droplets is studied. This fundamental study is performed to characterize the primary and secondary atomization of biodiesel as an alternative to diesel fuel. The main application of this work is focused on using biodiesel in the combustion chamber of gas turbine engines. However the results can be applied in other applications such as internal combustion engines and where there are high viscosity liquids to be atomized. Specifically, the objectives are summarized as follows:

1. *Find trajectory of biodiesel LJICF by shadowgraph:* Visualization of the trajectory of LJICF illustrates several characteristics of liquid fuel, such as penetration depth, breakup length, surface waves on the liquid jet, onset of breakup, jet column breakup length, slope of the liquid column jet, effect of drag on the liquid jet, spray structures, droplet size distribution and spray flux positioning. Although image processing and averaging of several snapshots results in different quantitative parameters, some of the shadowgraph results such as droplet size distribution and spray flux positioning need deeper experimental tests using laser diagnostics.
2. *Simulate biodiesel spray and find trajectory by Discrete Phase Model (DPM):* Since this study serves as a fundamental study to characterize biodiesel, various experimental tests are performed; however, various existing simulation models should be tested and calibrated in order to represent any future application of biodiesel spray. Therefore DPM simulations are performed and validated by the experimental tests, in order to verify the applicability of this model for biodiesel LJICF.

3. *Study of breakup processes by PDPA:* As mentioned before, some characteristics of biodiesel jets cannot be obtained quantitatively by shadowgraph images or their image processing. PDPA measurements of biodiesel LJICF is used first to verify the trajectory found by the shadowgraphs' image processing. Secondly, the droplet size distribution, velocity and flux positioning across the spray are obtained.
4. *Simulate the primary breakup process by Volume of Fluid (VOF) model:* In this model, the liquid as well as the gas phase are solved by the Navier-Stokes equation, and the interface is tracked after a dynamic refinement at each time step. Consequently, the surface waves, liquid jet column slope and breakup length, onset of breakup, and ligament topologies obtained from this model are validated by the experimental tests. In other words, the numerical simulations of this study are first validated by the experimental results (trajectory, instability waves, etc). Furthermore, in order to capture the time/space dependency of LJICF, the numerical results are used to capture high resolution ligament shapes, and droplet sizes. In this vein, not only the numerical results are validated, but also the restrictions of the experiments can be remedied to find additional characteristics.
5. *Study of elliptical jets in free gaseous environment:* The jets emanating from elliptical orifices are simulated and validated in order to find their characteristics. The elliptical jets are suggested as a means of controlling the penetration of liquid jet breakup. The breakup processes of elliptical jets also are compared to those of circular orifices.

6. *Study of elliptical LJICF:* The trajectory, ligament topology, slope of liquid jet column and droplet sizes generated by circular and elliptical jets with various aspect ratios are found. The primary breakup processes of elliptical jets are investigated as well. Specifically, the elliptical jets are studied as a technological alternative to compensate for the differences between the biodiesel and diesel jet penetration depths.

## 1.5 Layout of the Thesis

The thesis is organized in order to represent the abovementioned objectives.

Chapter 1 presents a general introduction on biodiesel as an alternative of diesel fuels. It starts with a history of biofuels, introduces biodiesel and its blends and compares their properties with diesel. Then a brief introduction is provided on fundamental atomization studies of any fuel. Necessary steps are illustrated in order to recognize the primary and secondary breakup behaviors of biodiesel. Since the characteristics of two alternative fuels might be different, a change in nozzle geometry from circular to elliptical with various aspect ratios is proposed.

Chapter 2 is a comprehensive experimental study of atomization of biodiesel and its blends. Furthermore the atomization characteristics of biodiesel are compared with diesel. The experimental methods consist of shadowgraphy and Phase Doppler Particle Analyzer (PDPA) laser diagnostics. Liquid jet trajectory, jet column breakup length, jet column slope, onset of breakup, droplet size distribution, and flux measurements are provided for biodiesel, diesel and their blends.

Chapter 3 consists of the simulation of biodiesel jet in crossflow. Two numerical methods are used in order to be firstly validated by the experimental results of Chapter 2 and propose the proper method for modeling the atomization of biodiesel.

Chapter 4 shows the numerical investigation of the breakup process of a liquid jet emanating from a set of elliptical orifices with different aspect ratios. The results are compared with the circular orifice jet. The differences in the jet breakup characteristics are observed as potential means of controlling the liquid spray. This study incorporates the liquid jet in free air, the capillary breakup and the effects of Rayleigh instabilities on the jet breakup.

Chapter 5 presents the differences between primary breakup of LJICF through circular and elliptical jets with major axis toward the gas flow direction or traverse to the gas flow direction. The penetration depth, surface waves, ligament topologies and onset of breakup have been obtained for different configurations and conditions of elliptical and circular jets. Since the results of Chapters 2–3 show a remarkable change in the penetration of biodiesel LJICF, even with higher mass flow rates, it is suggested to use elliptical jets with different configurations in order to remedy the biodiesel penetration. This state-of-the-art idea can be used as a means of controlling the biodiesel atomization.

Chapter 6 summarizes the findings and provides recommendations for further research.

# Chapter 2

# Comparative Study of Biodiesel and Diesel Jets in Gaseous Crossflow-Experimental Study


## Abstract

This study compares the fundamental spray characteristics such as penetration depth, droplet diameter, velocity, and volume flux of biodiesel and diesel as well as their blends. Liquid jet is injected into an air crossflow with a speed of 58 m/s. A series of experimental tests covering Weber numbers from 29 to 82 and momentum flux ratios from 10 to 133 are conducted using the shadowgraph method and Phase Doppler Particle Analyzer (PDPA). The shadowgraph images are processed in order to find the penetration depth and to investigate different regimes of breakup. PDPA is used for capturing droplet size distribution, velocity, and volume flux. The results differ remarkably in terms of breakup regimes and trajectory for biodiesel blends, which may be due to the high viscosity of biodiesel in comparison to diesel. For example, at a Weber

number of 80, some bag breakups are observed on the biodiesel jet against the expectation that, at this Weber number, most of the liquids experience atomization mode.

## 2.1 Introduction

Recently, biodiesel has attracted the interest of many industries due to its renewable resources, Cetane number, and lower pollution of particulate matter, while its atomization, ignition, and combustion efficiency have been critiqued [30], [31]. In terms of order and time constant, spray atomization dominates several consecutive processes of combustion, such as mixing, evaporation, and ignition. It even affects the capacity of pollution (i.e., $NO_x$, soot, and carbon monoxide). For this reason, many studies have been devoted to the fundamentals of penetration depth, spray structure, droplet size distribution, primary breakup of liquid jets to ligaments, and secondary breakup of ligaments or droplets into smaller droplets [32], [33], [34], [35], [36], [37], [38]. One of the most important properties of liquid sprays is penetration and the subsequent trajectory of the liquid fuel spray. Indeed, fuel distribution and the trajectory of spray in the combustion chamber of engines can influence flame shape and combustion instability [38]. In order to study the effects of using different fuels on these parameters, the study of liquid jet in gaseous crossflow is used to perform a fundamental investigation and translate over applied industrial conditions.

An extensive literature review of liquid jet in crossflow can be found in the work of Elshamy [25]. One of the first studies of penetration of water jet in crossflow has been performed by Schetz and Padhye [32]. They worked experimentally on the effect of momentum flux ratio on the length of jet column breakup. Thereafter Mazallon et al. [39] and Wu et al. [33], [34], [35] proposed new breakup maps for liquid jets in crossflow

based on the gas-liquid Weber number. Mazallon et al. [39] classified and visualized four different regimes of primary breakup as column, bag, multimode and shear breakup regimes. The column breakup results in the breakup of the jet to the same diameter size droplets. In the bag breakup, the liquid jet is flattened from the sides and makes bag shape structures before breakup. The multimode breakup represents a breakup regime where both bag shape structures and liquid ligaments appear after primary breakup, and finally shear breakup is the regime that liquid ligaments and droplets are sheared off the liquid jet surface. In addition, Wu et al. [33], [34], [35] conducted a series of tests on water, glycerol, and ethanol in order to take into account the effects of viscosity and surface tension. Furthermore, they correlated the windward trajectory of spray and breakup length to the momentum flux ratio; however, the correlation does not contain viscosity or the Weber number (Equation 2.1). Moreover, Wu et al. [33] classified the liquid disintegration into surface breakup and column breakup regimes. The study of Wu et al. [33] showed that at large liquid/gas momentum flux ratios, surface breakup happens before the large surface waves' development. This is in a manner that for more viscous liquids, the appearance of surface waves plays an important role in the breakup process.

$$\left(\frac{y}{d}\right) = 4.3\left(q\frac{x}{d}\right)^{0.33} \qquad \textbf{Equation 2.1}$$

Iyogun et al. [37] extended the results of [35] for lower Mach numbers of crossflow gas. They also proposed a correlation for low subsonic regimes, similar to the study of [35], the correlation for the windward trajectory of sprays did not include the effect of viscosity or the surface tension of liquid. Following these works, Birouk et al. [40], conducted a series of experiments in order to study the effect of viscosity on the primary

breakup regime map. Their results showed that viscosity greatly affects the boundaries of breakup regime maps. In another study, Birouk et al. [41], investigated the effect of viscosity on the penetration and trajectory of the liquid jet in crossflow. Their study revealed that generally, the jets' penetration decreases by increasing the liquid viscosity. Stenzler et al. [38] found that the viscosity and Weber number can directly affect the trajectory and penetration of sprays in crossflow and they included these effects in their proposed correlation. They tested water, kerosene, acetone, and 4-heptanone (see Equation 2.2).

$$\left(\frac{y}{d}\right) = 3.688 q^{0.430} \left(\frac{x}{d}\right)^{0.384} We^{-0.110} \left(\frac{\mu}{\mu_{H_2O}}\right)^{-0.108} \qquad \textbf{Equation 2.2}$$

Sallam et al. [22] conducted a series of experimental tests using shadowgraphy and holography techniques. They characterized the breakup of round nonturbulent liquid jets in gaseous crossflow by determining primary breakup regimes. They also determined conditions for the onset of ligament and drop formation. They found a comparable analogy between the primary breakup of nonturbulent liquid jets in crossflow and the secondary breakup of drops subjected to the shockwaves. In addition, it was shown that the transition between various breakup regimes are not influenced by the liquid viscosity and happens at $We$=4, 30 and 110 for the transitions to bag, multimode and shear breakup regimes, respectively. An important characteristic parameter in different regimes of breakup is the liquid surface waves appearing on the windward side of the liquid jet. The wavelength $\lambda_s$ of these surface waves is defined as the distance between each two nodes on the liquid surface. Several studies including Sallam et al. [22] have used $\lambda_s$ as a definition for the transition of different breakup regimes. The wavelength non-

dimensionalized with the original jet diameter, $\lambda_s/d_j$ for bag breakup regime is almost 1 "which is consistent with the somewhat axisymmetric deflection of the flow to form a bag" [22]. This ratio, $\lambda_s/d_j$, for shear breakup ($We$>110) is almost 0.1 to be consistent for the formation of ligaments having a similar diameter as $\lambda_s$ and finally $\lambda_s/d_j$ for multimode breakup regime (30<$We$<110) is between 1-0.1 due to complex behavior of this regime ranging from bag to shear breakup. Furthermore, Sallam et al. [22] used the onset of breakup properties as a feature of primary breakup in order to classify the breakup regime. For example, Sallam et al. [22] have measured the liquid jet diameter and concluded that the ratio of jet diameter at the nozzle exit to the jet diameter at the onset of breakup ($d_j/d_i$) is equal to 2 and 1 at the bag breakup regime ($We$<30) and shear breakup regime ($We$>110), respectively. On the other hand at the multimode breakup regime (30<$We$<110), this ratio ($d_j/d_i$) has a uniformly decreasing behavior from 2 to 1 from $We$=30 to $We$=110.

From the numerical point of view, a series of Lagrangian particle tracking simulations of droplets in a gaseous crossflow is performed by Madabhushi [42]. He used a Reynolds Average Navier-Stokes (RANS) coupled with k-ε turbulence model for the gaseous part and validated his results. Although a general agreement with the experiment was observed, due to the absence of wakes and vortices which are mostly damped by $k$-$\varepsilon$ model, some of the droplets' velocity and size were different from the experiment. Subsequently Ng et al. [43] performed a Volume of Fluid numerical modeling of liquid jet in crossflow. Several correlations between the wavelength, jet diameter and Weber number were obtained based on their study. Later on, Hermann [44] developed a Refined Level Set Grid (RLSG) method, which is coupled with Large Eddy Simulation (LES)

turbulence model, for capturing the liquid interface of the jet in crossflow. The simulations of Hermann [44] showed two main mechanism of liquid breakup. The first mechanism which is a Kelvin–Helmholtz instability, waves on the liquid column generate roll-ups and continue to grow along the jet axis until they form bag-like structures and result in a broad range of drop sizes. In the second mode, corrugations on the liquid jet surface are stretched out into ligaments and consequently break up into a range of drop sizes. Recently, Hermann et al. [45] investigated the impact of liquid/gas density ratio on the primary breakup of a liquid jet in crossflow. They found that density ratio has a noticeable effect on the liquid core dynamics during the breakup even if all other relevant characteristics are set equal. More specifically, an increase in density ratio results in an increase in liquid core penetration with reduced bending in the crossflow; however, the post-primary atomization spray penetrates farther in both the jet and transverse directions. They also mentioned that an increase in density ratio results in a decrease in the wavelength of instabilities along the jet. Regarding the wavelength of disturbances on the windward side of the liquid jet in crossflow, Pai et al. [46] performed numerical simulations using spectrally resolved level set method with an emphasize on the effect of Weber number on the wavelength. It is concluded that decreasing the Weber number lead to an increase in the wavelength of windward disturbances of the liquid surface and vice versa. Based on this practice, they found an excellent agreement with the experiments on the shape and size of the ligaments.

To the best of knowledge of the author of this thesis, no specific research has been found for correlating the penetration of biodiesel and its blends in crossflow. In this study, trajectories of traverse liquid jets in a subsonic crossflow of air have been

compared using experimental tests. Diesel, biodiesel, and their blends are injected at different gas Weber numbers (from 29 to 82) and liquid-to-gas momentum flux ratios (from 10 to 135). The gaseous flow in an open loop wind tunnel is air at atmospheric conditions with a maximum velocity of 58 m/s. Since biodiesel properties such as density, viscosity, and heat of combustion are not the same as diesel, these experiments have been designed to provide unbiased comparisons. Using a fixed Weber number, the momentum flux ratio of biodiesel, which leads to the same heat of combustion as diesel, is selected to be compared. Shadowgraph technique and filtering are used to obtain the windward trajectory of the spray, which represents the penetration of the fuel in crossflow.

## 2.2 Experimental Setup

The experimental setup used in this work consists of an open loop subsonic wind tunnel with a test section of 100×100×750 mm. The test section is made of glass in order to resist against the high corrosion of biodiesel. The environment air is blown into the wind tunnel by a 1.5HP blower fan made by Aeroflo (Mississauga, ON, Canada). Then the flow passes through a fine screen and a nozzle before reaching the test section. The velocity inside the test section can be varied between 20 and 58 m/s by means of using a damper located at the inlet of the fan. The maximum air velocity in the test section is characterized by Particle Image Velocimetry (PIV) measurements of a very fine spray (less than 10μm) in order to find the exact velocity vector directions, turbulence intensity, and to calibrate the measurements of a Pitot tube. The PIV measurements (see Figure 2.16, Appendix at page 50) show that in the test section, the velocity of air is parallel and constant at each axial location except the narrow boundary layers on the wall, which are

less than 10 mm thick on each side. Therefore, the air axial velocity can be considered uniform in the liquid jet's upstream. In addition the PIV results show a turbulence intensity of 9% exists at the wind tunnel test section just upstream of the injector location. After the calibration of the Pitot tube for the maximum velocity with the PIV measurements, the air velocity and pressure inside the test section are measured using the Pitot tube. A schematic of the liquid injector is shown in Figure 2.1. As can be seen in Figure 2.1, the injector is a plain circular tube with a diameter of 0.5 mm. A tapered transition from the 2 mm to 0.5 mm is applied to avoid cavitations. The length to diameter is also considered 100 in order to have fully developed flow in all cases, even the lowest velocity, which can cause the laminar flow inside the injector; however, the high-pressure losses by using this long injector are compensated for by the fuel pump. The injector is mounted vertically on the top of the test section at an axial position of 200 mm from its inlet plane. The center of the 0.5 mm diameter lies on the symmetry plane of the test section.

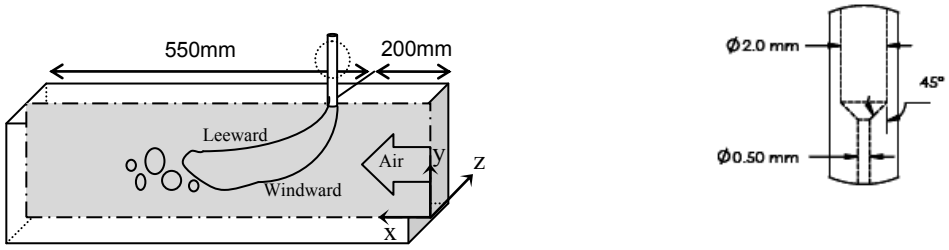


**Figure 2.1 Schematic of the wind tunnel test section and injector**

Shadowgraph with a high-speed camera (Photron SA1.1, USA) has been used for capturing images of the spray side view (x-y plane in Figure 2.1). In order to have images with good contrast, even for the smallest droplets on the windward edge of the spray, the

trajectory was captured at 250 frames per second and the shutter speed was set at 1/593000 sec. Having this configuration, 500 images, with a resolution of 1024×1024, were captured for each test. In addition, 500 images were captured from the background without any liquid spray. In order to eliminate the background noise from the spray images, and digitizing the images to find the spray windward trajectory, a code was written using the image processing toolbox of MATLAB. The minimum value of each pixel, among 500 background images, creates the background image. The next step in the image processing code is to eliminate the background image from the spray image. The resultant images without background noise are superimposed to form the average spray trajectory. A sample raw image and the superimposed image of this process are illustrated in Figure 2.2. Using a 25% light cut-off threshold [47], the windward and leeward spray boundaries are defined as the loci of the points with the lowest light intensity. Finally, a number of points (i.e., 50-100) are sampled on the locus of windward trajectory and a curve is fitted to the sample points. It should be mentioned that the uncertainty of the obtained trajectory is proportional to the size of image, the image resolution and the number of pixels per jet diameter. Having about 11 pixels per diameter and the size of image (100×100 diameter), lead to 0.1% uncertainty in the trajectories.

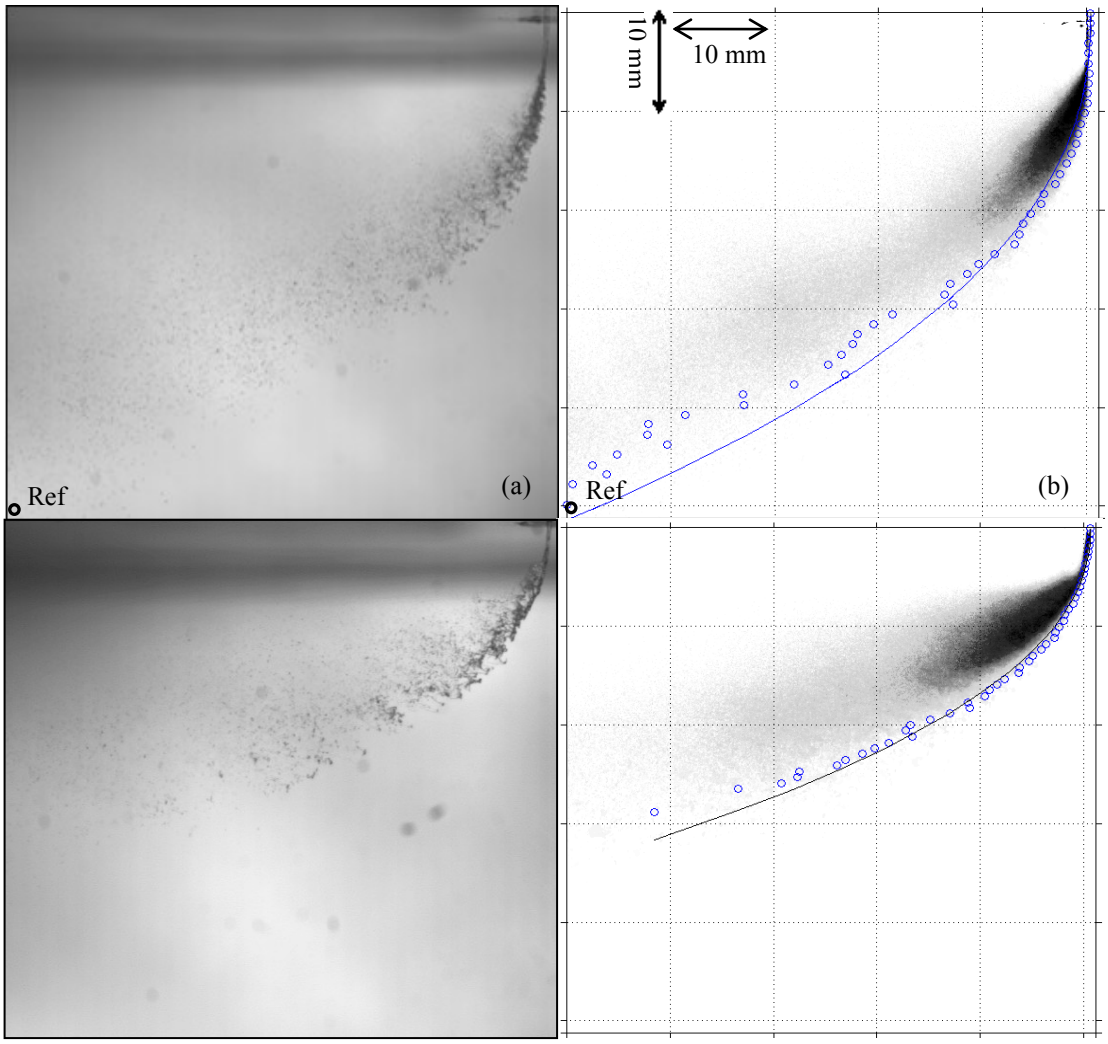


**Figure 2.2 a) Snapshot of diesel spray, *We* = 80, *q*=82, b) Filtered and averaged 500 snapshots of diesel spray, *We* = 80, *q*=82, c) Snapshot of B100 spray, *We* = 76, *q*=102, d) Filtered and averaged 500 snapshots of B100 spray, *We* = 76, *q*=102. Circle markers indicate the windward trajectory points of the spray and the lines are exponential fitted curves. Reference points are the windward trajectory points 50 mm downstream**

Two-dimensional Phase Doppler Particle Analyzer (PDPA) by TSI Inc. (MN, USA) is used as a vehicle for other experiments. Two components of the droplet velocity, as well as the droplet diameter, are captured in a 143° forward scattering of the PDPA probes (TSI Inc.). The PDPA is set up on a traverse with a 0.1 mm spatial increment (ISEL Germany). The focusing point, considering the refractions of the glass walls, is

found and set on the reference point at a 50 mm section downstream of the nozzle exit. It should be mentioned that, for each test, the reference point is selected to lie on the windward trajectory point (see Figure 2.2). In addition, three other points are captured under this point (see Figure 2.3) in order to make sure that this point is lying on the windward trajectory. In order to capture the whole spray characterization, 25 points in a 5×5 matrix are set up to perform the velocimetry and capture the droplet size distribution. Furthermore, to find out that the 5×5 matrix lies in the spray and does not reach the leeward location of the spray, five more points are set up on the top of the matrix. The PDPA tests are conducted on this matrix for diesel, biodiesel, and different blends 50 mm downstream of the injection point. It should be mentioned that a droplet sphericity measurement is performed according to the work of Araneo et al. [48], for several traverse planes downstream the orifice. The test resulted in having higher than 90% spherical droplets among the total captured droplets at 50 mm downstream, while the same test depicted for example ~65% spherical droplets/ligaments at 25 mm plane downstream that may translate to inaccurate measurement or incomplete secondary breakup. Consequently, 50 mm plane downstream the orifice have been selected for PDPA measurements.

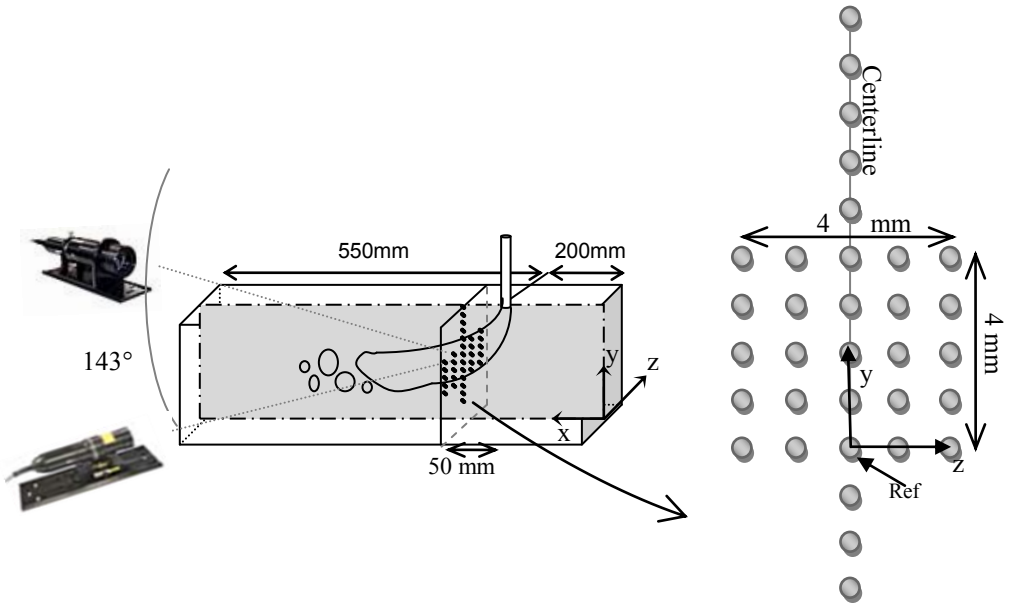


**Figure 2.3 Test Section Schematic, the planes on which PDPA is done and the matrix of capturing points**

Diesel, biodiesel (B100) and several blends (i.e., B50, B20 and B5) are tested for several momentum flux ratios and Weber numbers. The blends are named based on the percentage of the mass ratio of biodiesel to diesel. For example, B20 is made by 20% by mass of biodiesel added to 80% by mass of diesel. The biodiesel in the present work is an ASTM 6751-based vegetable fatty acid methyl ester which is refined and produced by Rothsay Biodiesel, Canada, from animal fat and recycled cooking oil. In addition, this diesel is the known D-2 type diesel provided by Ultramar, Canada. The physical properties of biodiesel (B100) and biodiesel blends B20 and B5 are obtained mainly from the material fact sheet of the same day, same batch production and also from the literature [49], [50] which has a similar combination. In fact, a comparison between the repeated physical properties from the literature and the factsheet shows a negligible ±5%

difference. The properties are shown in Table 2.1. Additionally, the properties of B50 are interpolated between the properties of B20 and B100.

**Table 2.1 Physical properties of diesel, biodiesel, and blends**

| Properties | Unit | Diesel | B100 | B50 | B20 | B5 |
|---|---|---|---|---|---|---|
| Density | $kg/m^3$ | 850 | 884 | 867 | 856.8 | 851.7 |
| Surface Tension | N/m | 0.0252 | 0.0271 | 0.02615 | 0.0255 | 0.0253 |
| Kinematic Viscosity | $m^2/s$ | 1.40E-06 | 4.20E-06 | 2.8E-06 | 1.50E-06 | 1.43E-06 |
| Heat of Combustion | BTU/lb | 19672 | 16630 | 18151 | 18981 | 19520 |

The test matrix for each liquid is composed of three different air velocities. For each air velocity, three momentum flux ratios are tested. Consequently, 45 different test conditions are performed to include a wide range of momentum flux ratios (q) and Weber numbers (Table 2.2). The test conditions for diesel and biodiesel blends are adjusted to provide the same amount of heat of combustion for all test cases. For example, the momentum flux ratio of 100 for diesel has an equal heat of combustion as the momentum flux ratio of 135 for B100, if we assume the same combustion efficiency. This results in having higher mass flow rates for the biodiesel blends compared to those of the diesel case, but this unbiased test condition seems more practical in the industrial applications, where there are different choices of fuel for the same combustion chamber.

**Table 2.2 Experimental test conditions**

| Parameters | Unit | Diesel | B100 | B50 | B20 | B5 |
|---|---|---|---|---|---|---|
| $V_g$ | m/s | 35, 45, 58 | 35, 45, 58 | 35, 45, 58 | 35, 45, 58 | 35, 45, 58 |
| $T_g$ | °C | 20 | 20 | 20 | 20 | 20 |
| *Mach No.* | | 0.1, 0.13, 0.17 | 0.1, 0.13, 0.17 | 0.1, 0.13, 0.17 | 0.1, 0.13, 0.17 | 0.1, 0.13, 0.17 |
| $We_g$ | | 29, 48, 80 | 28, 46, 76 | 29, 48, 79 | 29, 49, 81 | 30, 49, 82 |
| $q$ | | 10, 50, 82, 100 | 13, 67, 102, 135 | 12, 58, 94, 115 | 11, 53, 87, 107 | 10, 51, 81, 101 |

## 2.3 Results and Discussion

Figure 2.4 show the windward trajectories of diesel, B50, and B100 for air velocities of 45 and 58 m/s. In addition, the correlations of Stenzler et al. [38] and Birouk et al. [41] are illustrated in these figures. As can be seen in Figure 2.4, the correlations of Stenzler et al. [38] and Birouk et al. [41] show good agreement in case of diesel trajectories, especially at the injection near field. However the correlations cannot predict the trajectory of biodiesel blends very well.

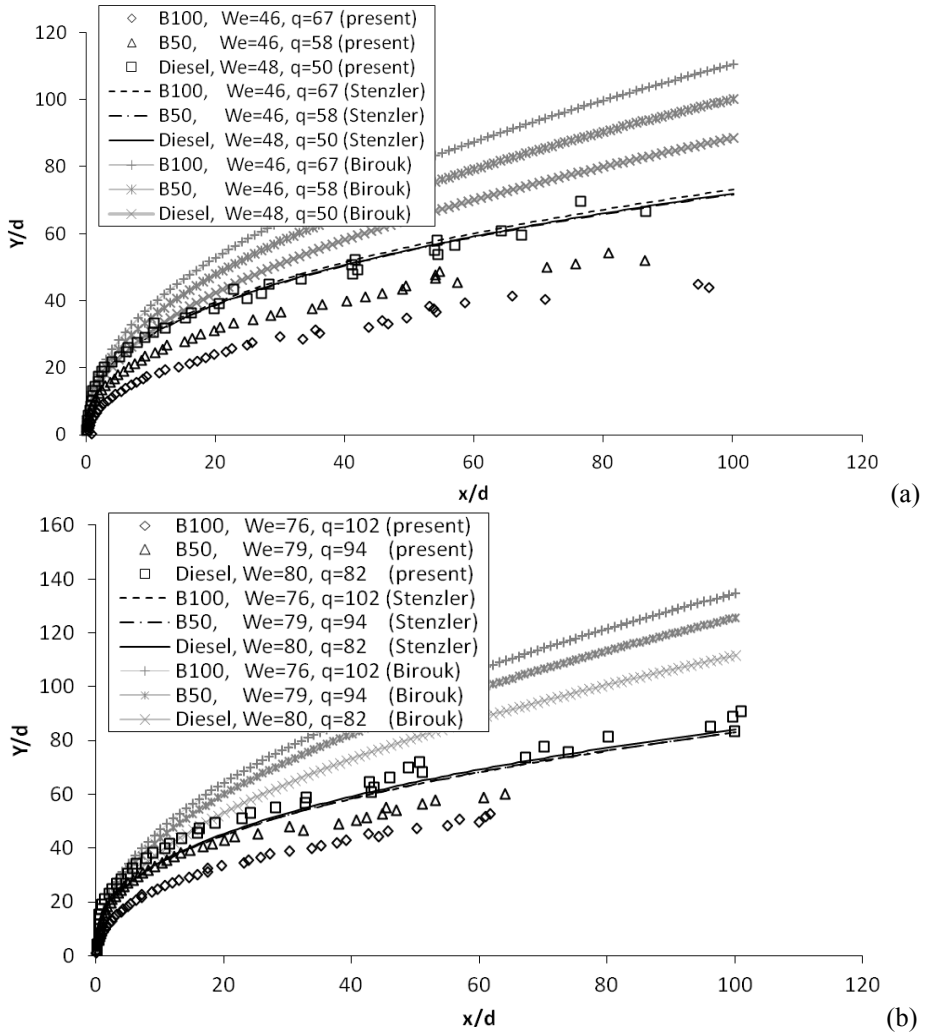


**Figure 2.4 a, b) Experimental and empirical trajectories for similar Weber numbers and different momentum flux ratios in the test matrix**

The source of this discrepancy can be explained by inspecting the snapshots of Figure 2.5. It is apparent in Figure 2.5 that due to the high viscosity and different surface tension of biodiesel, the breakup regime of biodiesel is bag breakup even at a Weber number as high as 76 while in the cases of water and most fuels, such as diesel, kerosene, and ethanol at Weber numbers as high as the aforementioned value, the breakup regime is atomization-multimode [33]. Owing to this fact, the primary breakup of biodiesel fuels seems to have an important role in the penetration depth of biodiesel. Furthermore, the snapshots of Figure 2.5 show a straighter column of diesel compared to the jet column of biodiesel exiting just below the nozzle. This phenomenon is interesting, since it shows higher drag coefficient associated with the biodiesel jets which result in a blunt jet. In addition, the existence of higher surface wavelengths on biodiesel jets can be responsible for this major difference compared to the diesel jet breakup. Time-series direct visualization images of the liquid jet breakup at the near field of injector are available in Appendix (p.51-52) for various Weber numbers. Although the shadowgraph images of Figure 2.5 and Appendix (p.51-52) qualitatively show the aforementioned behaviors, quantitative investigations by measuring wavelength and onset of breakup are performed as described below.

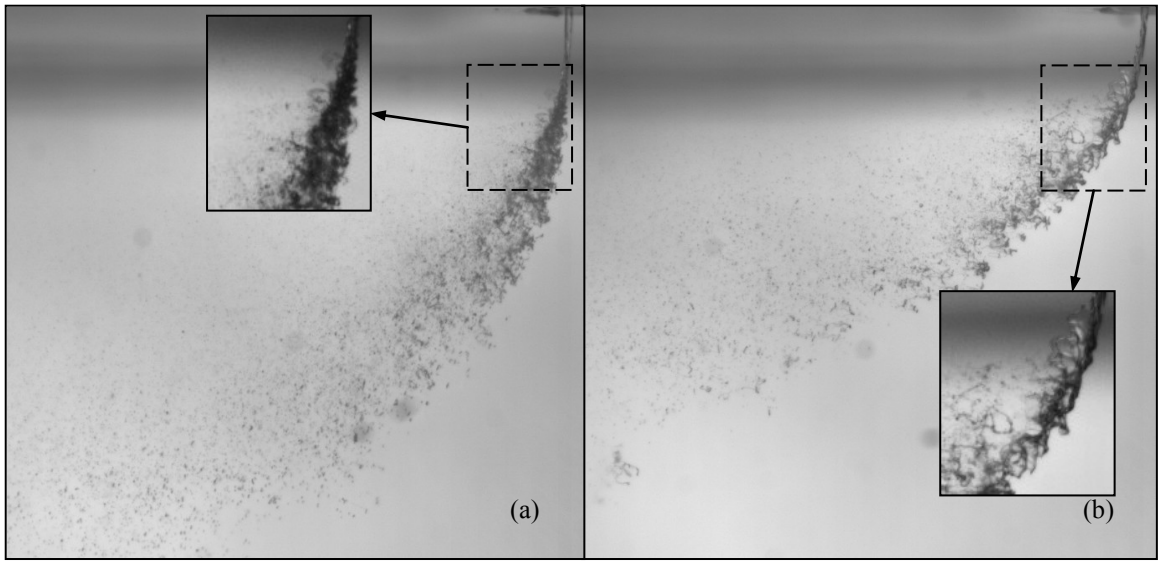


**Figure 2.5 a) Shadowgraph snapshot of diesel, *We*=80, *q*=82, b) Shadowgraph snapshot of B100, *We*=76, *q*=102 (close up images show different breakup regimes for diesel and B100, i.e. atomization regime and bag-multimode regime, respectively)**

In order to investigate the effect of viscosity of biodiesel on drag, liquid column and primary breakup, a detail image processing is performed on the shadowgraph images in order to find the onset of breakup point. As mentioned in the literature review, according to Sallam et al. [22], the ratio of jet diameter at the nozzle exit to the jet diameter at the onset of breakup ($d_j/d_i$) has a uniformly decreasing behavior from 2 to 1 from *We*=30 to *We*=110 (multimode breakup). Figure 2.6 shows $d_j/d_i$ ratio for diesel, B50, and B100. At each Weber number, three points are drawn for each liquid, which represents the low, medium and high momentum flux ratio, *q*, from bottom to top.

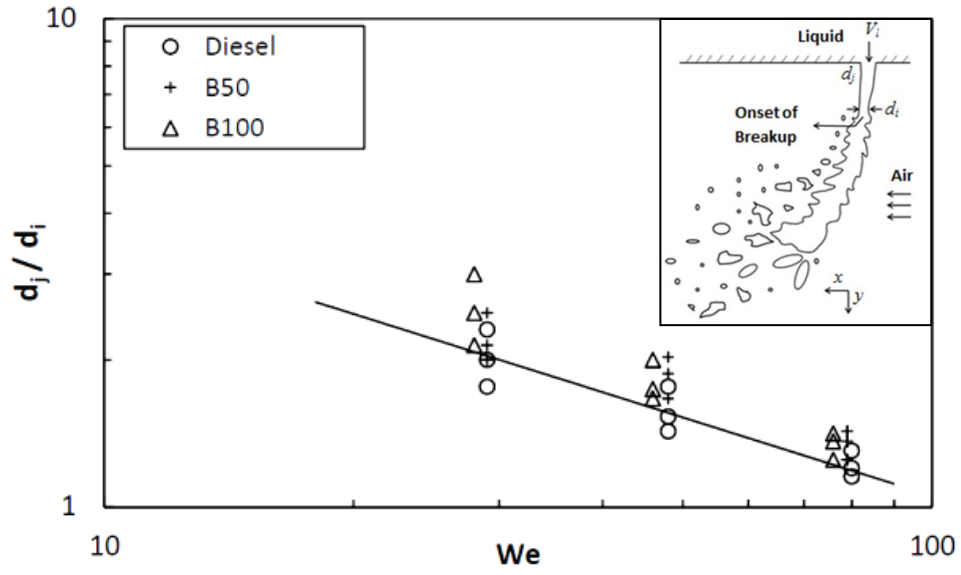


**Figure 2.6 The ratio of jet diameter at the orifice exit to the diameter at the onset of breakup for diesel, B50, and B100 at different Weber numbers and momentum flux ratios, compared with Sallam et al. [22]**

As can be seen in Figure 2.6 the ratio of $d_j/d_i$ for diesel agrees well with the results of Sallam et al. [22] at multimode breakup regime (i.e. $30<We<110$). This is in a manner that at each Weber number, the ratio of $d_j/d_i$ for B50 is greater than $d_j/d_i$ for diesel. $d_j/d_i$ for B100 is greater than both $d_j/d_i$ for B50 or diesel. Apparently, this repeating behavior for various Weber numbers shows that generally, the diameter at the onset of breakup, $d_i$, for B100 is smaller than B50 and $d_i$ of B50 is smaller than diesel. This shows that the column shape is squeezed more for B100 from the side view. Consequently, when a jet is narrowed in one direction, it should be widened in another direction, namely facing the crossflow. Apparently, the wider the area, facing the crossflow, the higher is the drag of the jet column.

Figure 2.7 depicts the slope of the jet column from the nozzle exit to the onset of the breakup. It is clear that at different Weber numbers, the slope of biodiesel liquid jet in crossflow is greater than that of diesel. Higher slopes of the jet column clearly translate to having less penetration for biodiesel as concluded in the previous section where the trajectories are correlated. In other words, the liquid jet of biodiesel is bent more towards downstream which affects the disintegrated droplets as well. Once again, the higher slopes of the jet columns show greater drag acting on the jet column for biodiesel.

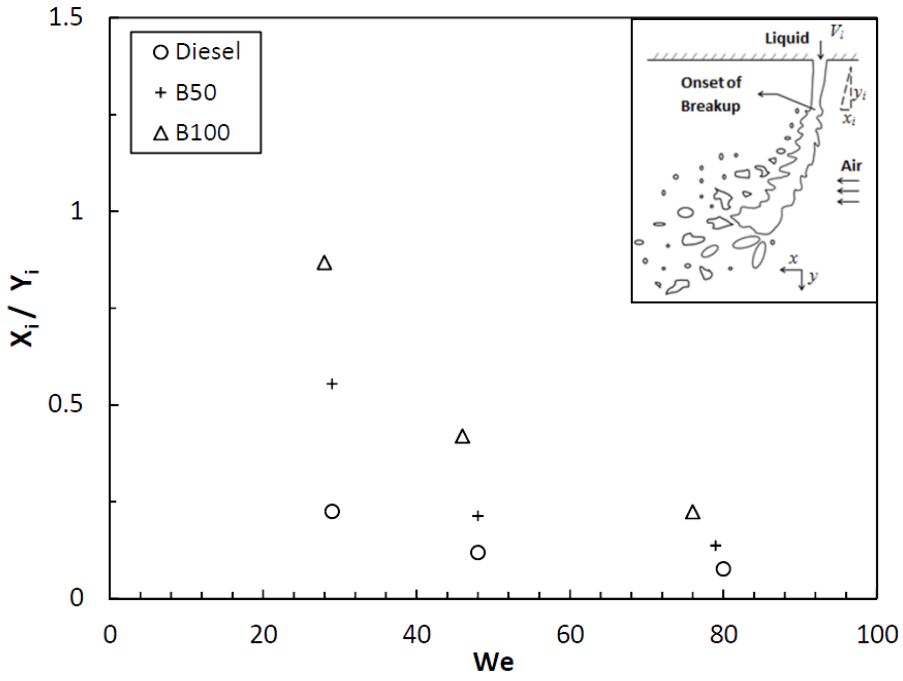


**Figure 2.7 Liquid column slope for diesel ($q$=50), B50 ($q$=49) and B100 ($q$=48) at different Weber numbers and momentum flux ratios**

Another important characteristic parameter in different regimes of breakup is the first liquid surface wave appearing on the windward side of the liquid jet. As mentioned in the literature review, the non-dimensionalized wavelength $\lambda_s/d_j$ for bag breakup ($We$<30) and

shear breakup (*We*>110) regimes are constant and equal to 1 and 0.1, respectively. On the other hand, $\lambda_s/d_j$ for multimode breakup regime (30<*We*<110) is between 1-0.1 varying with respect to Weber number. Figure 2.8 illustrates the wavelength of liquid surface waves for biodiesel and diesel.

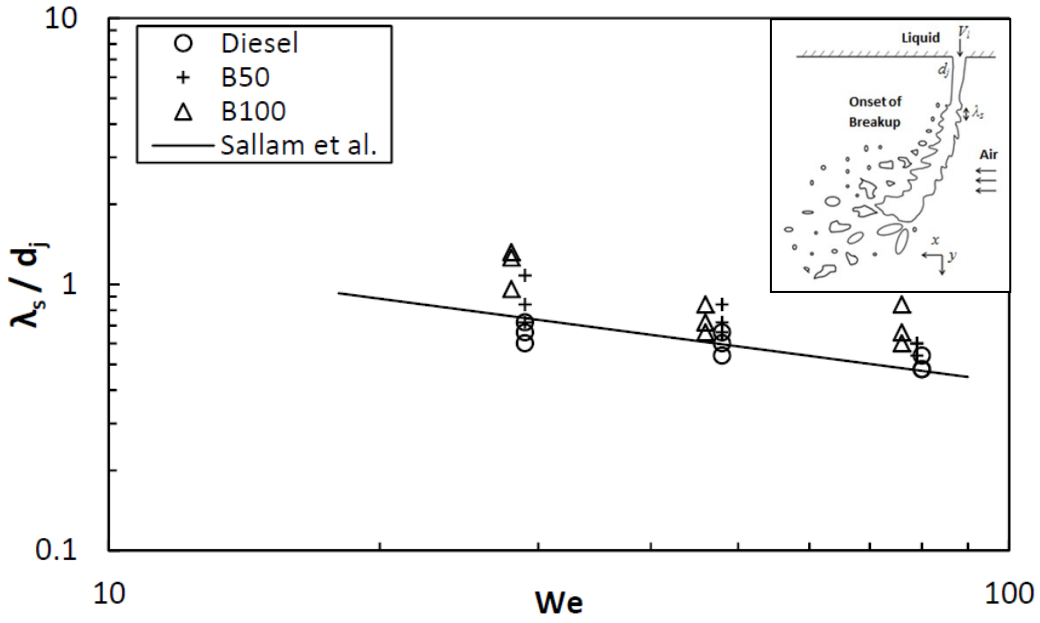


**Figure 2.8 Wavelength of surface instabilities on the windward side of the liquid jet for diesel, B50 and B100 at different Weber numbers and momentum flux ratios, compared with Sallam et al. [22]**

The results of Figure 2.8 show good agreement between the results of diesel wavelengths with the results of Sallam et al. [22] while biodiesel blends' wavelengths are higher than diesel. Considering $\lambda_s/d_j$ of bag breakup regime equal to almost 1, shows that biodiesel breakup is closer to bag breakup regime while diesel clearly lies on the region of $\lambda_s/d_j$<1 which is consistent with multimode breakup.

Considering the aforementioned discussion, the issue with the correlation of Stenzler et al. (Equation 2.2) is assumed to be the large viscosity range of different biodiesels. In

this regard, the kinematic viscosity of biodiesel blends is ranging between $1.4\times10^{-6}$ and $4.2\times10^{-6}$ $m^2/s$ for diesel and B100, respectively, while Stenzler's experiments cover $3.9\times10^{-7}$-$1\times10^{-6}$ $m^2/s$ for Acetone, 4-Heptanone, and Water. Hence, the power of viscosity and Weber number terms are considered for improvement, as the equation works well with the varying momentum flux ratio. Therefore, in this study, the correlation of Equation 2.2 is used as a base; however, the power of viscosity and the Weber number is corrected by performing a regression on the experimental results of diesel and biodiesel blends. Equation 2.3 shows the proposed trajectory for diesel and a wide range of biodiesel blends from B20 to B100.

$$\left(\frac{y}{d}\right)=3.688q^{0.430}\left(\frac{x}{d}\right)^{0.384}We^{-0.085}\left(\frac{\mu}{\mu_{H_2O}}\right)^{-0.222} \quad \textbf{Equation 2.3}$$

The improved form of trajectory for the range of biodiesel B5 to B100 and pure diesel are found to be as presented in Equation 2.3. The regression $R^2$ value for this equation is obtained 0.8 for the trajectories of B20, B50 and B100 test cases mentioned in the test matrix. It should be mentioned that Stenzler's equation, Equation 2.2, is still in agreement for Diesel and B5 cases, while for B20, B50, and B100, Equation 2.3 can give more accurate trajectories. As can be seen in this equation, for the above-mentioned range of tests, the power of viscosity term in the trajectory equation is higher (compared to a power of -0.108 proposed by Stenzler et al. [38]), providing more realistic results to reflect the effect of atomization of high viscous flows, such as high-percentage biodiesel blends.

As mentioned in the methodology, a validation experiment is performed for the above equation using the PDPA. The test matrix of PDPA is found with the reference

point at x=50 mm. Three additional points are captured under the reference point in order to assure the validity of the above equations. Using this methodology, the data counts at a specified duration (i.e., 60 sec), suddenly drops from 10000 at the reference points to one order of magnitude lower at the point just under the reference. This behavior, which is illustrated in Figure 2.9, agrees that the penetration of the spray is found by the above correlation at 50 mm downstream for the blends specified (i.e., B20, B50, and B100). The same validation is done for the Stenzler equation (Equation 2.2) for diesel and B5.

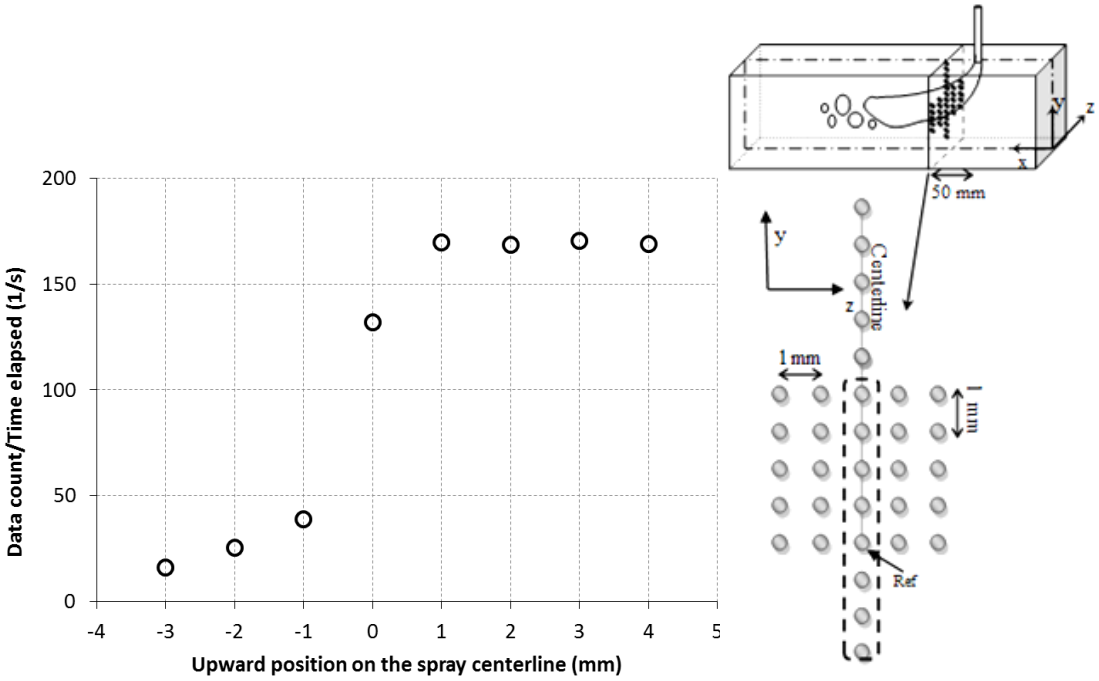


**Figure 2.9 Number of data per second captured by PDPA at different points on the centerline of the spray of B50, *We*=79, *q*=58**

Furthermore, PDPA is used for the measurement of droplet diameter, velocity, and volume flux. Figure 2.10 shows the contour of the Sauter mean diameter (SMD or $D_{32}$) of droplets at a Weber number of 80 and a momentum flux ratio of 82 for diesel. In addition, Figure 2.11 shows the SMD of B50 and B100 with the same heat of combustion

as diesel. It should be mentioned that zero in the vertical axis denotes the windward point of the spray 50 mm downstream of the injector (see Figure 2.2). Therefore, in the absolute coordinate system, the reference windward point of different blends is at different heights; however, the measurements are made with respect to the reference point up to 4 millimeters upward with 1 mm spacing. As can be seen in Figure 2.11, the droplets' Sauter mean diameters are similar for different blends within a ±10% range.

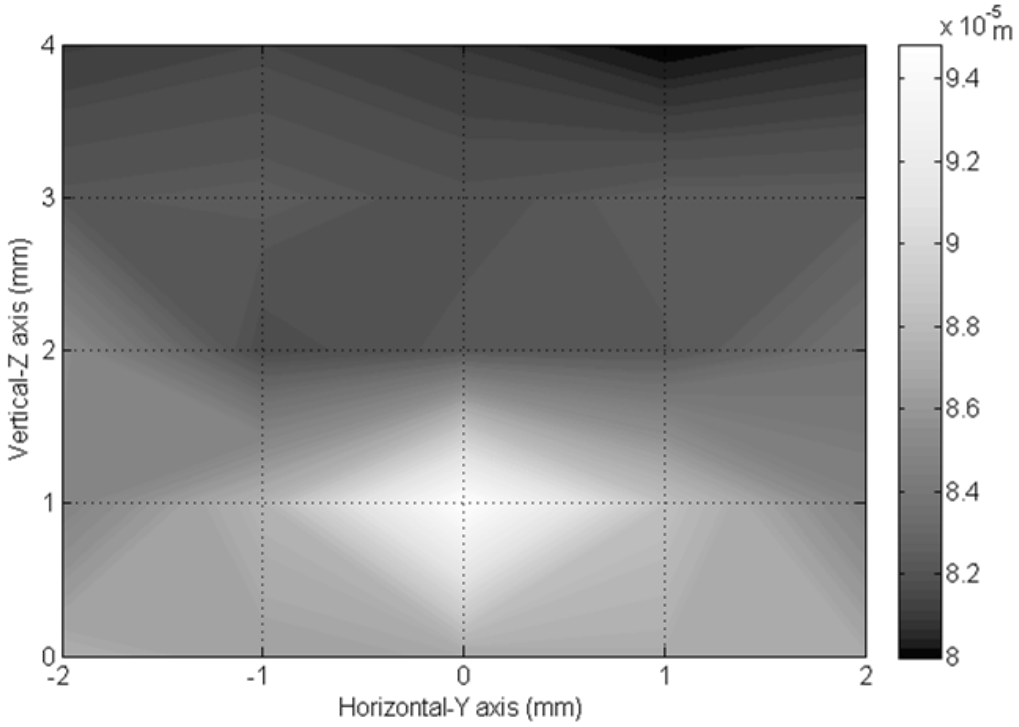


**Figure 2.10 Droplet SMD contour on the plane 2" downstream of the nozzle for diesel, *We*=80, *q*=82. Zero denotes the windward locus of the spray and measurements are taken at the grid crosses**

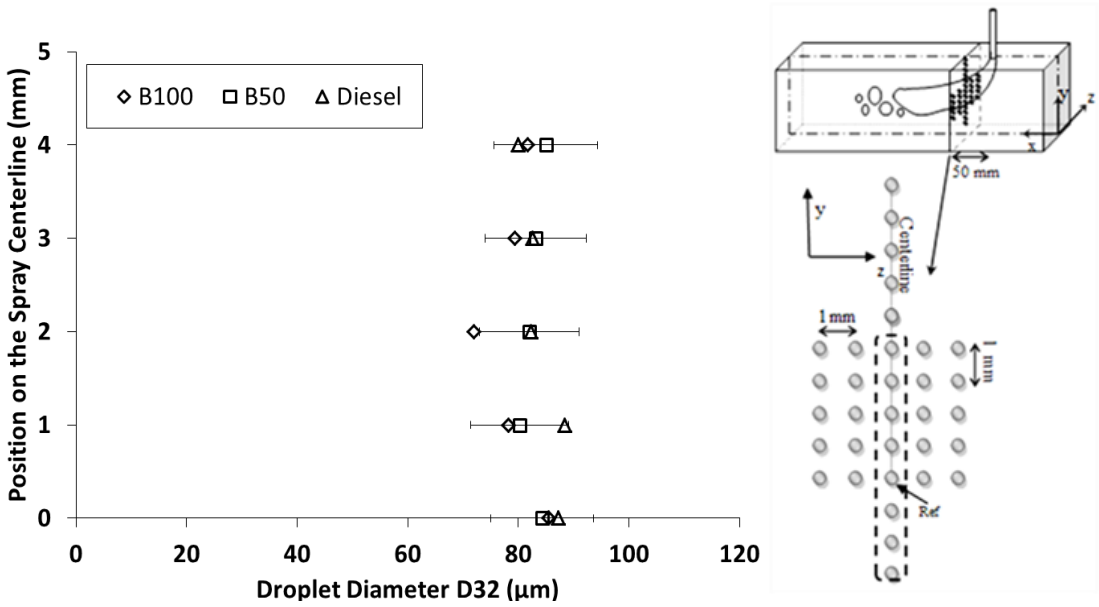


**Figure 2.11 Droplet diameter of diesel (*We*=48, *q*=100), B50 (*We*=48, *q*=115), B100 (*We*=46, *q*=133) at 50 mm downstream of the nozzle**

Figure 2.12 depicts a sample of the droplet size distribution of the spray 50 mm downstream of the nozzle for 2 or 3 mm above the reference point for various blends (Figure 2.12). In other words, the vertical axis in Figure 2.12 represents the percentage of the total drops captured with the diameter mentioned on the horizontal axis. Apparently, the distribution shape for different blends is identical; however, there are some changes in the values which are less than 10%. For example, in this figure, the droplet size of diesel seems greater than B50 and the droplet size of B50 seems greater than B100. According to Figure 2.11, this is not a unique behavior, and in some other results, the droplet diameter of B100 might be even greater than diesel. In this regard, it can be concluded that the droplet size of different blends of diesel and biodiesel is the same with a difference of ±10%. This fact shows that although different primary breakup modes exist, as shown in Figure 2.5, the secondary breakup process causes the droplet size to be the

same. Additionally, the droplet sizes of different blends have the same distribution against their spray trajectories, which differ remarkably. As discussed before, the trajectories of biodiesel show less penetration in comparison to the trajectories of diesel. This was reasoned to be a consequence of different primary breakup regimes and a different drag force on the jet column. For example, according to Figure 2.5, bag breakup mode is observed in biodiesel at a Weber number of 76, while in most fuel sprays, such as diesel at Weber numbers above 40, atomization mode is dominant in the primary breakup. On the other hand, Figure 2.11 and Figure 2.12 show the same droplet size distribution, 50 mm downstream, which means that after the secondary breakup, biodiesel and diesel sprays have the same droplet size distribution. In other words, the secondary breakup refines the spray of biodiesel and diesel identically, no matter what the difference their primary breakups may have.

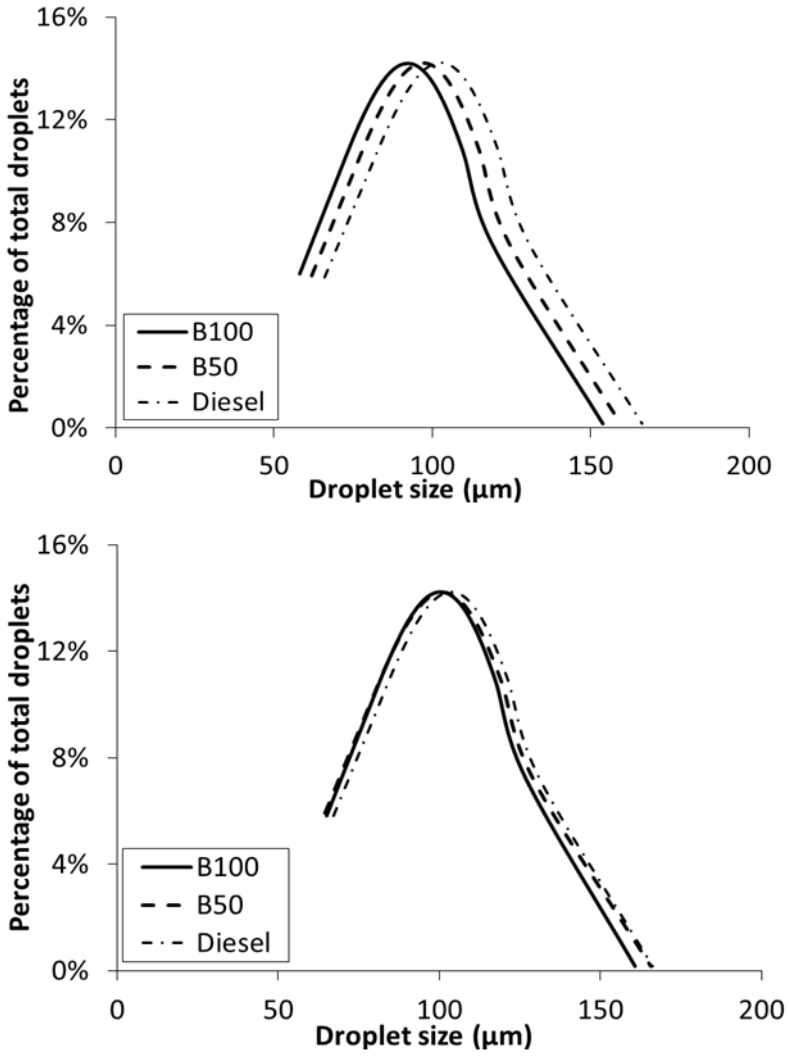


**Figure 2.12 Droplet size distribution of spray of diesel (*We*=48, *q*=100), B50 (*We*=48, *q*=115), B100 (*We*=46, *q*=133) 50 mm downstream of the nozzle and 2 mm or 3 mm (top and bottom graph, respectively) above the reference point**

Figure 2.13 illustrates the velocity of droplets normalized by the injection velocity for different blends from the windward reference point up to four millimeters upward. It is clear that the velocity of droplets is decreased as the concentration of biodiesel increases. The trend shows that droplets of B100 have lower velocities 50 mm downstream of the injector. Figure 2.5 can be used to explain the phenomenon where more bending and column shape change occurs like the bag breakup regimes for the jet

column of B100 compared to diesel. Also, as mentioned before regarding Figure 2.5, the change in the column shape in the case of B100 and B50, which makes the bag shapes, causes wider wakes upstream of the spray and consequently, larger turbulence intensity at 50 mm downstream. Hence, less drag force 50 mm downstream causes the droplets to accelerate less. Both Figure 2.5 and Figure 2.13 imply that most of the momentum exchange between the gas and the liquid jet is performed to bend the initial jet and there is less momentum residues for driving the droplets in the case of B100 compared to diesel. In the case of diesel, the jet column has bent less and there are more droplets shedding from the beginning of the jet issue point. It can be assumed that because of high viscosity in the case of biodiesel, the jet column becomes blunter after injection, causing it to have more drag and more momentum exchange at the jet column and consequently having less momentum residue for driving the droplets.

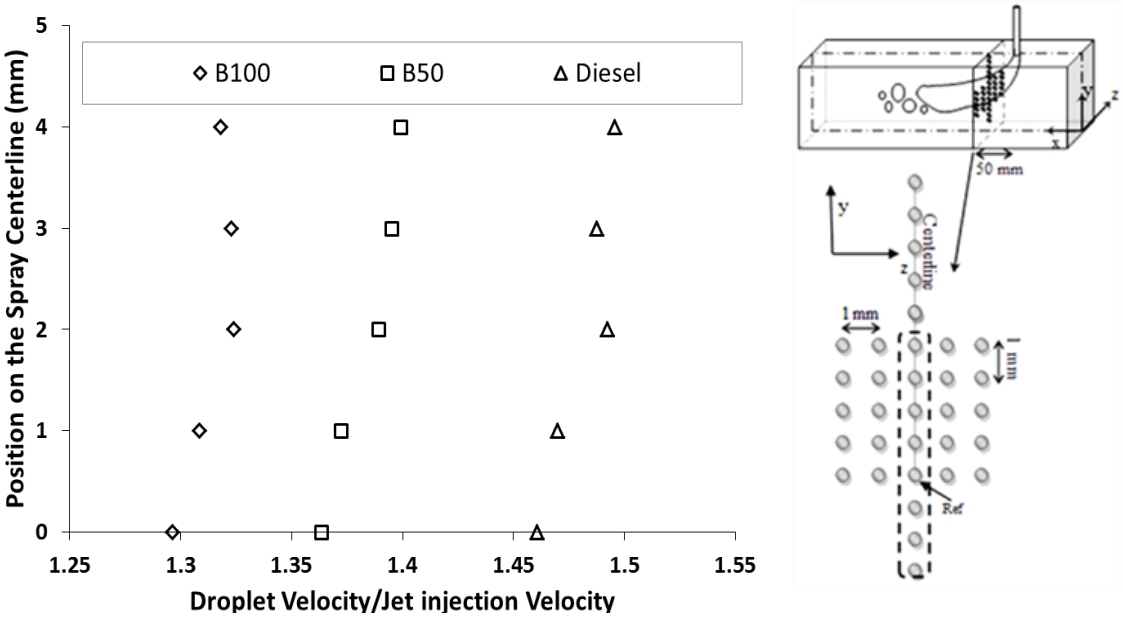


**Figure 2.13 Droplet velocity of diesel (*We*=48, *q*=100), B50 (*We*=48, *q*=115), B100 (*We*=46, *q*=133) at 50 mm downstream of the nozzle**

The normalized volume flux for different blends across the spray is shown in Figure 2.14. It should be mentioned that the flux is normalized by the total fluxes passing the 25 points shown in Figure 2.15. The trend shows that the flux of biodiesel sprays is more at the windward locations, while at upward points the diesel spray flux is more than the biodiesel blends. Keeping in mind that the droplet diameters are almost the same (Figure 2.11 and Figure 2.12), greater flux means having more droplets passed through a point. Therefore, for the biodiesel sprays, a higher flux zone is concentrated at positions near the windward trajectory and a lower flux zone is concentrated upward compared to the diesel spray. This behavior results in having better atomization and shear/stripping breakup of diesel compared to biodiesel blends. Once again, this shows a greater bag breakup regime, even at high Weber numbers, for the biodiesel blends – in comparison to diesel.

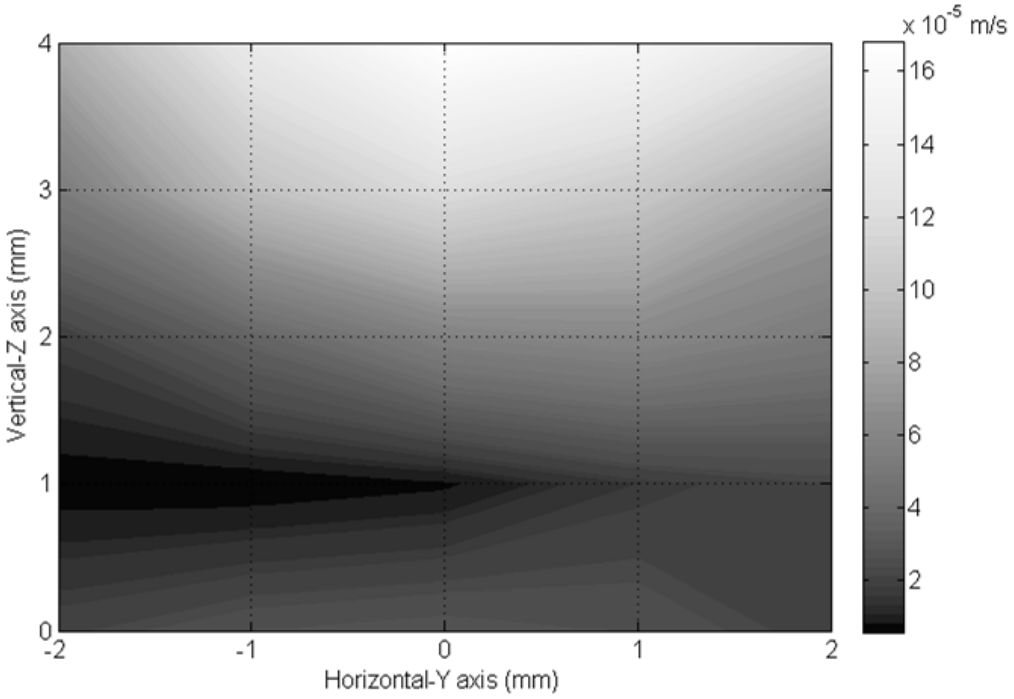


**Figure 2.14 Flux of diesel spray (m/s), *We*=48, *q*=100 at 50 mm downstream of the nozzle**

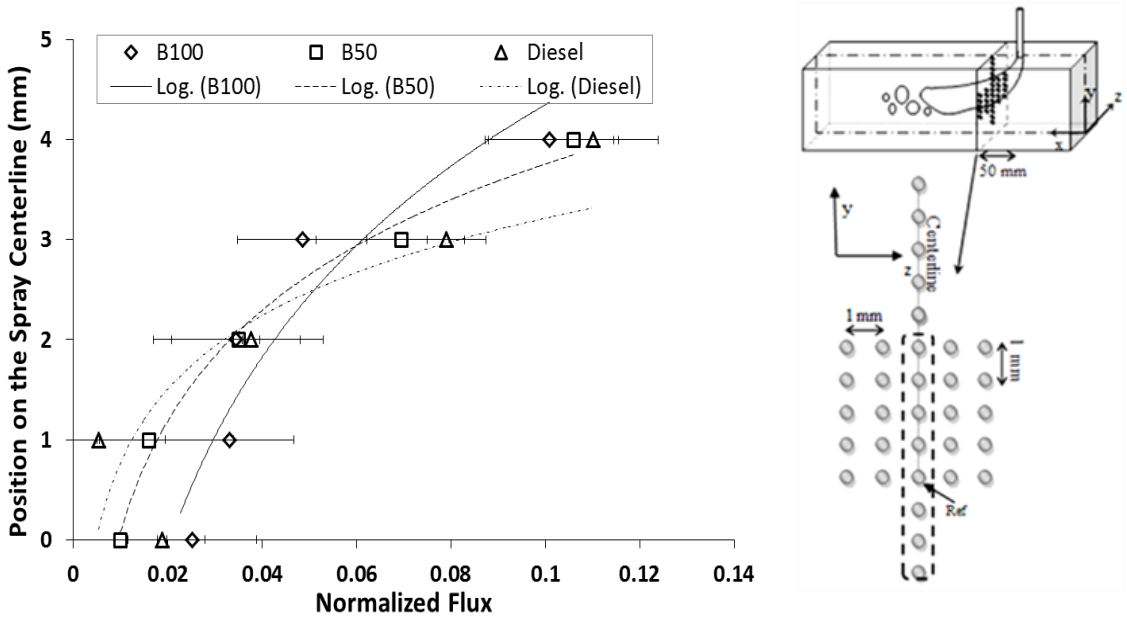


**Figure 2.15 Normalized flux of diesel (*We*=48, *q*=100), B50 (*We*=48, *q*=115), B100 (*We*=46, *q*=133) at 50 mm downstream of the nozzle**

## 2.4 Conclusion

The trajectories, onset of breakup, liquid surface instability, droplet size, velocity, and volume flux near the windward position of the spray have been compared experimentally for biodiesel blends and diesel liquid jets traversing subsonic air. The tests were done for several conditions in order to cover different Weber numbers and momentum flux ratios. The experimental results show a significant lower penetration depth of biodiesel jet in comparison to the diesel jet. This is determined to be due to the different breakup regimes of biodiesel and a larger drag of biodiesel liquid columns. Another possible parameter that may have effects on the trajectories is the orifice discharge coefficient, which is not addressed in this study. Based on the results of this study, an improved correlation was found for the penetration of biodiesel or any other liquids within the same range of viscosity and surface tension. Within this range, the

effect of viscosity is more pronounced, comparing to liquids such as water, diesel, and kerosene. In this regard, the effect of viscosity is thought to be a lag in the transition Weber number from bag shape breakup to multimode. This is illustrated by the larger wavelength instabilities on the liquid jet. This behavior translates into wider traverse area of liquid jet in crossflow that deflects the jet towards downstream. In terms of droplet size near the windward locus of the spray, the droplet sizes have identical distributions and the same value, with a variation range of ±10%. Having the same droplet size and distribution for various blends shows the same spray refinement quality after the secondary breakup while having different primary breakup and penetration depths. The droplet velocity is decreased as the concentration of biodiesel increases. This shows that droplets have experienced a lower drag force for biodiesel blends because of the primary momentum exchange with the jet column and wider wake after the biodiesel jet primary breakup. Furthermore, the volume flux of biodiesel spray is larger for the points near the windward trajectory in comparison to that of diesel spray; however, a lower volume flux is captured when traveling from the windward to the leeward side of the trajectory. The cause of this flux distribution, droplet velocity trend, and penetration is that the primary breakup regime of high viscosity fuels, such as high biodiesel blends, totally differs from regular fuels, such as diesel or kerosene.

## 2.5 Appendix

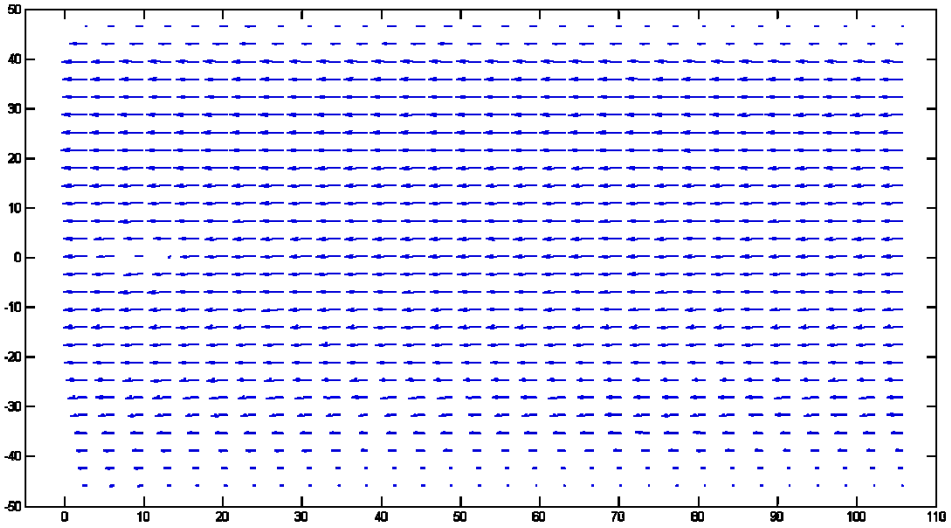


**Figure 2.16 Particle Image Velocimetry (PIV) characterization of the wind tunnel test section (25 mm plane from the top wall of the test section)**

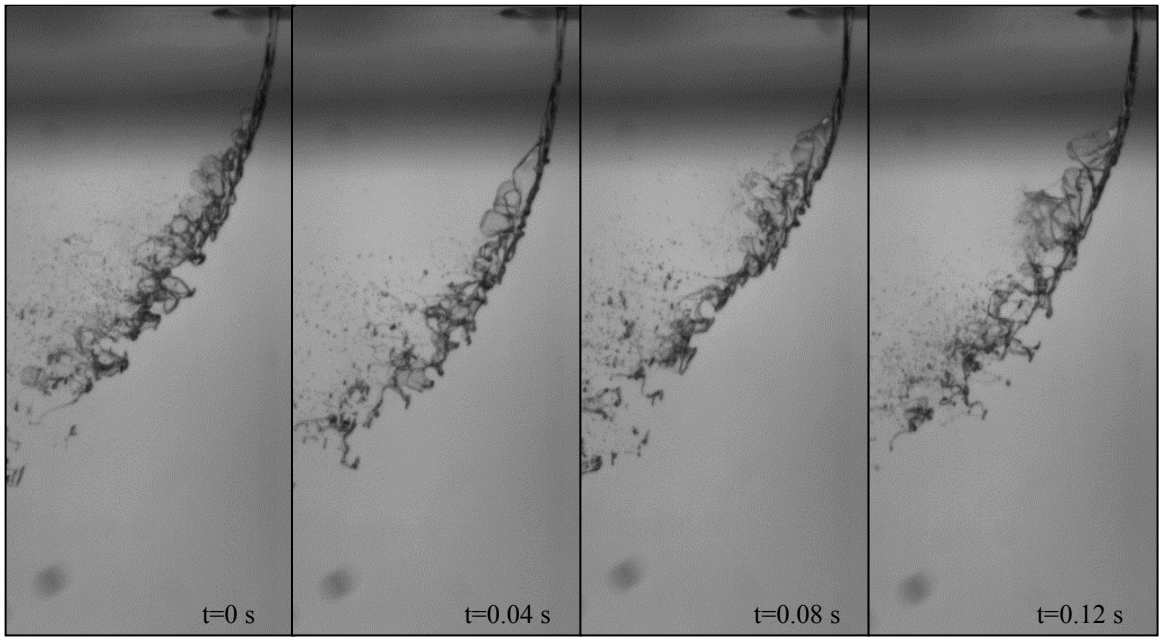


**Figure 2.17 Time series snapshots, B100, We=46, q=133**

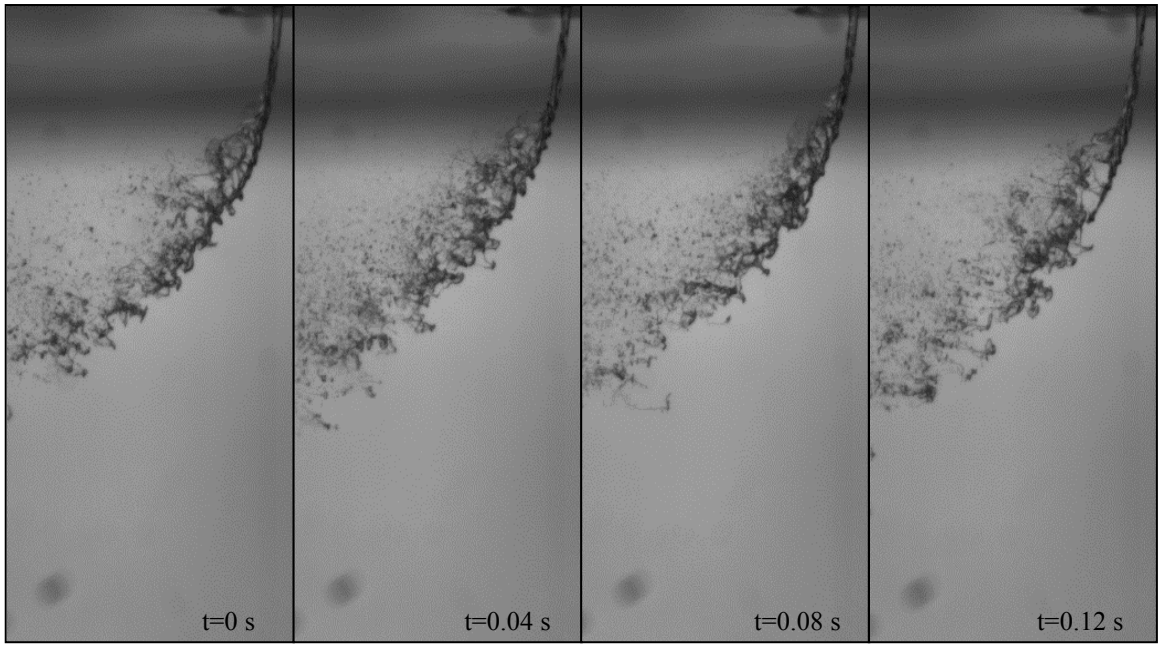


**Figure 2.18 Time series snapshots, B100, We=76, q=102**

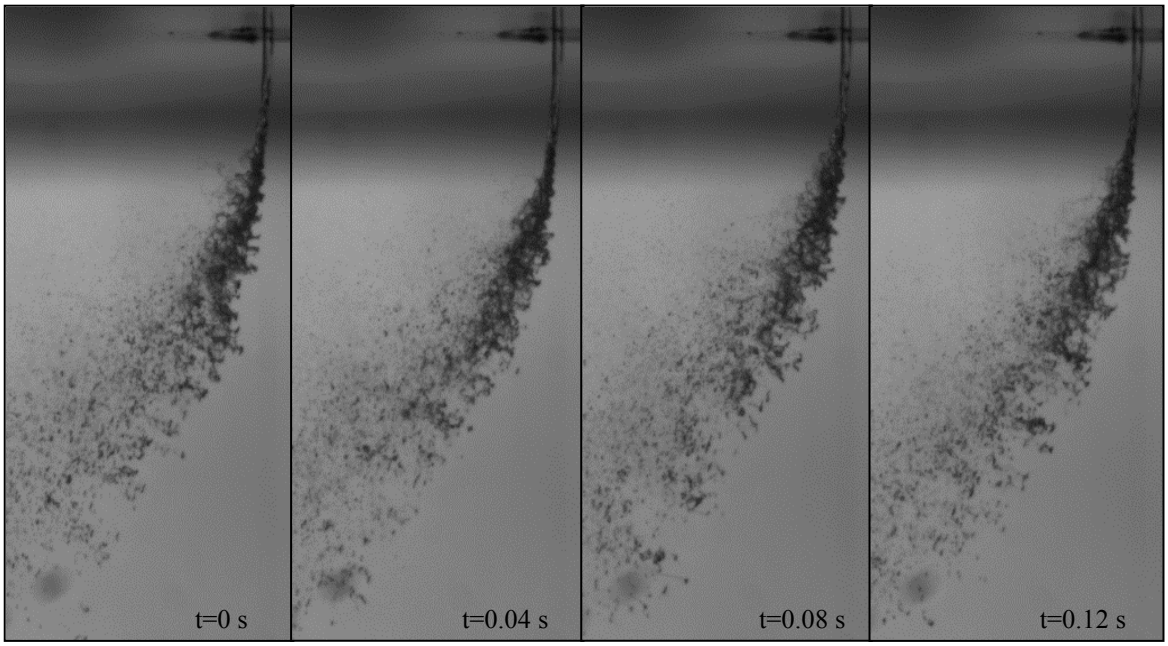


**Figure 2.19 Time series snapshots, diesel, *We*=48, *q*=100**

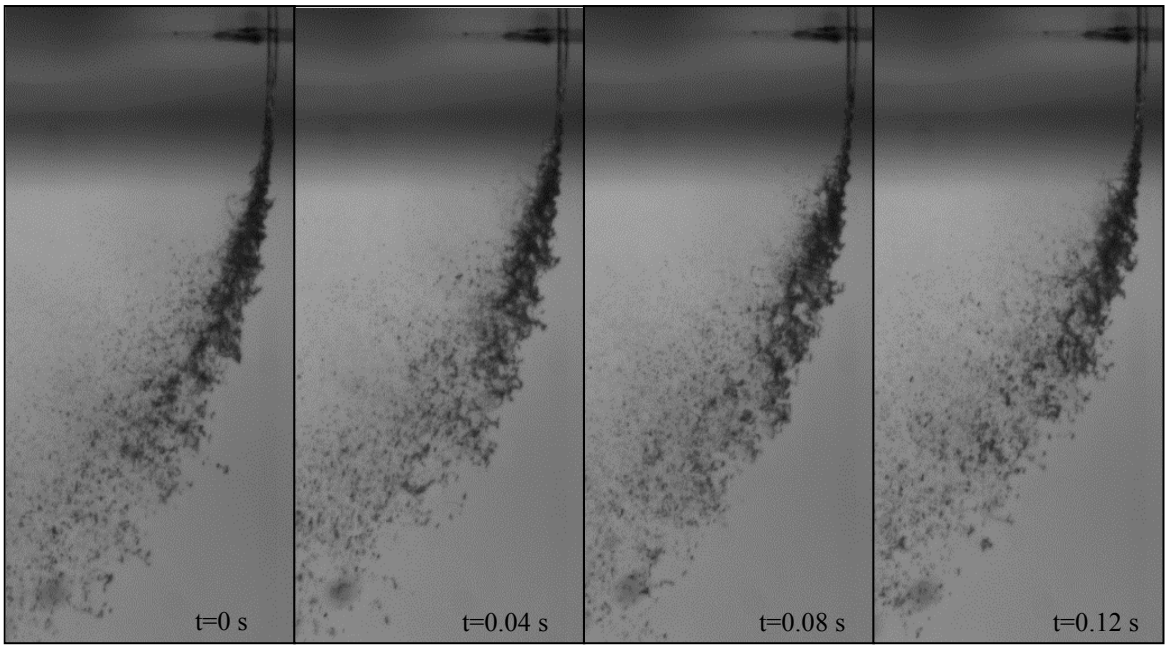


**Figure 2.20 Time series snapshots, diesel, *We*=82, *q*=100**

# Chapter 3

# Simulation of Liquid Jet of Biodiesel, Diesel and Their Blends in Cross Flow


## Abstract

Near field behavior of liquid jet in crossflow, i.e. deformation, primary breakup and penetration, is investigated. Biodiesel, diesel and their blend are used as the liquid jets entering the crossflow of air. In this study, the primary breakup of the liquid jet is simulated using the Volume of Fluid (VOF) numerical method. In order to, accurately, capture vortices including the horseshoe vortex in the gas, the liquid internal vortices and their effects on the liquid disintegration, Large Eddy Simulation (LES) turbulence model is coupled with the VOF and a dynamic mesh refinement method. The operating condition of this study is gas to liquid relative Weber number of 46-80 with liquid to gas momentum flux ratios ranging from 50 to 102. This work serves as a comparative study of biodiesel and diesel spray characteristics in crossflow. Liquid jet trajectory, surface waves and onset of breakup present a comparative study of the characteristics of liquid jet primary breakup in crossflow. Furthermore the droplet sizes are measured downstream of

the computational domain. The results show lower penetration depth of biodiesel comparing to diesel that agree well with the previous experimental work of the author.

## 3.1 Introduction

Liquid Jet in Cross Flow (LJICF) has many applications such as gas turbine combustion chamber, ramjets, scramjets and agricultural liquid dispensers. Furthermore, it can be served as a fundamental study of spray quality for different fuels as it illustrates jet disintegration, surface waves, primary and secondary breakups, effect of viscosity, effect of surface tension and the effect of density of the fuel on the final droplet size distribution, mixing, evaporation and combustion processes. In the last decade, scientists and industries have been attracted to the use of renewable energy such as biofuels [51]. Biodiesel as an alternative for diesel, which is already in use by many industries such as transportation and energy, played a pioneer role in this direction. Moreover biodiesel has different renewable resources such as Canola oil, cottonseed oil, animal fat, soybean oil, yellow grease and brown grease. Contrary to these advantages, the ignition, atomization and evaporation of biodiesel have been critiqued [30], [31]. In a recent comparative study [51], it has been shown experimentally that biodiesel has lower penetration depth comparing to diesel. The lower penetration depth is determined to be due to higher drag of biodiesel jet columns and different breakup regime map [51]. Moreover, larger wavelength instabilities are captured on the jet surface which is thought to be due to viscosity effects. In this numerical study, deformation, surface waves, and disintegration of a set of biodiesel blend jets issued from the same orifice are compared with those of a diesel jet.

Schetz and Padhye [32] experimentally studied the Liquid Jet in Cross Flow (LJICF), by conducting a series of tests in order to find a correlation between the jet column breakup, momentum ratio, drag coefficient and the fluids' length scales. In this regard, Wu et al. [33], [34], [35] and Mazallon et al. [39] classified the breakup map of LJICF in different categories, which are defined based on the gas-liquid Weber number. Mazallon et al. [39] visualized four different regimes of primary breakup, i.e. column, bag, multimode and shear breakup regimes. According to their study, the column breakup is called to a regime of breakup that results in the breakup of the jet to same diameter size droplets. In the bag breakup regime, the liquid jet is flattened from the sides and makes bag shape structures before breakup. In turn, in the multimode breakup regime, both bag shape structures and liquid ligaments appear after primary breakup. Finally shear breakup regime is defined when liquid ligaments and droplets are stripped off the liquid jet surface. Sallam et al. [22] performed an experimental study using shadowgraphy and holography. They found that the transition between various breakup regimes happens at $We$=4, 30 and 110 for the transitions to bag, multimode and shear breakup regimes, respectively. Several studies including Sallam et al. [22] use the liquid jet's surface wavelength, $\lambda_s$, as a characterization for the transition between different regimes of breakup. The wavelength $\lambda_s$, of the surface waves on the windward side of LJICF, is defined as the distance between each two nodes on the liquid surface. The wavelength non-dimensionalized with the original jet diameter, $\lambda_s/d_j$ for bag breakup regime ($We$<30) is equal to 1 [22]. This ratio, $\lambda_s/d_j$, for shear breakup ($We$>110) is almost 0.1 to be consistent for the formation of ligaments having a similar diameter as $\lambda_s$. Ultimately $\lambda_s/d_j$ for multimode breakup regime (30<$We$<110) varies between 1-0.1 due to complex

behavior of this regime ranging from bag to shear breakup. In addition to $\lambda_s$, Sallam et al. [22] used the onset of breakup as a classifying parameter of the LJICF breakup regimes. For example, they concluded that the ratio of jet diameter at the nozzle exit to the jet diameter at the onset of breakup ($d_j/d_i$) is equal to 2 and 1 at the bag breakup and shear breakup regime, respectively. In contrast, at the multimode breakup regime, this ratio ($d_j/d_i$) has a uniformly decreasing behavior from 2 (at *We*=30) to 1 (at *We*=110). Wu et al. [33], [34], [35] performed a set of experiments with water, glycerol and ethanol in order to investigate the effects of viscosity and surface tension. They correlated the windward trajectory of spray and breakup length to the momentum flux ratio. Birouk et al. [40] found that viscosity, greatly, affects the boundaries of breakup regime maps. In another study by Birouk et al. [41], the effect of viscosity on the liquid jet penetration is investigated. It, generally, resulted in having less penetration for more viscous liquid jets in crossflow. Following these works, Stenzler et al. [38] correlated the trajectory of LJICF with gas-liquid Weber number, liquid to gas momentum flux ratio and viscosity ratio. They tested liquids with various viscosities such as water, kerosene, acetone and 4-heptanone. In this vein, Farvardin et al. [51] modified the correlation of Stenzler et al. [38], by considering the high viscosity associated with biodiesel and its blends. They conducted a series of shadowgraph and PDPA experiments in order to find and compare the trajectories of LJICF. Diesel, biodiesel, and their blends were injected at different Weber numbers ranging from 11 to 80 and liquid-to-gas momentum flux ratios ranging from 10 to 135. Furthermore, they measured the onset of breakup, liquid jet column slope and wavelength of surface instabilities for diesel, biodiesel and their blends. They found a noticeable change in the trajectory of biodiesel jet in crossflow comparing to that of

diesel. As a result, the penetration of biodiesel is reported to be less than that of diesel. Biodiesel jets are found more flattened before the onset of breakup which is thought to be a cause of having higher drag force and ultimately less penetration. Accordingly, they concluded that the difference in the trajectories can be a result of the primary breakup and deflection of the jet column before the primary and secondary breakups [51].

In the numerical approach, Madabhushi [42] performed a series of Lagrangian particle tracking simulations of droplets in gaseous crossflow. For the gaseous part, he used a Reynolds Average Navier-Stokes set of equations coupled with $k$-$\varepsilon$ turbulence model. Although his results, generally, were in agreement with a similar experiment, most of the wakes and vortices, that have direct impact on the solution, were over-damped by the k-ε model. Therefore, in order to capture the gas-liquid two way effects, the interface tracking method and turbulence modeling were found as crucial techniques to resolve the simulation. Several interface tracking techniques such as Volume of Fluid (VOF), Refined Level Set Grid (RLSG), and Spectrally Refined Interface (SRI) were used by various researchers [52], [43], [44], [45], [46]. For example, Ng et al. [43] performed a Volume of Fluid numerical modeling of LJICF. Accordingly, they achieved a correlation between the wavelength, jet diameter and Weber number. A Refined Level Set Grid (RLSG) method is developed by Hermann [44]. He coupled his simulation with Large Eddy Simulation (LES) turbulence model. In addition, he combined his simulation with a Lagrangian two way coupled simulation for small and spherical droplets downstream of the jet primary breakup. Hermann [44] found two main mechanisms of liquid breakup in his simulations, i.e. Kelvin-Helmholtz instabilities and corrugations on the liquid jet surface. In the first mechanism, Kelvin–Helmholtz instability waves on the

liquid column produce roll-ups, which continue to propagate along the jet axis until they form bag-like structures. In the second mechanism, corrugations on the liquid jet surface are stripped off as stretched ligaments. Furthermore, Hermann et al. [45] investigated the impact of liquid/gas density ratio on the primary breakup of a liquid jet in crossflow. It was found that during breakup, the liquid core dynamics is affected significantly by the density ratio. In other words, an increase in density ratio leads to an increase in the liquid core penetration with reduced bending in the crossflow. This is in a manner that the post-primary atomization spray penetrates further in both the jet and transverse directions. Moreover, the wavelength of instabilities along the jet decreases by an increase in the density ratio. Regarding the wavelength of instabilities along the liquid jet, Pai et al. [46] performed numerical simulations using Spectrally Resolved Interface (SRI) method, emphasizing on the effect of Weber number on the wavelength. They found that decreasing the Weber number leads to an increase in the wavelength of disturbances.

In this study, the LJICF near field of the injection point is simulated numerically. The main aim of this work is to compare the primary breakup of biodiesel, diesel and their blend, in order to find out why biodiesel and its blends have different trajectories and subsequently penetration depth. In this regard, the same geometry of orifice and operating condition are used as the previous experimental study of the author [51]. The simulations are performed at Weber numbers 48 and 80 which represent the multi-mode regimes of liquid breakup in gaseous crossflow. In other words, the numerical simulations of this study are first validated by the experimental study (trajectory, instability waves, etc) of Farvardin et al. [51]. Furthermore, in order to capture the time/space dependency of LJICF, the numerical results are used to capture high

resolution ligament shapes, and droplet sizes. In this vein, not only the numerical results are validated, but also the restrictions of the experiments can be remedied to find additional characteristics.

## 3.2 Geometry and Boundary Conditions

Figure 3.1 schematically shows the computational domain and boundary conditions. The liquid jet is injected from a plain circular orifice of 0.5 mm diameter ($d$ = 0.5 mm). The orifice has an opening diameter of 2 mm for a length of 10 mm. Then a 45° conical chamfer directs the orifice internal flow into a 0.5 mm pipe. In order to assure a fully developed flow at the orifice exit, the length of 0.5 mm section of the orifice is considered 100×$d$. With the aim of capturing the effect of nozzle internal flow, disturbances and discharge coefficient, the flow inside the orifice is simulated separately for different Reynolds number and the orifice exit flow field is used as the boundary condition for the main LJICF study. Apparently, the orifice internal flow is modeled with the same LES formulations as described in the Methodology, but with much refined mesh that approximates the Direct Numerical Simulation (DNS) solution. In order to capture a wide domain around the near field of injection point, a domain of 10×40×40 times of the injector diameter is modeled in the lateral, horizontal and vertical directions respectively.

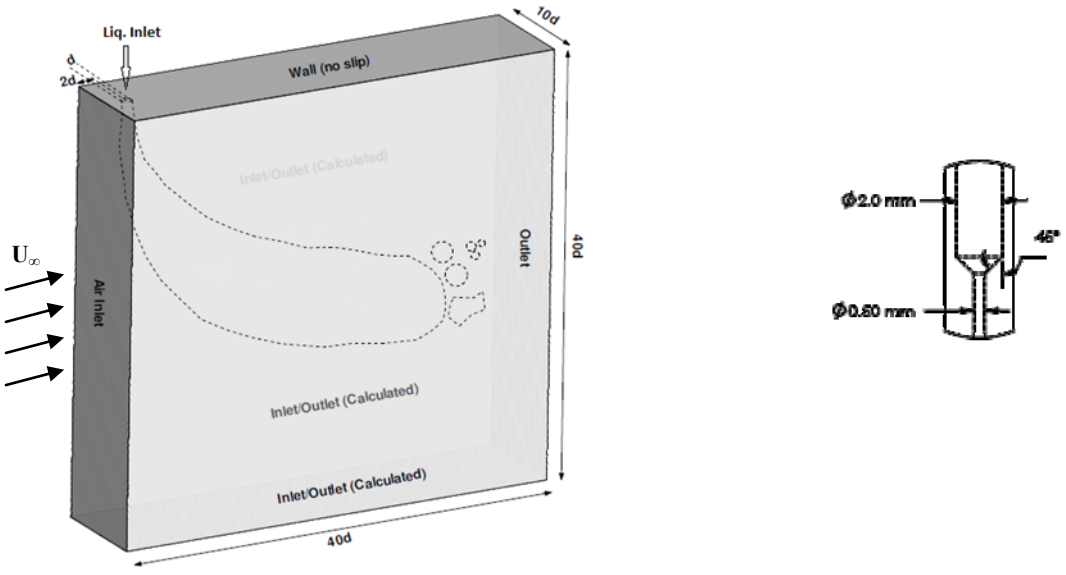


**Figure 3.1 Schematics of the computational domain. (Not to scale)**

As can be observed in Figure 3.1, the top wall is considered as a no-slip boundary condition (i.e. wall of the test section which is flush with the orifice exit) and the remaining lateral sides can be inlet or outlet of air/water depending on the calculated pressure, velocity and phase volume fraction at those faces. The original mesh size at the initial time step is 0.1 mm hexahedral; however the dynamic mesh refinement, which is elaborated in the Methodology section, refines the mesh size in the locus of air/water interface at each iteration.

Diesel, biodiesel (B100) and B50 blend are studied for several momentum ratios and Weber numbers. The blends are named based on the percentage of mass ratio of biodiesel to diesel. For example, B50 is made by 50% by mass of biodiesel added to 50% by mass of diesel. The physical properties of biodiesel (B100) are specified in Table 3.1 [49], [50]. Additionally, the properties of B50 are interpolated between the properties of diesel and B100.

**Table 3.1 Physical properties of diesel, biodiesel and blend**

| Properties | Diesel | B50 | B100 |
|---|---|---|---|
| Density (kg/m$^3$) | 850 | 867 | 884 |
| Surface Tension (N/m) | 0.0252 | 0.02615 | 0.0271 |
| Kinematic Viscosity (m$^2$/s) | 1.40E-06 | 2.8E-06 | 4.20E-06 |
| Heat of Combustion (kJ/kg) | 45757 | 42219 | 38681 |

As depicted in Table 3.1, the surface tension of B100 and B50 do not differ significantly from diesel; however the viscosity of B100 differs remarkably. In addition, the heat of combustion of B100 is almost 15% lower than the heat of combustion of diesel. Owing to this fact, in terms of comparison of two fuels, the mass flow rate of biodiesel should be higher than diesel in order to obtain the same heating value. This results into a biased operating condition as clarified in Table 3.2.

**Table 3.2 Operating Conditions**

| Parameters | Diesel | B50 | B100 |
|---|---|---|---|
| $V_g$ (m/s) | 45, 58 | 45, 58 | 45, 58 |
| $T_g$ (°C) | 20 | 20 | 20 |
| $We_g$ | 48, 80 | 48, 79 | 46, 76 |
| $q$ | 50, 82 | 58, 94 | 67, 102 |

## 3.3 Methodology

In order to compare the accuracy of the results and their agreement with the previous experimental study [51], two numerical models are used, Discrete Phase Model (DPM) and Volume of Fluid (VOF). The former one uses a Lagrangian aspect of the liquid phase. It solves the gas phase using Navier-Stokes set of equations and it tracks the liquid in form of discrete droplets from the injection point to downstream. Nonetheless, it captures the droplet secondary breakups, droplet deformation, evaporation and heat transfer, using empirical correlations. On the other hand, the latter model (VOF) is an Eulerian form of solving both liquid and gas phases using Navier-Stokes equations. It should be mentioned that the VOF method captures every details of the liquid/gas interface, although it does not model the heat/mass transfer among the fluid phases.

### *3.3.1 Discrete Phase Model (DPM)*

The Discrete Phase Model (DPM) numerical simulations were performed using Fluent 6.3. In order to model the penetration and windward trajectory of sprays, it is assumed that the droplets trajectory and their secondary breakup play more important roles than the primary breakup of the liquid jet column. Therefore Lagrangian Discrete Phase Model (DPM) was implemented. Taylor Analogy Breakup (TAB) model was used to calculate the breakup criteria at each time step. In addition, in the TAB model used for this study, the droplets are distorted from the spherical shape until they breakup into the child droplets. Hence, a dynamic drag model was applied in order to calculate the drag at each time step based on the new shape of droplets. The droplets at each time step can undergo two scenarios regarding the heat and mass transfer; heating before the vaporization temperature, and evaporation after the vaporization temperature. The whole test section is meshed and totally it contains 480,000 computational cells. The boundaries are wall on the test section and the inlet and outlet are simulated as velocity inlet and

pressure outlet, respectively. Air is modeled as an ideal gas with compressibility. Owing to low subsonic regime of gas, turbulence is modeled by *k-ω* equations.

### *3.3.2 Volume of Fluid (VOF)*

In order to capture the primary breakup, secondary breakup, column jet disintegration and liquid jet surface waves, the numerical modeling is performed using the Volume of Fluid (VOF) method. An incompressible, three dimensional, VOF solver for two immiscible Newtonian fluids, is used based on an OpenFOAM code [53]. In addition, Large Eddy Simulation (LES) turbulence model is utilized in order to accurately, capture the vortices upstream and downstream the liquid jet, its drag and consequently the jet penetration. An incompressible Navier Stokes set of equations is considered, including continuity and momentum equations with $\vec{v}$, $\rho$, $p$, $\mu$ and $g$ as velocity, density, pressure, viscosity and gravity (9.81 m/s$^2$), respectively.

$$\nabla . \vec{v} = 0$$ **Equation 3.1**

$$\frac{\partial}{\partial t}(\rho\vec{v}) + \nabla . (\rho\vec{v}\vec{v}) = -\nabla p + \nabla . [\mu(\nabla\vec{v} + \nabla\vec{v}^T)] + \rho\vec{g} + \vec{F}$$ **Equation 3.2**

It should be mentioned that density and viscosity in each cell are calculated based on the liquid to gas volume fraction of that cell ($\alpha$). As illustrated in Figure 3.2, the value of $\alpha$ is zero at the gas containing cells, one at liquid containing cells and between zero to one on the mixed containing cells [52]. Also the surface tension force, $\vec{F}$, on the interfacial cells is calculated as a function of surface tension $\sigma$, surface curvature κ and the gradient of volume fraction $\alpha$.

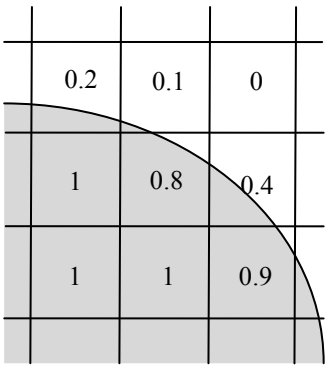


**Figure 3.2 Schematic of VOF method on computational cells**

$$\rho = \rho_l + \rho_g(1-\alpha) \quad \textbf{Equation 3.3}$$

$$\mu = \mu_l + \mu_g(1-\alpha) \quad \textbf{Equation 3.4}$$

$$\vec{F} = \sigma\kappa\nabla\alpha \quad \textbf{Equation 3.5}$$

$$\kappa = -\nabla.\left(\frac{\nabla\alpha}{|\nabla\alpha|}\right) \quad \textbf{Equation 3.6}$$

In order to account for the Large Eddy Simulation the Sub-Grid Scale (SGS) stress tensor comes from the nonlinear part of the convective term in the momentum equation. The SGS stress tensor can be approximated by means of the eddy viscosity definition and SGS kinematic viscosity. These two parameters in turn have a transport equation introduced by Yoshizawa and Horiuti [54].

$$\tau_{sgs} = \overline{vv} - \bar{v}\bar{v} \quad \textbf{Equation 3.7}$$

$$\tau_{sgs} - \frac{2}{3}k_{sgs}I = -\frac{\mu_{sgs}}{\rho}[\nabla\bar{v} + (\nabla\bar{v})^T] \quad \textbf{Equation 3.8}$$

$$\frac{\partial k_{sgs}}{\partial t} + \nabla.\left(k_{sgs}\bar{v}\right) = \nabla.\left[(\vartheta + \vartheta_{sgs})\nabla k_{sgs}\right] - \epsilon - \vartheta_{sgs}\bar{S}^2 \quad \textbf{Equation 3.9}$$

where in this equation ε, $\nu_{sgs}$ and S are found from the following relations.

$$\epsilon = \Delta C_\epsilon (k_{sgs})^{3/2}, \qquad C_\epsilon = 1.05 \quad \textbf{Equation 3.10}$$

$$\vartheta_{sgs} = \Delta C_k (k_{sgs})^{1/2}, \quad C_k = 0.07$$ **Equation 3.11**

$$\bar{S} = \frac{1}{2}(\nabla \bar{v} + (\nabla \bar{v})^T)$$ **Equation 3.12**

In terms of finding the interface of the two phases, in this study, a modified VOF method is used which has an additional convective term in the left hand side of the volume fraction conservation equation [54].

$$\frac{\partial}{\partial t}(\alpha) + \nabla.(\alpha \vec{v}) + \nabla.[\overrightarrow{v_r}\alpha(1-\alpha)] = 0$$ **Equation 3.13**

The last term in Equation 3.13, which is called artificial compression term, contains the compression velocity in order to avoid smearing of the phase interface [55]. In this equation, the term $\alpha(1-\alpha)$, has a non zero value in the cells just adjacent to the interface and zero on all other cells. This term is calculated based on the Rusche's model in several recent studies [56] and it captures the interface more accurately, while it has not a remarkable effect on the whole solution. The value of $\vec{v}_r$ in the vicinity of the interface is captured by Equation 3.14.

$$\overrightarrow{v_{r,f}} = n_f min\left[C_\alpha \frac{|\varphi|}{|S_f|}, max\left(\frac{|\varphi|}{|S_f|}\right)\right]$$ **Equation 3.14**

It should be mentioned that in Equation 3.14, $\varphi$, $S_f$, $C_\alpha$ and $n_f$ are the face volume flux, cell face area vector, compression coefficient (1.5 in Rusche's model [55]) and face unit normal flux respectively. The face unit normal also is defined by the equation below. In practical computation, due to avoiding zero value at the denominator of $n_f$, a small value of $\delta_n$ is used (eg. $10^{-5}$).

$$n_f = \frac{(\nabla\alpha)_f}{|(\nabla\alpha)_f + \delta_n|}$$ **Equation 3.15**

In addition, to solve the problem by means of the above formulation, for accurate tracking of the liquid interface, its surface waves, and breakup phenomenon, the interface has been captured by a dynamic adaptive mesh refinement method [53]. As illustrated in Figure 3.3, the cells with volume fraction between 0.01 and 0.99 are refined while the rest of the mesh is retained at the original size. In this manner, the liquid-gas interface cells become finer at each iteration; however to have a reasonable computational time, a limit of maximum three refinement levels has been applied for each cell. Furthermore, a limiter of 10,000,000 cells for the whole domain mesh after the final refinement has been implemented.

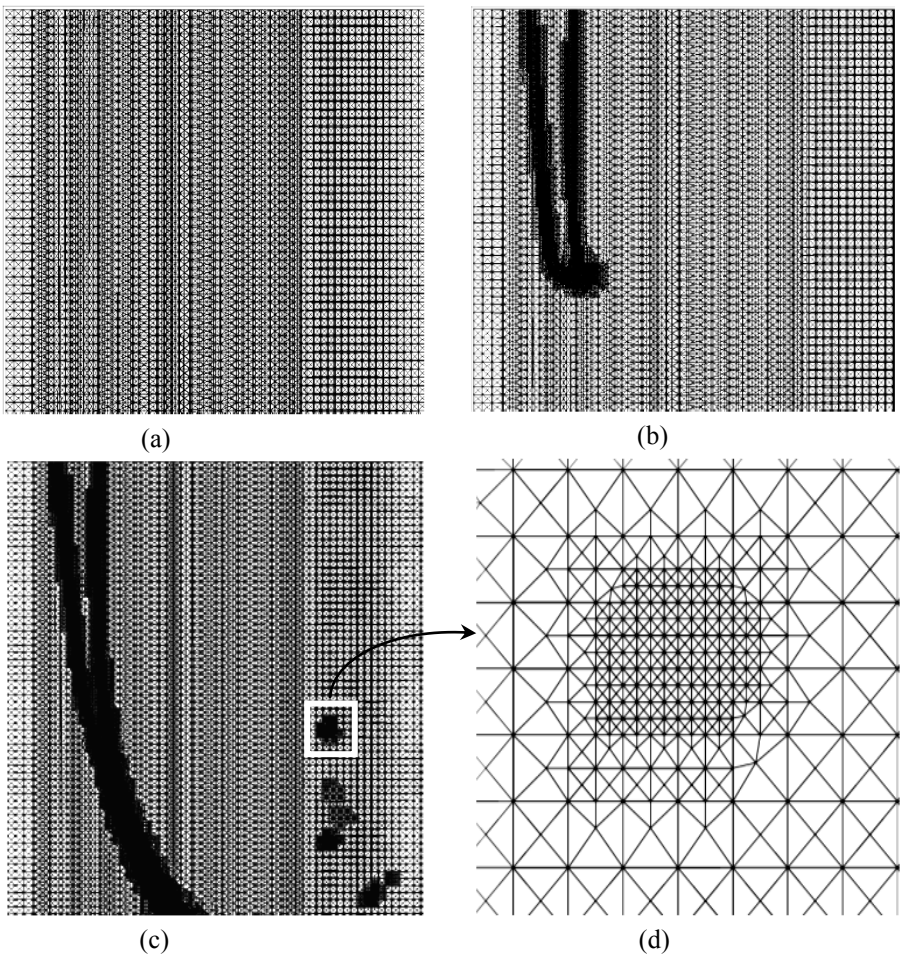


**Figure 3.3 a), Initial mesh cut-off, containing the injector exit, b) dynamic refined mesh of cells with $0.01<\alpha<0.99$ (interface) at an intermediate time step, c) dynamic refined mesh of cells with $0.01<\alpha<0.99$ (interface) after liquid jet advancement, d) a close-up of mesh refinement**

The coupled set of Navier-Stokes equations is solved for unsteady cases with a default time step of $1\times10^{-5}$ seconds. The time step however is adjusted by a Courant number of 0.5 or less. In terms of post-processing and visualization, in order to get a better comparison, the numerical results also are post processed with ParaFoam software [57] and the liquid interface meshes are rendered by Blender open-source software [58].

## 3.4 Results and Discussion

Figure 3.4 shows the windward trajectories of diesel, biodiesel, and B50 for air velocities of 45 and 58 m/s. In addition, the DPM numerical results and the correlation of Stenzler *et al.* [38] are illustrated in this figure. As can be seen in Figure 3.4, the DPM numerical results of diesel trajectory show good agreement with the experimental results, wheras the DPM numerical results of biodiesel are deviated from the experimental trajectories. In other words, the higher the concentration of biodiesel in the blends, the lower the accuracy of the DPM numerical results. One of the reasons of this discrepancy originates from the use of Taylor Analogy Breakup (TAB) model. In fact this model simulates the liquid as a spring-mass system with viscosity playing as damper role. Since the damper is a first derivative in the mass-spring formula, the high viscosity of biodiesel and its blends can become less dominant factors and their breakup and trajectories are influenced accordingly.

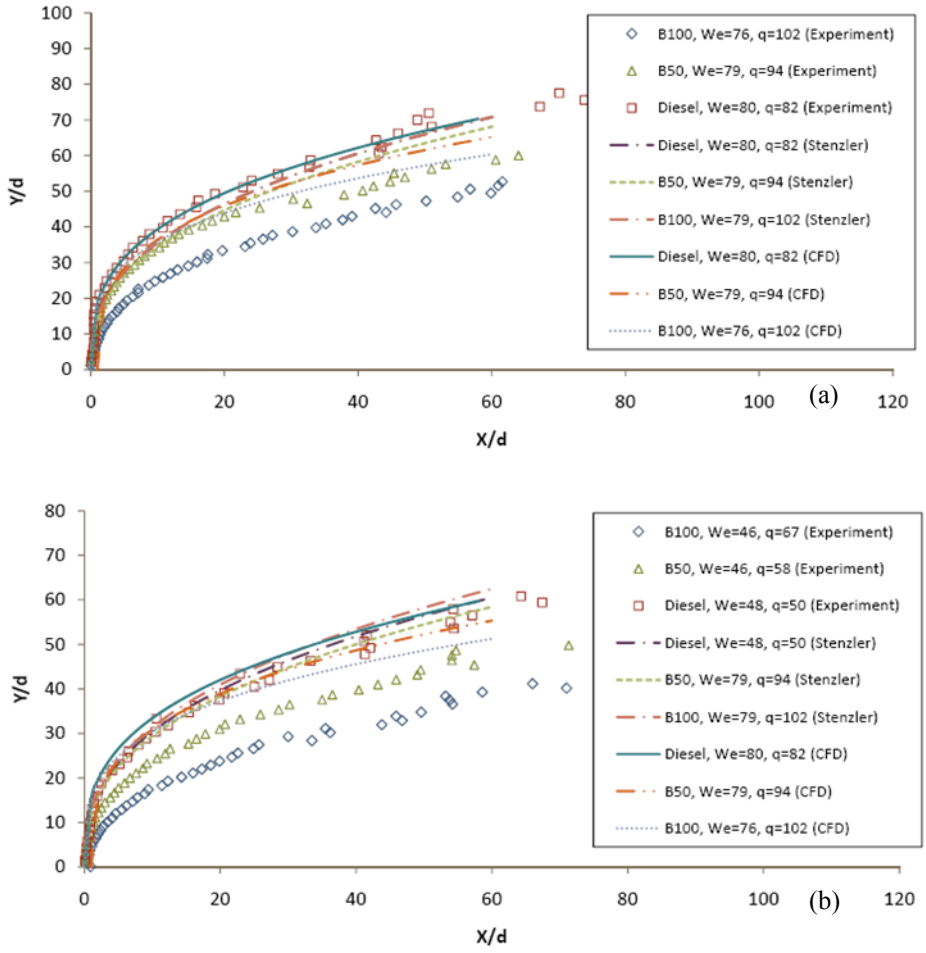


**Figure 3.4 Experimental, DPM numerical and empirical trajectories [59]**

The VOF numerical trajectory of biodiesel and diesel are illustrated in Figure 3.5. In addition, the experimental shadowgraphs of the same operating condition [51] are depicted in the same figure for comparison. It should be mentioned that in the rest of this thesis for conciseness, “numerical results” shortly, refers to VOF numerical results, while DPM results are always mentioned as DPM numerical results. As can be seen, biodiesel jet has more bag shaped ligaments at the windward side of the jet. This fact is clear in the simulation results as well. Furthermore the biodiesel jet column in comparison to the diesel jet, in either the experimental and numerical results, has bent more before the

column breakup. This behavior is thought to be a result of experiencing higher drag on the biodiesel jet.

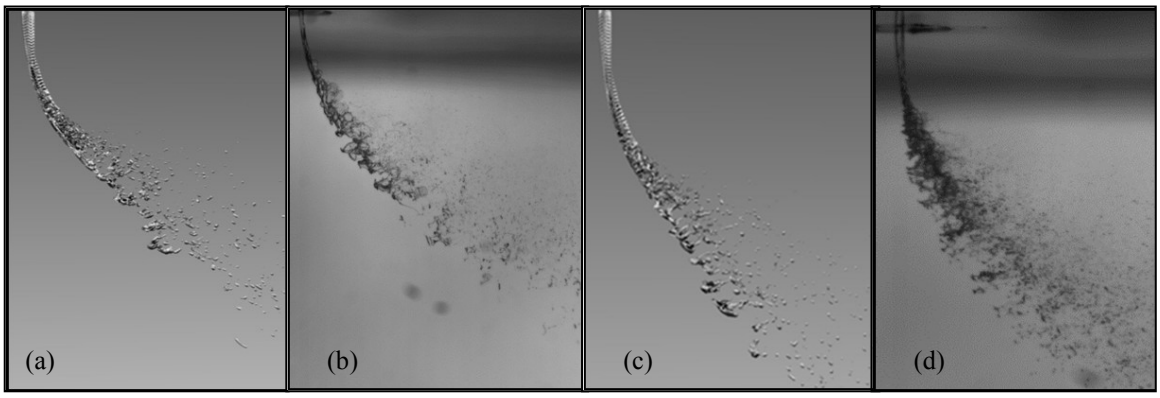


**Figure 3.5 Numerical and experimental trajectories at *We* = 48, *q* = 100 a) numerical, B100, b) shadowgraph, B100 [51], c) numerical diesel, d) shadowgraph diesel [51]**

Figure 3.6 shows velocity contours at different sections of the computational domain. As can be observed in this figure, there are stronger and wider wakes surrounding the biodiesel jet comparing to the diesel jet. Therefore the drag force causing by these wakes, can be translated into bending of the column jet of biodiesel. It should be mentioned that B50, which is not shown in Figure 3.5 has an intermediate behavior between B100 and diesel in terms of jet bending and bag shape ligaments.

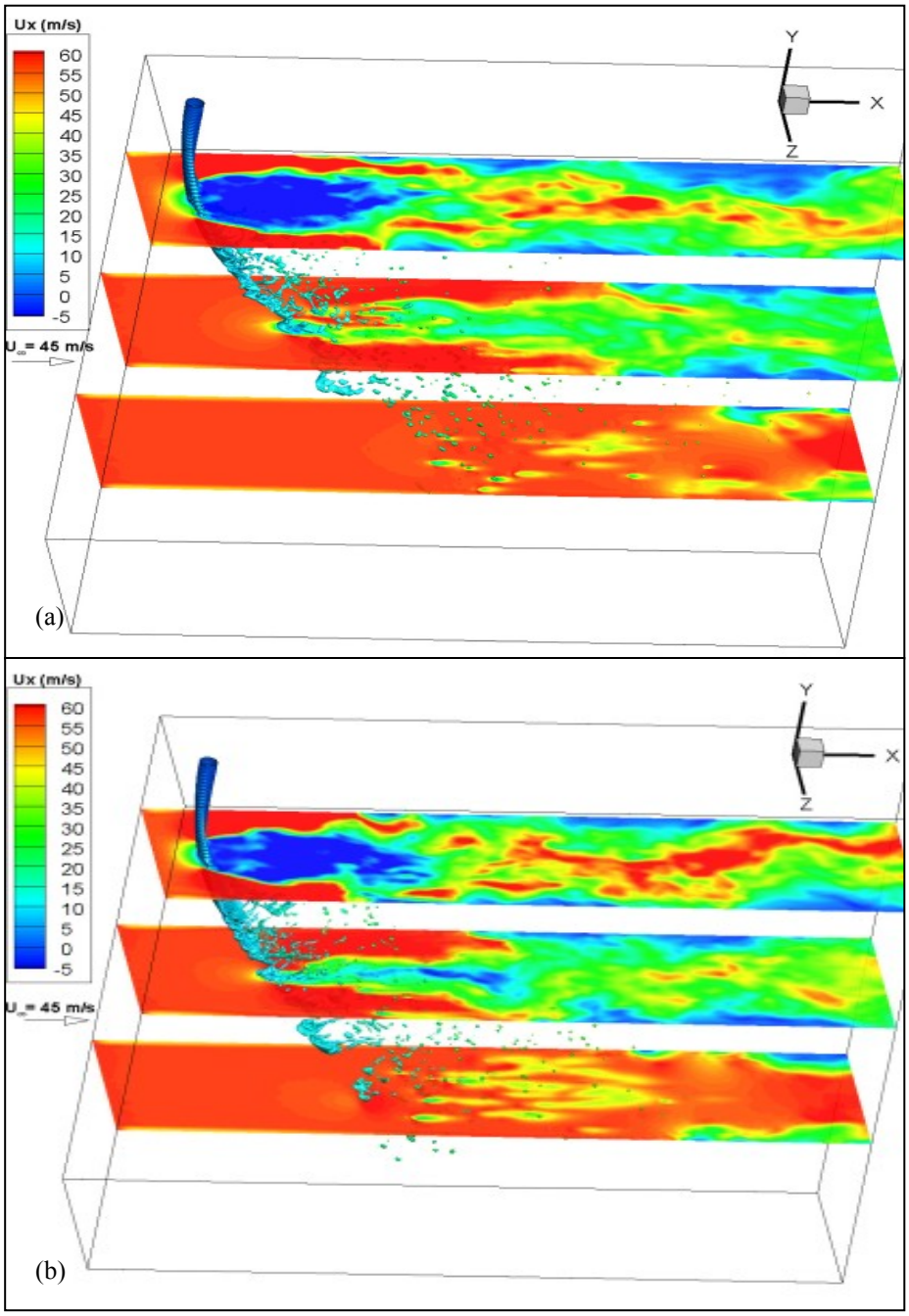


**Figure 3.6 Velocity contours at *We* = 48, *q* = 100, a) B100, b) diesel**

Another interesting result is having more bag shape ligaments in the biodiesel spray comparing to the diesel spray as a result of primary breakup. This fact is clearly illustrated in Figure 3.7 that shows the liquid interface near the windward trajectory and

just after the primary breakup. Having these bag shape ligaments at $We$ = 48, which is commonly known as the multimode regime, depicts how the high viscosity of biodiesel and its blends affects the primary breakup regime of biodiesel.

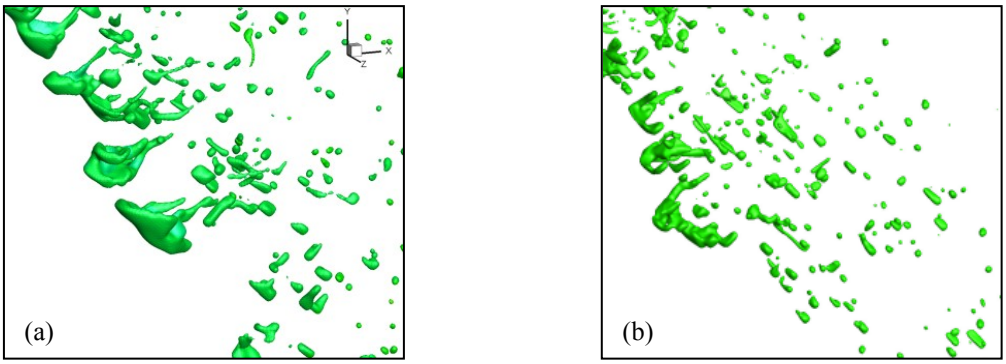


**Figure 3.7 Snapshots of a) biodiesel and b) diesel just after the primary breakup**

Figure 3.8 demonstrates the maximum velocity of droplets downstream of the computational domain, i.e. 40×$d$ or 20mm downstream of the injection point. Apparently, at the same operating condition, the diesel droplets have higher maximum and the B50 and B100 have lower maximum velocities respectively. These results once again confirm having stronger and wider wakes surrounding the biodiesel jet that consequently affects its droplets having lower velocities.

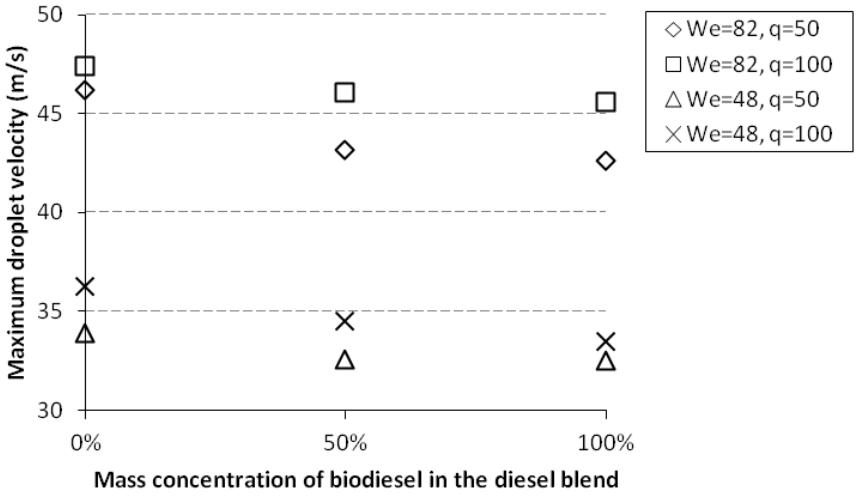


**Figure 3.8 Maximum velocity of downstream droplets for diesel, B50 and B100 at different operating conditions**

The windward trajectories of different liquids are shown in Figure 3.9. As can be seen, the results of the numerical simulation are in good agreement (<±10% difference) with the experimental results [51]. Also it is clear that the maximum error of numerical results appear typically, downstream of the domain. This can be due to the oscillatory behavior of the windward trajectory in different time steps at downstream locations where mostly, contains small droplets. It should be mentioned that the numerical trajectories of Figure 3.9 are the windward trajectories of the last numerical time step, while the experimental results of Figure 3.9 are an average of windward trajectories in 500 shadowgraph snapshots [51]. As another remarkable result in Figure 3.9, both the experimental and numerical results depict a decrease in the penetration depth from diesel to B50 and B100. This behavior of the penetration depth for diesel, B50 and B100 can be translated in change of the spray mixing locus in the engine applications.

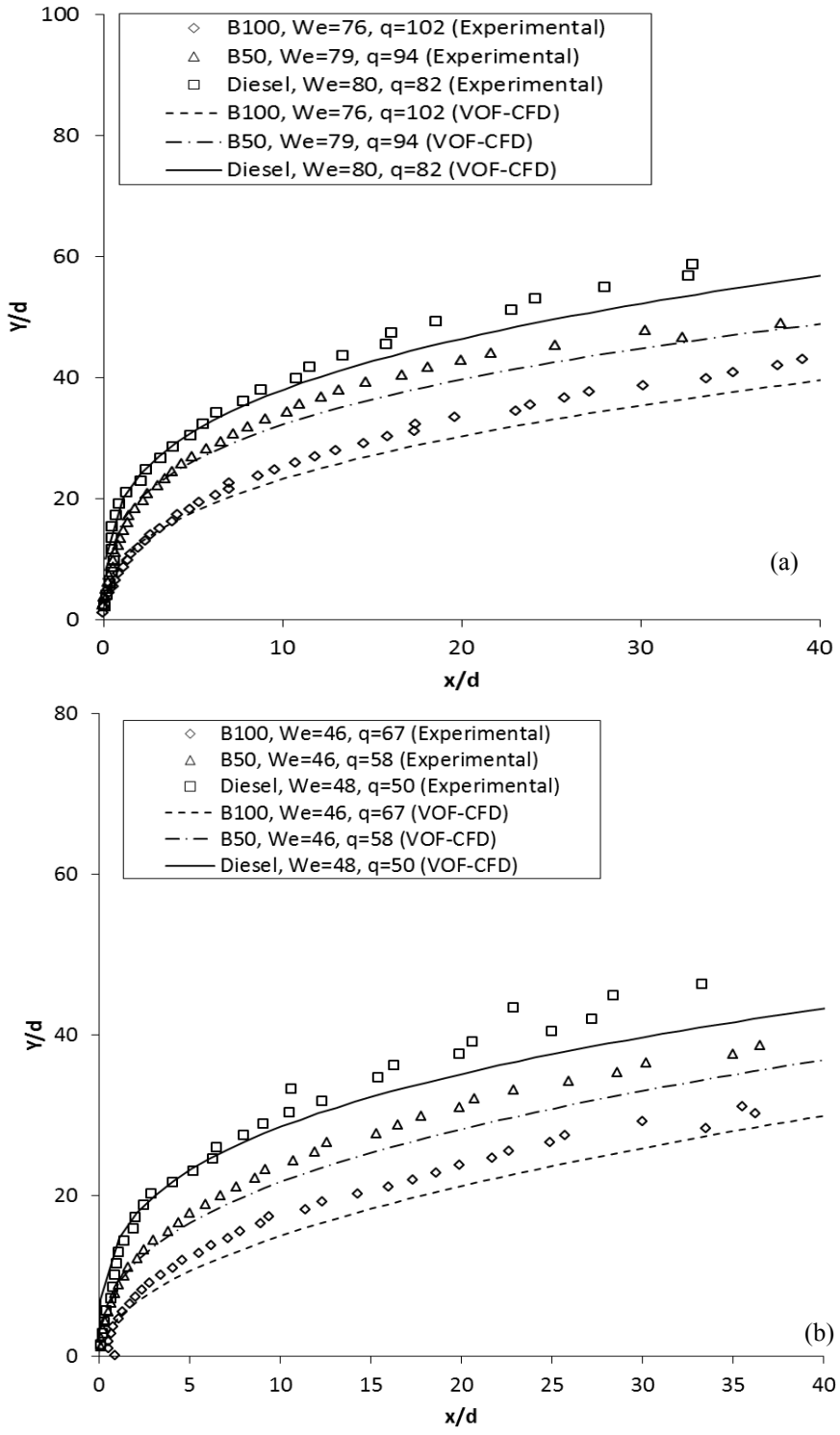


**Figure 3.9 Numerical and experimental trajectories of diesel, biodiesel and their blends at different Weber numbers and momentum ratios**

Figure 3.10 shows the comparison of different numerical methods with the experimental results [51]. Farvardin et al. [59] also performed a Lagrangian numerical simulation with the Discrete Phase Model (DPM) method. In the DPM method, the liquid part is not solved as a bulk fluid by the Navier Stokes equation. Instead the liquid part is modeled as a series of discrete droplets with a specified size at the injector exit. Subsequently, a set of empirical relations governs the discrete droplets in terms of secondary breakup, deformation, evaporation, etc. For example, in the above mentioned paper, they used Taylor Analysis Breakup (TAB) method to simulate the breakup of initial spherical droplets as in a spring-mass system. As a result and as mentioned in [51], this type of simulation, does not predict the penetration depth very well due to column jet bending, surface waves and primary breakup effect which are not modeled in DPM. In this study, the progress of the simulation results from DPM to VOF is shown in Figure 3.10. The VOF simulation results are significantly closer to the experimental results (±10% accurate) in comparison to the DPM results [51] (±35%).

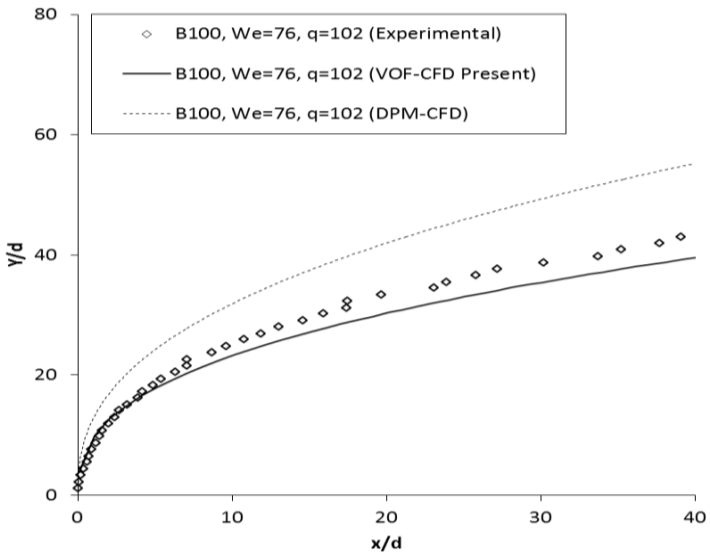


**Figure 3.10 Comparison of different numerical simulations (VOF as present work and DPM as the previous work of the author [51]) with the experimental results**

Figure 3.11 shows the slope of the jet column between the nozzle exit and the onset of breakup (subscript *i* denotes the properties at the onset of breakup). Diesel, B50 and B100 trajectories show decreasing behaviour for the jet column slope by increasing the Weber number. Since the regime of breakup in this study is multimode regime, by increasing the Weber number it is expected to have less bag shape structures and more sheared ligaments.

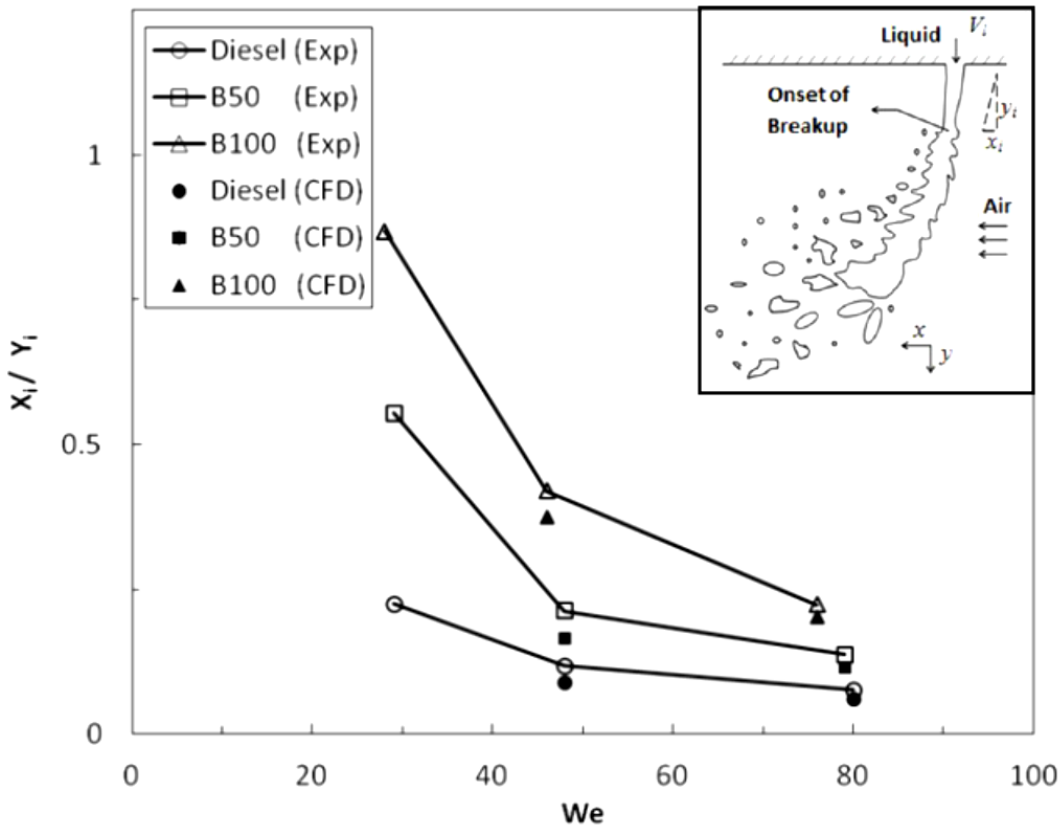


**Figure 3.11 Jet column slope at the onset of breakup, $q$=50, experimental [51] vs. numerical**

Therefore for each liquid by increasing the Weber number, less bag shapes are formed, that leads to have less surface drag and straighter jet. In comparison between diesel, biodiesel and their blends, the slopes of B100 at each specified Weber number is

larger than B50 and B50s' are larger than diesel. Once again, this behaviour shows having higher drag for B100 jets comparing to diesel. In turn having higher drag depicts more flattening of the jet column which can be translated as having more bag shapes in B100 and B50. It should be mentioned that generally the results agree well with the experiments [51]. The difference between the numerical and the experimental results [51] are thought to be due to having coarse mesh near the top wall where the jet is issued from. Actually, the mesh refinement in this study is performed at the liquid jet interface where the volume fraction is between 0.01 and 0.99 while the mesh is remained unrefined adjacent to the top wall. Therefore the boundary layer cannot be predicted accurately. As a result, a small difference between the computational and experimental results is inevitable.

The jet diameter at the orifice exit ($d_j$) normalized by the side-thickness of the jet ($d_i$) at the onset of breakup is illustrated in Figure 3.12. As can be seen, the results agree well with the experimental results. Apparently, the value of $d_j/d_i$ for B100 is higher than B50 and B50 is higher than diesel. Since the value of $d_j$ was fixed during this study, it means that B100 jet has become thinner, viewing from the side, which translates into becoming more flattened at the onset of breakup. In other words at the same Weber number, the biodiesel jets make more bag shapes at the onset of breakup or its bag shapes burst later which both pronounce the effect of higher viscosity.

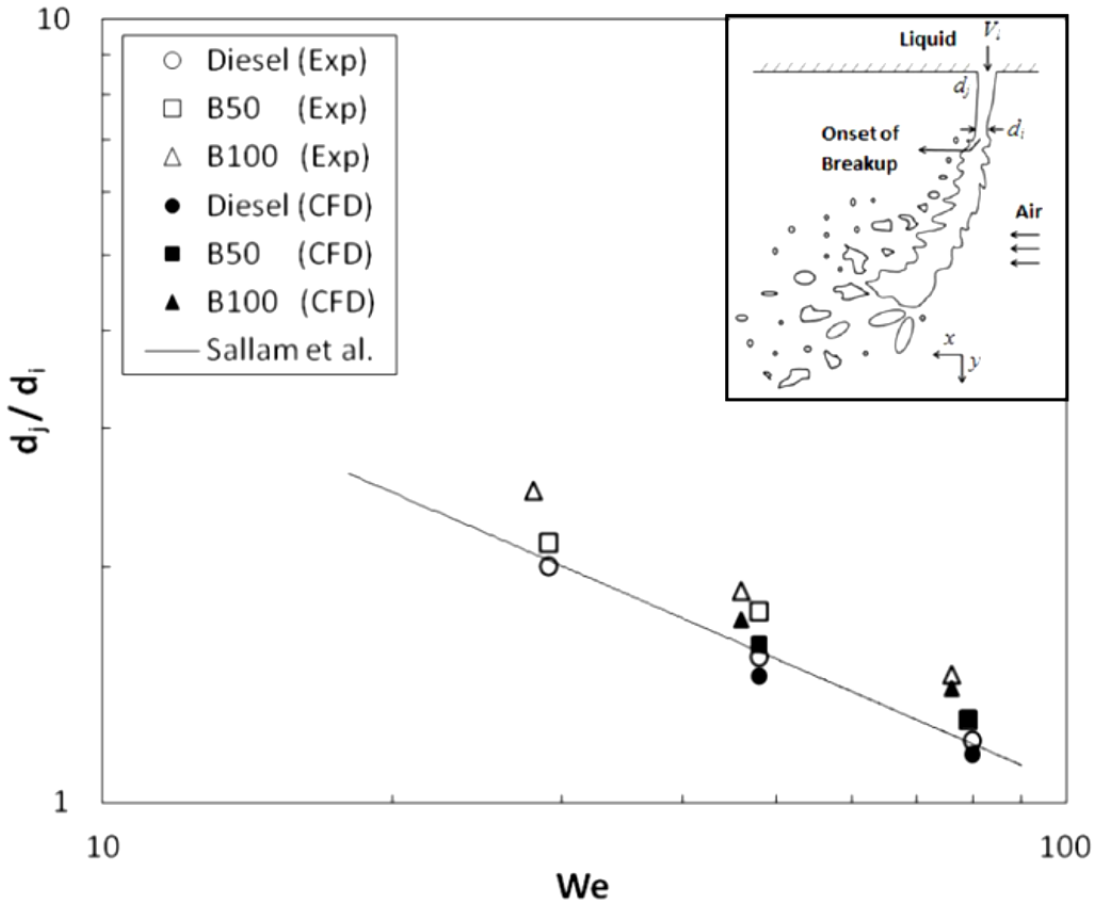


**Figure 3.12 Jet diameter ($d_j$) normalized by the side thickness of the jet at the onset of breakup ($d_i$), $q$ = 50, experimental [51] [22] vs. numerical**

Finally, Figure 3.13 shows the wavelength of instabilities on the jet surface. The wave-length is defined as the distance between two nodes of instabilities on the jet surface. The results were validated using the experimental study of the author [51] and the study of Sallam et al. [22]. The results agree well with the experimental works and shows having larger wavelengths for biodiesel and its blends comparing to diesel. Higher wavelengths can be a result of higher viscosity of biodiesel as it clearly damps the waves. Moreover the instability wave-lengths are used as a breakup regime classification parameter among different researchers [22]. It should be noticed that the Weber numbers of this study represents the multimode regime of primary breakup and in this regime both

the bag shape structures and ligaments exist; however the higher wavelength instabilities once again confirms more bag shape structures in biodiesel in contrast to diesel.

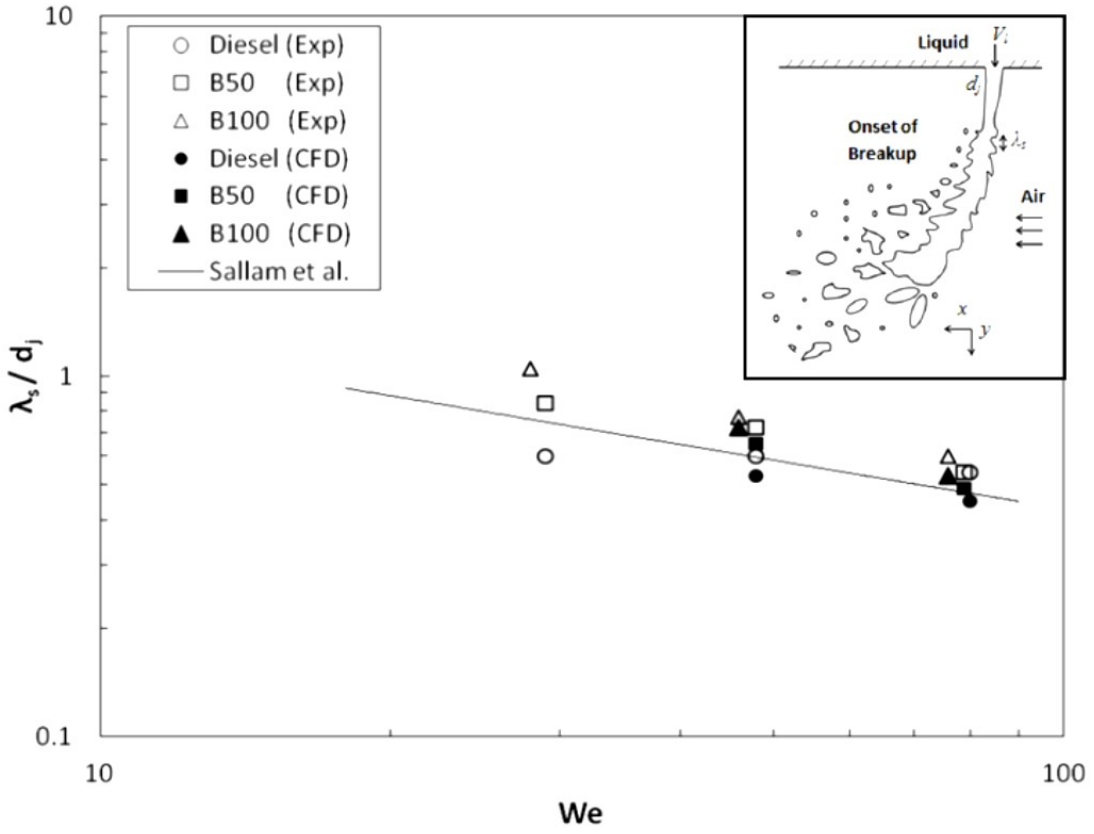


**Figure 3.13 Wavelength of jet surface instabilities ($\lambda_s$), $q$ = 50, experimental [51] [22] vs. numerical**

## 3.5 Summary and Conclusions

A comparative study of B100, B50 and diesel jet in crossflow is performed by a coupled VOF-LES simulation. In addition the numerical results are validated by the same condition experimental results of the author [51]. The results show lower penetration depth of biodiesel jet comparing to the diesel jet. One of the reasons of this behavior is having higher drag acting on the biodiesel liquid columns. Consequently, biodiesel jets deflect more towards the downstream. This is in a manner that diesel jet owing to lower

drag bends less towards downstream and consequently penetrates more inside the crossflow. Several bag shapes are observed after the primary breakup of biodiesel at large Weber numbers, i.e. atomization Weber numbers, which argues the common classification of primary breakup regimes. This is in a manner that at the same Weber numbers, diesel show atomization mode of breakup. On the other hand, biodiesel droplets at downstream of the domain have lower velocities which can be as a result of having wider wakes surrounding the biodiesel column. Furthermore, the windward trajectory of VOF-LES simulation is compared with the DPM simulation results [59]. Apparently, the results of VOF-LES seem to be in better agreement with the experimental shadowgraph results in comparison with the DPM trajectories. Ultimately, the wavelengths of jet surface instabilities are compared for biodiesel, diesel and their blends. Apparently, the high viscosity of biodiesel damps the surface waves more, which might be a cause of having the jet column more flattened, consequently higher drag and more bag shape structures during the primary breakup.

# Chapter 4

# Numerical Simulation of the Breakup of Elliptical Liquid Jet in Still Air

**Abstract**

The numerical simulation of liquid jets ejecting from a set of elliptical orifices with different aspect ratios between 1 (circular) and 3.85 is performed for several Weber numbers, ranging from 15 to 330. The axis-switching phenomenon and breakup length of the jets are characterized by means of a Volume of Fluid (VOF) method, together with a dynamic mesh refinement model. This three-dimensional simulation is compared with a recent experimental work and the results agree well. It is concluded that, by increasing Weber number ranging from 15 to 100, the breakup length of the liquid jet increases, reaches a peak, and then suddenly decreases.

## 4.1 Introduction

Liquid jet breakup plays an eminent role in many applications, such as gas turbine, internal combustion engines, agricultural liquid dispensers, oil-fired furnaces, and ink-jet printing. In fact, when a liquid jet breaks up into droplets the liquid surface increases,

leading to a higher mass and heat transfer. A number of parameters have crucial effects on the liquid jet breakup. These parameters include, but are not limited to, nozzle internal flow, jet surface waves, velocity profile, surface tension, gas velocity and direction, and turbulence at the nozzle exit. Ohnesorge [14] have categorized the four forces acting on the liquid as inertia, $\rho L^2V^2$, surface tension, $\sigma L$, viscous, $\mu LV$ and gravity, $\rho L^3g$; where $L$, $V$, $g$, $\rho$, $\sigma$, and $\mu$ represent the characteristic length of the jet (i.e. diameter, $D$), mean axial jet velocity, gravity acceleration, density, surface tension, and dynamic viscosity, respectively. The ratio of these forces can be grouped into four non-dimensional groups, including the Reynolds number, $Re=\rho LV/\mu$, the Weber number, $We = \rho LV^2/\sigma$, the Froude number, $Fr=V^2/gL$, and the Ohnesorge number, $Oh=We^{0.5}/Re$. Based on the force that leads to the breakup of a liquid jet, different regimes are defined. A classical problem in this field is the circular liquid jet breakup, which was first studied by Lord Rayleigh more than a century ago [15]. He demonstrated that at low liquid jet velocities, the effect of ambient air is negligible and the instabilities of the circular liquid jet are the main cause of breakup. This regime of liquid jet breakup is called the Rayleigh regime, after him. Dumouchel [20] has summarized various regimes of liquid jet breakup in Table 4.1, in terms of Weber number ($We$), Ohnesorge number ($Oh$) and gas to liquid density ratio ($Q=\rho_g/\rho_l$). The breakup length variation of a liquid jet with different velocities illustrates the different regimes of breakup. Figure 4.1, schematically, depicts the categorization of Dumouchel [20] for variation of the breakup length ($Z_b$) versus the liquid jet velocity ($V_l$).

**Table 4.1 Breakup regimes of liquid jet in still air, Dumouchel [20]**

| Zone | Disintegration regime | Weber number Criteria |
|---|---|---|
| A | Dripping | $We<4$ |
| B | Rayleigh | $We>4$, $QWe<0.6+2.5Oh^{0.9}$ |
| C | First wind-induced | $0.6+2.5Oh^{0.9}< QWe <6.5$ |
| D | Second wind-induced | $6.5< QWe <20.15$ |
| E | Atomization (spray) | $QWe>20.15$ |

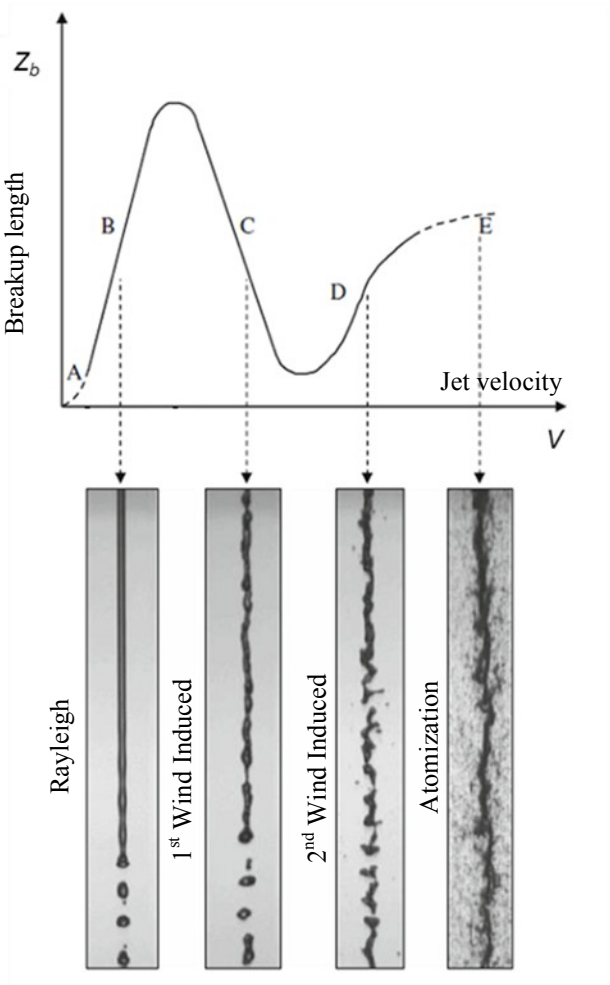


**Figure 4.1 Different breakup regimes of liquid jet in still-air, Dumouchel [20]**

Owing to the ease of manufacturing, circular nozzles have been studied extensively; however, one of the simplest ways for controlling these parameters is changing the near

field behavior by changing the geometry of spray orifices. In addition, non-circular orifices have attracted many researchers due to the fact that they may break up earlier than circular jets [21]. Husain and Hussain [26] found that in the atomization mode (see Table 4.1), the jets issued from elliptical orifices have more rapid mixing which is a remarkable profit in many combustor applications. In contrast to the interests on these non-circular orifices, there are only a few studies on this matter [21], [26], [29], [60], [61], [62], [63], since they are more complicated for theoretical analysis and practical manufacturing. The jet issued from an elliptical orifice switches its minor and major axis of the ellipse 90 degrees. Kasyap et al. [29] recently conducted a series of thorough experimental tests with water and water-glycerol in order to characterize the axis-switching phenomenon and the breakup length using elliptical injectors with different aspect ratios. Once the jet ejects out of the elliptical orifice, surface tension tends to deform the elliptical jet into a circular one in order to minimize the curved surface area, while after reaching the circular cross section, the lateral inertia does not tend to stop, therefore causing another switched elliptical cross section which is rotated 90 degrees. As illustrated in Figure 4.2, the axis switching number is an integer number defined as the number of times the jet switches its axis, while the axis switching wavelength, $\lambda_s$, is defined as the distance between every other axis switching which can vary along the jet at different times.

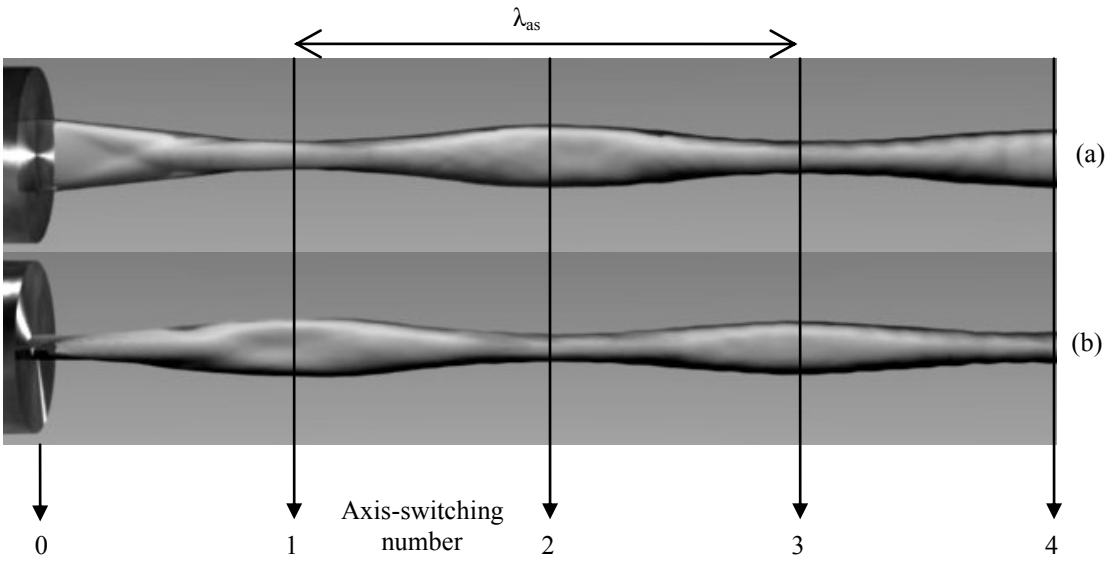


**Figure 4.2 Schematic sketches of an elliptical liquid jet discharging from an elliptical orifice, a) jet appearance in the major axis plane of the elliptical orifice, and b) jet appearance in the minor axis plane of the elliptical orifice**

**Table 4.2 Cross section dimensions of the orifices**

| Orifice index | Major axis (mm) | Minor axis (mm) | $D_{eq}$ (mm) | Aspect ratio |
|---|---|---|---|---|
| C1 | 0.50 | 0.50 | 0.5 | 1.0 |
| E1 | 0.61 | 0.41 | 0.5 | 1.5 |
| E2 | 0.86 | 0.28 | 0.5 | 3.0 |
| E3 | 1.00 | 0.25 | 0.5 | 4.0 |

From the viewpoint of instability study, Dityakin [61], Bechtel et al. [63], Bechtel [62], Caulk and Naghdi [64], and Amini and Dolatabadi [65] have developed different methods for the instability problem, including the axis switching, gravity, and viscosity effects. Dityakin [61] derived a temporal dispersion equation for axisymmetric disturbances. Neglecting the gravity effect and the gas density, he investigated the instability of an inviscid elliptic liquid jet in an inviscid gas, analytically. Bechtel et al.

[63], used a one-dimensional model with the Galerkin method in order to integrate the Navier-Stokes equation over the jet cross section. In another study, Bechtel [62] performed an analytical investigation on the effect of viscosity and gravity. He proposed a nonlinear conservative oscillator model for the axis switching phenomenon in the absence of viscosity and gravity. This one degree of freedom oscillator model is converted to non-conservative form in the case of Newtonian fluid. Caulk and Naghdi [64], [66] included the surface tension in their one-dimensional Cosserat equations to obtain the free surface location of a viscous liquid jet with a finite ellipticity. In their study, the motion of a fluid jet is replaced by the motion of a directed curve based on the Cosserat theory. It should be mentioned that Caulk and Naghdi [66] used their model to investigate the instability of a special case of circular jet only, and did not study the issue of elliptic jet instability. In a recent research, Amini and Dolatabadi [21], [60], [65] obtained a linear one dimensional solution of the temporal and spatial capillary instability equations for an elliptic viscous liquid jet. They captured the growth rate of disturbances for different modes under various conditions. They also suggested an equation for the jet profile, the axis-switching phenomenon, and break-up for various conditions. The equations are approximated for small and large ellipticities. They found that in the capillary regimes, the effect of ellipticity increases the growth rate, while at higher Weber numbers, as the aerodynamic forces prevail, the higher the ellipticity becomes, the lower the growth rate. Finally, Amini and Dolatabadi [21], [60], [65] performed a set of experiments for validation of the linear results. The experimental data are in agreement with the theoretical predictions; however, at high ellipticities, the nonlinear effects are strong while the experimental and numerical results deviate.

Apparently, due to several simplifying assumptions, the validity of theoretical results may be limited to some conditions; therefore, a numerical simulation seems to improve one's understanding of the axis-switching phenomenon, dominant instability modes, and breakup of elliptic liquid jets. In this vein, Brown and Boris [67] studied the elliptic jets numerically, using the Direct Numerical Simulation (DNS) coupled with Flux Corrected Transport (FCT) technique. Their study is dedicated to finding the reason of rapid mixing of elliptic jets compared to circular jets. It resulted in recognizing the generation and evolution of vortical structures along the boundary of the jet as a result of the Kelvin-Helmholtz instability. These instabilities are identified as a reason for rapid mixing of elliptical jets. Miller et al. [68] performed a set of numerical studies in order to find the effect of different shape orifices, i.e. circular, elliptical and rectangular, on the fluid structure and mixing of free jets. They simulated several jets with initial cross-section aspect ratios 1 and 2. Miller et al. [68] used a three dimensional (3D) domain with 4×4 diameter size and 9 diameter length. They captured the axis switching phenomenon, entrainment and mixing characteristics. The results show faster mixing for elliptical jets compared to circular ones. In this numerical study, deformation, surface waves, and the disintegration of a set of liquid jets issued from elliptical orifices are compared with those of a circular jet having the same cross-sectional area. In addition, the phenomenon of axis-switching, which is a specific behavior of the jets emanating from elliptical nozzles, has been investigated in a domain as large as 10×10×100 jet diameters. In this study, the gaseous environment is still air with a gas Weber number of less than 0.4 ($We_g = \rho_g D V_g^2/\sigma$) and the liquid jets have a liquid Weber number ($We = \rho_l D V_l^2/\sigma$) range of 30 to 225 for water. It should be mentioned that ρg and ρl are the gas and liquid density,

respectively. Considering the previous experimental studies by Pan and Suga [69] and Reitz [70] the effect of gas environment on the liquid jet disintegration and breakup are negligible for $We_g < 0.4$. The numerical modeling is performed using the Volume of Fluid (VOF) method coupled with the Large Eddy Simulation (LES) turbulence model of flow provided by the OpenFOAM CFD code [53]. The VOF model, in turn, uses the MULES (Multidimensional Universal Limiter with Explicit Solution) scheme. In addition, for accurate tracking of the liquid interface, its surface waves, and breakup phenomenon, the interface has been captured by a dynamic adaptive mesh refinement method. To get a better comparison of the near field behavior, the numerical results are post-processed with ParaView software [57] and the liquid interface meshes are rendered by Blender open-source software [58].

The numerical studies were then validated using the experimental works in the literature. The results clearly show the surface waves and ruffles on the jet, the penetration depth and detached ligaments at the aforementioned Weber numbers. Furthermore, the interesting axis-switching behavior of the elliptical jets has been quantified by the axis-switching number and is compared with the experimental results of the literature. The numerical results show good agreement with the experimental cases.

## 4.2 Geometry and Boundary Condition

A set of orifices, including the circular and several elliptical orifices with different aspect ratios are considered for the simulations (Table 4.2). It should be mentioned that in this study, the aspect ratio is assumed to be the ratio of the major to minor axis of the orifice. The orifices are designed to have the same area, but with different geometries. In

this regard, the equivalent diameter of the orifices is 0.5 mm and the aspect ratios of the study of Kasyap et al. [29] are used for having a one-to-one comparison of the numerical results of this paper with their experimental set of results.

Figure 4.3 shows a schematic of simulation geometry. A rectangular cube of 5×5×50mm is modeled, consisting of the injector on one side and air as the inside material. Hence, the ambient of the jet has a size of 10×10×100 diameters of the jet on each side, respectively, and is flowing across the long side of the rectangular cube. Having the 100 diameters for the jet to break up facilitates the measurement of axis-switching characteristics and breakup length. The geometry is meshed by a Cartesian grid of 0.15 mm increments on the z direction. On the x-y plane, the same mesh size is used in a mapped mesh form in order for the mesh to form the shape of the orifice cross section.

Boundary conditions of this geometry are fixed pressure on the side walls and outlet, and fixed velocity on the injector and the wall which includes the injector. It should be mentioned that velocity on the wall is fixed to zero, according to the no-slip boundary condition. The velocity of the water ejecting from the injector varies according to Table 4.3, which covers the Rayleigh mode of breakup.

**Table 4.3 Liquid injection Weber and Reynolds number**

| Injection velocity (m/s) | *We* | *Re* |
|---|---|---|
| 1.5 | 15 | 837 |
| 2.1 | 30 | 1172 |
| 4.0 | 110 | 2245 |
| 6.9 | 330 | 3884 |

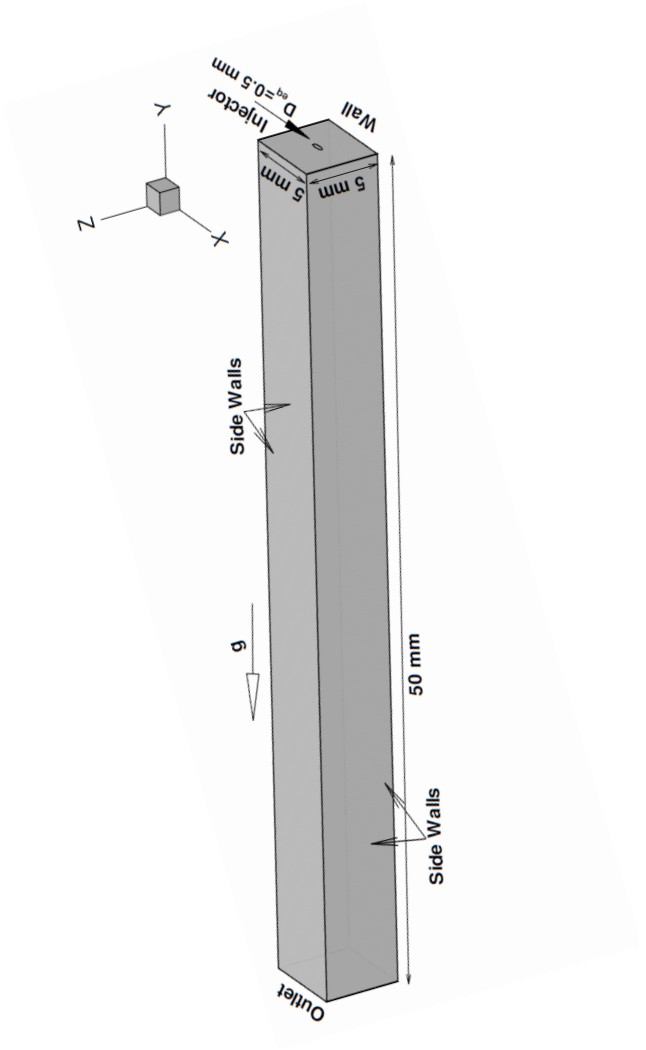


**Figure 4.3 Schematic of the simulated geometry**

The liquid-to-gas volume fraction ($\alpha$) on the injector inlet cells is kept one as boundary condition. Also the value of volume fraction ($\alpha$) is zero in all other cells at time $t$=0. The value of turbulent kinetic energy, $k$, is implemented by using Equation 4.1 for each boundary condition, based on a turbulence intensity of $I$=15% for the liquid inlet and $I$=1% for the side walls, which may pass a little amount of air due to the advancing liquid jet inside the geometry. It should be mentioned that turbulence intensity, $I$, is

defined as the ratio of root mean square of velocity fluctuation to the local mean velocity. As noted in the introduction, this simulation is validated by the experimental data of Kasyap et al. [29]. Hence, the value of turbulence intensity, $I$, at the liquid entrance boundary ($I$=15%) is estimated based on the nozzles which have not reached a fully-developed flow for the Reynolds number of this study, which lies on the laminar regime. The pressure at the side walls and outlet is considered to be fixed atmospheric pressure in contrast to Neumann boundary condition (zero gradient) at the liquid inlet.

$$k = \frac{3}{2}(V_l I)^2$$ **Equation 4.1**

## 4.3 Methodology

The computational fluid dynamics simulation is performed using OpenFOAM code [53]. The solver is an incompressible, three-dimensional, Volume of Fluid (VOF) solver for two immiscible fluids. Air and water with a surface tension of 0.07 N/m are considered Newtonian fluid phase one and two, respectively. Consequently, each cell at any instance has a value of α equal to the volume fraction of water to air as shown in Figure 4.4. For example, at the initial time, the value of α for the whole domain, except the cells on the injector face, is zero.

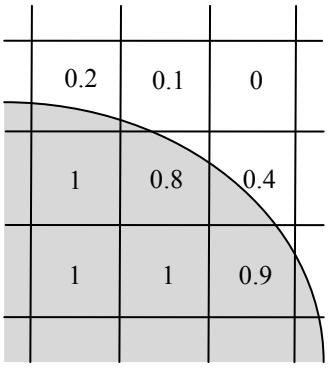


**Figure 4.4 Schematic of VOF method on computational cells**

The governing equation for this modeling is the incompressible Navier Stokes equations, including continuity and momentum equations with $\vec{v}$, $\rho$, $p$, $\mu$, and $g$ as velocity, density, pressure, viscosity, and gravity, respectively. The gravity applied in the Navier-Stokes equations is 9.8 m/s$^2$.

$$\nabla.\vec{v} = 0 \quad \textbf{Equation 4.2}$$

$$\frac{\partial}{\partial t}(\rho\vec{v}) + \nabla.(\rho\vec{v}\vec{v}) = -\nabla p + \nabla.[\mu(\nabla\vec{v} + \nabla\vec{v}^T)] + \rho\vec{g} + \vec{F} \quad \textbf{Equation 4.3}$$

$$\rho = \rho_l + \rho_g(1-\alpha) \quad \textbf{Equation 4.4}$$

$$\mu = \mu_l + \mu_g(1-\alpha) \quad \textbf{Equation 4.5}$$

$$\vec{F} = \sigma\kappa\nabla\alpha \quad \textbf{Equation 4.6}$$

$$\kappa = -\nabla.\left(\frac{\nabla\alpha}{|\nabla\alpha|}\right) \quad \textbf{Equation 4.7}$$

It should be mentioned that $\vec{F}$ is the surface tension force on the interfacial cells which is a function of surface tension $\sigma$, surface curvature $\kappa$, and the gradient of volume fraction $\alpha$.

In terms of volume fraction conservation throughout the domain, a modification has been made in the VOF method by introducing an additional convective term in the volume fraction conservation equation [55].

$$\frac{\partial}{\partial t}(\alpha) + \nabla.(\alpha\vec{v}) + \nabla.[\overrightarrow{v_r}\alpha(1-\alpha)] = 0 \quad \textbf{Equation 4.8}$$

The mentioned convective term is called artificial compression and contains the compression velocity which is computed in a suitable way in order to avoid smearing of the phase interface [56]. In this regard, since the term $\alpha(1-\alpha)$ has non-zero value in the

vicinity of the interface and zero value on the other cells, it does not affect the overall solution while it facilitates capturing an interface, which is a step function of $\alpha$ between liquid ($\alpha = 1$) to gas ($\alpha = 0$). The $\vec{v}_r$ at the vicinity of the interface is a velocity field to compress the interface and is found by Rusche's model [55].

$$\overrightarrow{v_{r,f}} = n_f min\left[C_\alpha \frac{|\varphi|}{|S_f|}, max\left(\frac{|\varphi|}{|S_f|}\right)\right] \quad \textbf{Equation 4.9}$$

Whereas $\varphi$, $S_f$, $C_\alpha$, and $n_f$ are the face volume flux, cell face area vector, compression coefficient (i.e. 1.5 as per Rusche's model), and face unit normal flux, respectively. The face unit normal is also defined by the following equation. Technically, a small value constant, $\delta_n$, is considered in this formula in order to avoid division by zero in the cells where $\left|(\nabla\alpha)_f\right| \to 0$. For example, in this calculation, $\delta_n$ is considered $10^{-5}$.

$$n_f = \frac{(\nabla\alpha)_f}{\left|(\nabla\alpha)_f\right| + \delta_n} \quad \textbf{Equation 4.10}$$

The turbulence model used in this study is the Large Eddy Simulation (LES) model using one equation for finding Sub-Grid Scale (SGS) kinetic energy and smooth filtering delta coefficient of 1 with a maximum delta ratio of 1.1. The SGS stress tensor can be approximated by means of the eddy viscosity definition and SGS kinematic viscosity. These two parameters, in turn, have a transport equation introduced by Yoshizawa and Horiuti [54].

$$\tau_{sgs} = \overline{v}\overline{v} - \bar{v}\bar{v} \quad \textbf{Equation 4.11}$$

$$\tau_{sgs} - \frac{2}{3}k_{sgs}I = -\frac{\mu_{sgs}}{\rho}[\nabla\bar{v} + (\nabla\bar{v})^T] \quad \textbf{Equation 4.12}$$

$$\frac{\partial k_{sgs}}{\partial t} + \nabla.\left(k_{sgs}\bar{v}\right) = \nabla.\left[(\vartheta + \vartheta_{sgs})\nabla k_{sgs}\right] - \epsilon - \vartheta_{sgs}\bar{S}^2 \quad \textbf{Equation 4.13}$$

Whereas in these equations, $\varepsilon$, $v_{sgs}$ and $S$ are found by the following relations:

$$\epsilon = \Delta C_\epsilon (k_{sgs})^{3/2}, \qquad C_\epsilon = 1.05 \qquad \textbf{Equation 4.14}$$

$$\vartheta_{sgs} = \Delta C_k (k_{sgs})^{1/2}, \qquad C_k = 0.07 \qquad \textbf{Equation 4.15}$$

$$\bar{S} = \frac{1}{2}(\nabla \bar{v} + (\nabla \bar{v})^T) \qquad \textbf{Equation 4.16}$$

A coupled set of Navier-Stokes equations is solved implicitly by a PISO (Pressure Implicit with Splitting of Operators) method at each time step. The default time step of $1\times10^{-5}$ seconds is taken into account with the possibility of adjustments with Courant number. In this regard, the maximum Courant number, which restricts the time step adjustment, is 0.5 and the upper limit of time step is $1\times10^{-5}$ seconds. Subsequently, the chosen time step is less than $1\times10^{-5}$ seconds, which facilitates the simulation of even the smallest perturbations on the jet surface and its process of breakup. In terms of the total time of the flow, the results serve the simulation of jet evolution through the domain from time zero to 0.1 seconds. During the jet evolution, the solution is saved after each $5\times10^{-4}$ seconds of the flow.

As mentioned in previous parts, a dynamic mesh refinement method is used to solve the liquid flow on a fine mesh in order to capture the perturbations on the liquid and small droplets separated from the bulk liquid. It is not necessary to solve the air on a fine mesh, since the air is quiescent and has less perturbation compared to the liquid part. In this way, the whole mesh is a coarse one in order to solve the gaseous part, while after each iteration and the liquid advancement in the domain, the refinement is solely performed on the cells which contain liquid. The dynamic mesh refinement process is controlled by the value of alpha. Consequently, the cells, which have $0.001 \leq \alpha \leq 1$, are refined one level in the x, y, and z direction. At the next iteration, again the cells which contain liquid are refined. In this manner, the liquid-containing cells become finer at each

iteration; however, in order to restrict the numerical problem in a timely and cost-effective manner, there is a maximum limit of three refinement levels for each cell and a limiter of 10,000,000 cells for the whole domain mesh after the final refinement. Therefore, as can be seen in Figure 4.5, the liquid-containing cells are refined even though they are on the liquid jet's surface with $0.001 \leq \alpha < 1$ or inside of it, with $\alpha = 1$. It should be mentioned that for comparison, primarily, a simulation was performed with a mesh refinement just on the interface containing cells with $0.001 \leq \alpha < 1$. In that comparative simulation, the jet surface cells were refined; however, the liquid jet interior cells with $\alpha = 1$ were not. Although in both cases, axis-switching phenomenon was captured; its wavelength, jet's surface ruffles, and breakup point are considerably different. Later on, where the validation with the experiments is given, it is shown that the simulation results having the dynamic mesh refinement on $0.001 \leq \alpha \leq 1$ lead in sound agreement with the experiments. Indeed, this comparison depicts the significant role of the core of the liquid jets on its instability and breakup, which is proved also by Amini [21].

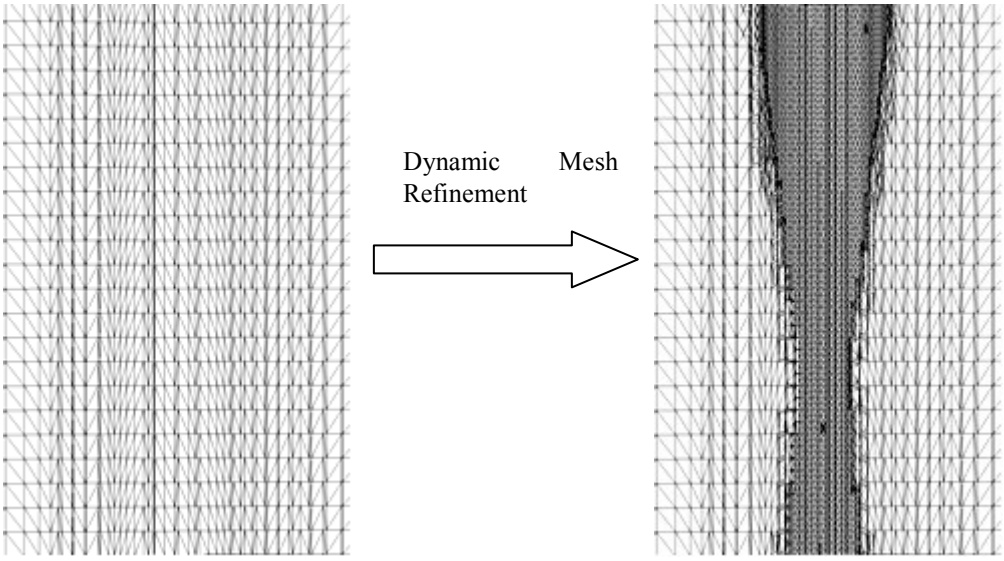


**Figure 4.5 Dynamic mesh refinement cut off (right), initial mesh cut off (left)**

Finally, in order to get a better comparison of the near-field behavior, the numerical results are post-processed with ParaView software [57] and the liquid interface meshes are rendered by Blender open-source software [58]. The numerical simulation was then validated using the experimental work of Kasyap et al. [29] on the axis-switching characterization and breakup length.

## 4.4 Results

The numerical results clearly illustrate the axis-switching phenomenon which agrees prominently well with the experimental data. Figure 4.6 shows an image of the elliptical jet ejected from the elliptical orifice E2. It is remarkable to notice the agreement between the numerical and experimental results in terms of axis-switching wavelength variation, max diameter change, breakup length and separated droplet shape in this figure. Since the aspect ratio of E2 is high (3) compared to the circular orifice, the axis switching is clearly identified in the images. This means that the surface tension attempts to pull the elliptical cross section to a minimum surface energy cross section, i.e. circular, while the inertia

tends to continue its way after reaching the circular cross section. Depending on the jet velocity, it is expected to observe some perturbations because of turbulence on the surface of the jet, which is shown in the experimental results. The numerical results show the same behavior in this regime of the flow, meaning that the turbulence model predicts the phenomenon well in terms of turbulent kinetic energy and its dissipation. The jet, after oscillating between the elliptical and circular shape, reaches a point that tends to break up and this fact is one of the challenging processes in numerical simulations. If there is no or a low number of mesh refinements in the simulation, usually the prediction of breakup length can be misleading. This is due to having coarse meshes in the neck of the jet where it prepares to break up, while having enough levels of mesh refinement leads to the comparable results. Owing to this fact, a mesh dependency study is performed to find the optimum number of mesh refinement levels. The study shows that if the number of mesh refinement levels is less than 3, the results are not in agreement with the experimental images in terms of the breakup length, surface ruffling of the jet, and axis-switching number of oscillations.

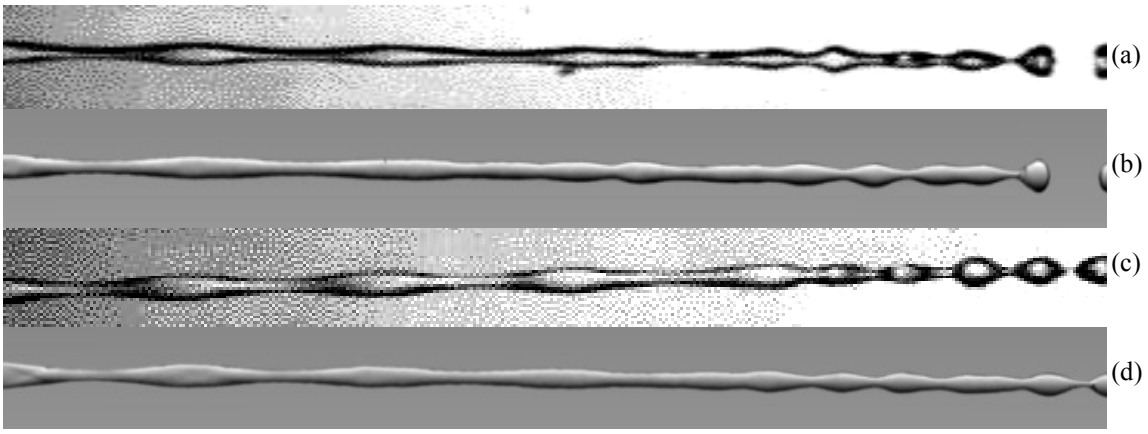


**Figure 4.6 Cut off images of elliptical water jets ejected from orifice E2 (3) at $We^{0.5}$=10.5, a, c) experimental, courtesy of G. Amini, and b, d) numerical simulation iso-surfaces ($\alpha$=0.5), at different times**

In terms of characterizations of the elliptical jet, some parameters are investigated, including the axis- switching wavelength, the axis-switching number, and the breakup length. It should be mentioned that the axis-switching wavelength is the distance between two successive major axis points according to Figure 4.2. In addition, the axis-switching number is considered to be zero at the ejection point and the advancement of the jet from the elliptical to the circular cross section, or vice versa, is counted as an addition to the axis-switching number (see Figure 4.2).

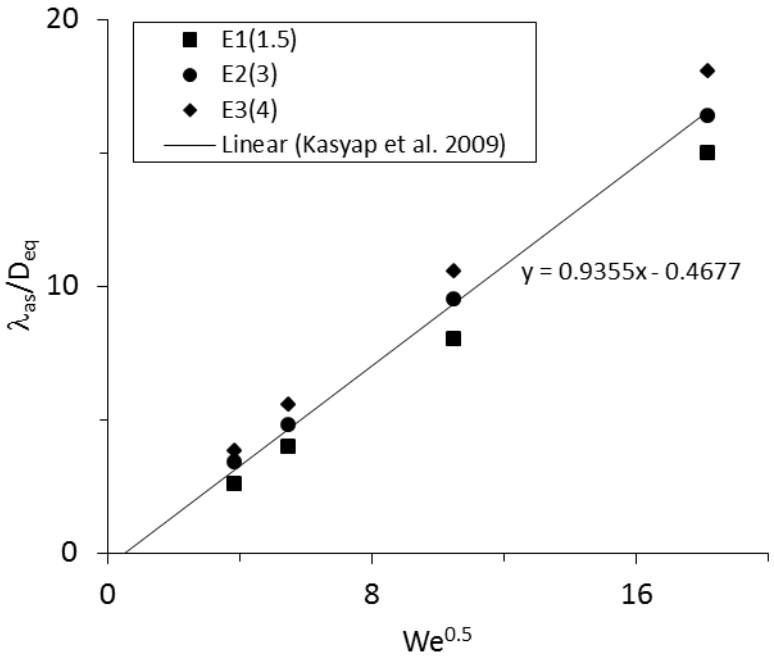


**Figure 4.7 Nondimensionalized axis-switching wavelength vs. the Weber number square root**

The equivalent diameter is defined by Equation 4.17. Apparently, the equivalent diameter of the elliptical orifice is the diameter of the circular jet having the same cross-sectional area *A*. Figure 4.7 shows the variation of axis-switching wavelength which is

non-dimensionalized by the equivalent diameter. According to Rayleigh [15], Geer and Strikawerda [71], and Kasyap et al. [29] and their experimental results, the axis-switching wavelength in a low Weber number, low Ohnesorge number regime, shows a linear variation versus the Weber number square root. This behavior is independent of the orifice geometry and is apparent in the numerical results of the present work as well.

$$D_{eq} = \sqrt{\frac{4A}{\pi}}$$ **Equation 4.17**

The axis-switching wavelength variation along the jet axial direction is captured in Figure 4.8 for different orifices. The data identified by filled symbols are the simulation results and the data identified by open symbols represent the experimental results of Kasyap et al. [29]. As can be seen, the axis-switching wavelength is low with an increasing trend towards the axial direction. This behavior can be a result of either gravity or the advancing contact angle of water at the injection point which is related to the orifice and liquid velocity. In fact, any small roughness change or any imperfection in the orifice exit can affect the axis switching wavelength at the near field; however these effects will be damped along the jet advancement [29], [72]. It should be mentioned that in this work the advancing contact angle of water at the injection point is computed by the code with a limit of 90º in order to simulate a stainless steel machined orifice. As a result, the numerical outcome and the experimental data [29] agree well.

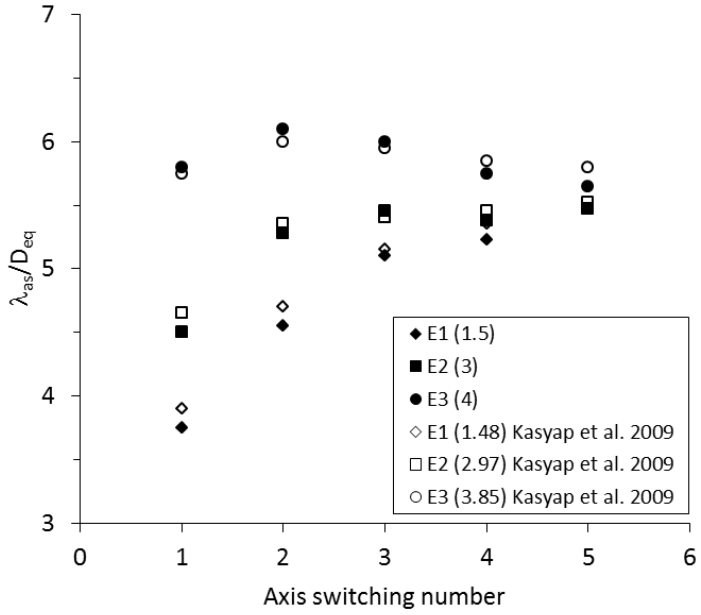


**Figure 4.8 Effect of orifice geometry on non-dimensionalized axis-switching wavelength vs. axis-switching number (defined according to Figure 4.2) for $We^{0.5}$=6 (experimental) and $We^{0.5}$=5.45 (numerical)**

In addition, the effect of different Weber numbers on the axis-switching wavelength is depicted in Figure 4.9. Based on the numerical and experimental results, by increasing the Weber number, a shift of the axis-switching wavelength behavior is expected; however, the wavelength behavior remains almost identical. The difference between the numerical and the experimental results is owing to the fact that the simulated tests are at a relatively lower Weber number comparing to the experimental results. In this regard, a one-to-one matched data on the axis switching was not available to compare.

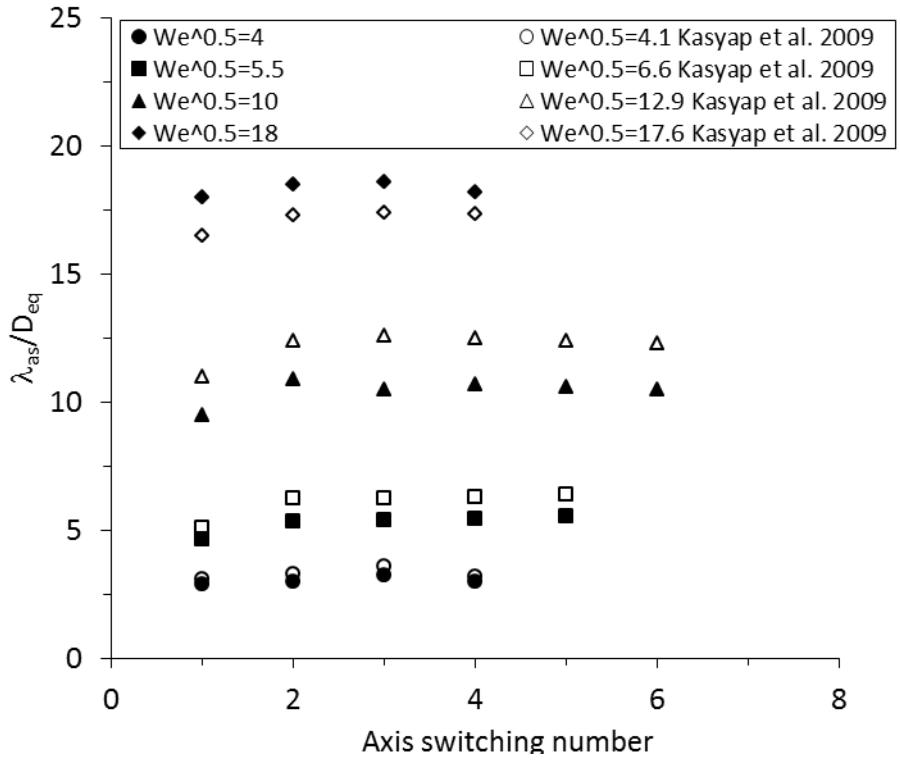


**Figure 4.9 Effect of Weber number ($We^{0.5}$) on non-dimensionalized axis-switching wavelength vs. axis-switching number (defined according to Figure 4.2) for orifice E2 (3)**

Another aspect in the elliptical liquid jet characterization is the breakup length which is presented in Figure 4.10. The breakup length in the regime of study (Rayleigh regime) is increased by increasing the velocity of the jet, and then it reaches a peak and decreases suddenly. These simulation results conform to the experimental results and once again show that the chosen dynamic mesh refinement method had predicted the primary breakup of the jet well. It should be mentioned that at low Weber numbers, before reaching the maxima (at a Weber number called $We_{crit}$) in the curves of Figure 4.10, no axis switching is observed in the simulation conforming to the experimental results [29]. In other words at Weber numbers smaller than $We_{crit}$, the liquid jet has a capillary breakup behavior and surface tension plays the most important role in its breakup. At a

Weber number close to $We_{crit}$ axis switching appears in the simulation and experimental results [29]. Thereafter, as the Weber number increases, the breakup length reduces and reaches to its minimum value. At this stage ruffles form on the jet surface. In this regime, weaving of the jet interface by means of ruffles and axis switching results in a significant decrease of the jet breakup length [16]. Therefore higher aspect ratio of elliptic jets leads in larger perturbations that reduce the liquid breakup lengths. The points at the right of the minima in Figure 4.10 represent the other regime of breakup, in which the momentum plays an important role and dominates the turbulence effects. In this regime, an increase in Weber number increases the momentum and consequently the breakup length [20].

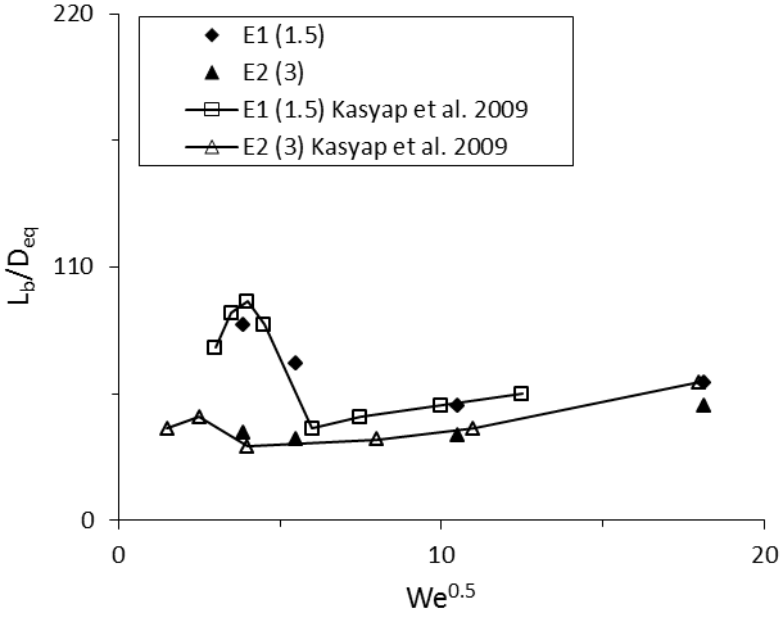


**Figure 4.10 Numerical and experimental [21] breakup length for orifice E2 (3)**

A comparison has been made in order to assess the choice of number of grid-refinement levels and turbulence method, i.e. Large Eddy Simulation (LES) compared with the k-ε turbulence model. In order to study the grid refinement sensitivity on the

solution, the jet breakup length for nozzle E2 with an aspect ratio of 3 (E2(3)) is obtained for different number of refinement levels. As can be seen in Figure 4.11, using two levels of refinement, the results deviate rather significantly from the experiment. In other words, two level refinement results in a monotonically increasing trend compared to the experimental results that has a minimum on low Weber numbers. Furthermore, the results for the case of two refinement levels have a maximum of more than 30% error comparing to the experimental ones. By implementing three levels of mesh refinement the numerical results considerably improves such a way that the difference between three and four levels of mesh refinement is less than 5%. Considering more than 8 times memory usage and slowing down the simulation 10 times for the case of four refinement levels, led us to choose three refinement levels for the present simulations.

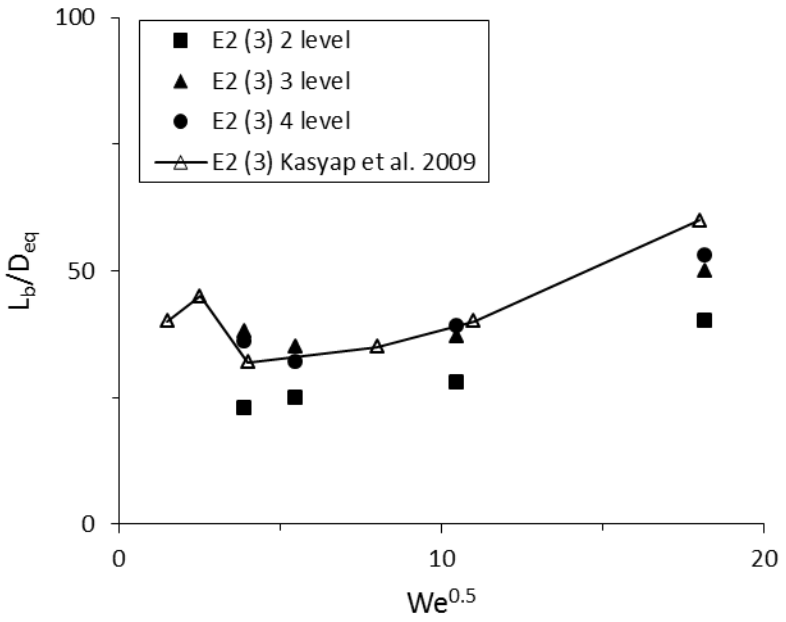


**Figure 4.11 Breakup length sensitivity to number of mesh refinement levels**

Finally, in order to assess the choice of turbulence model on the simulation results, nozzle E2(3) and E3(4) have been chosen for this purpose and their normalized axis-switching wavelength are validated by using the Kasyap et al. [16] experiments. It is depicted in Figure 4.12 that the experimental results and the LES based simulation results are in good agreement in terms of increasing the wavelength after the nozzle exit, reaching a maximum, and then plateauing along the rest of the jet. In contrast, the wavelength obtained by the k- ε turbulence model is monotonically increasing alongside the jet path. The increasing behavior of the wavelength right after the nozzle exit is due to gravitational acceleration and orifice exit perturbations [16], while these are damped by the effect of viscosity and surface tension along the rest of the jet. This is in a manner that, as known, the *k-ε* turbulence model does not simulate very well the damping of the perturbations. Furthermore a laminar case is solved to find out the effect of turbulence modeling on the simulations results. It can be seen in Figure 4.12 that axis switching wavelength does not agree with the experimental results neither in value nor in its trend. In summary, the laminar simulation significantly underestimates the axis switching wavelength. Apparently, in the laminar regime, the surface waves and internal flow have less perturbations and the only reason of increasing the wavelength along the jet may be the effect of gravitational acceleration.

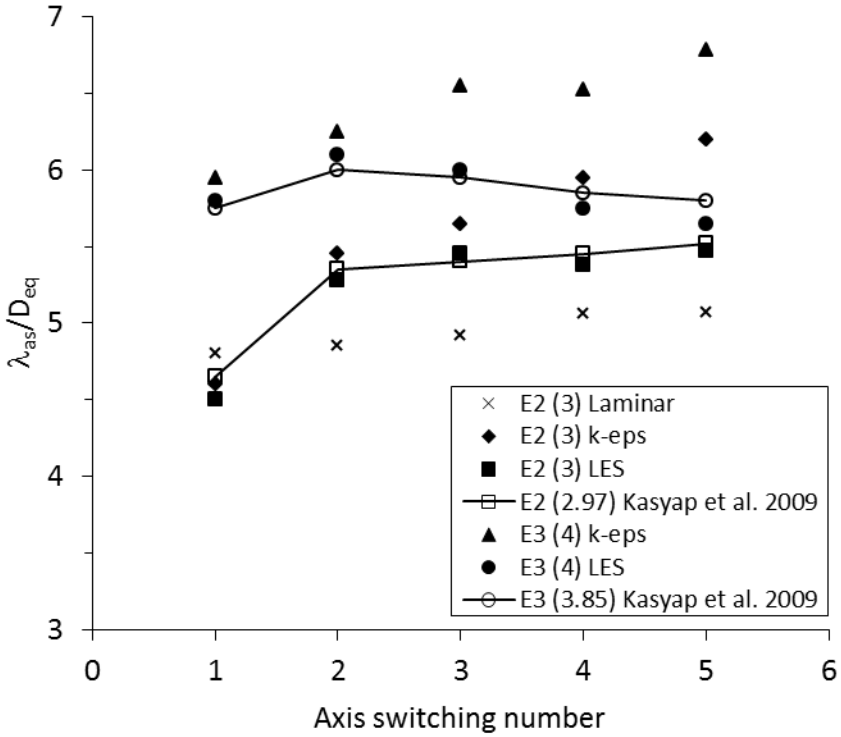


**Figure 4.12 Comparison of LES and *k-ε* turbulence model on the simulation results, *We*=110**

## 4.5 Conclusion

A series of simulations is conducted with the aim of modeling the primary jet breakup in still air in the Rayleigh regime. Furthermore, the characterization of the axis-switching phenomenon is performed, using the computational tools. The elliptical jet shows an axis-switching phenomenon by changing the major and minor axis in a 90 degree shift. This behavior was well characterized by the numerical simulation and it is in a good agreement with the experimental results in terms of the wavelength and its variation along the axis. In addition, the breakup length of the elliptical jet which is modeled is completely in agreement with the experimental data. It is concluded that the choice of VOF and LES model, together with the dynamic mesh refinement based on the volume fraction, leads to comparable numerical results. Furthermore, by using the

dynamic refinement mesh instead of a fine initial mesh, a remarkable progress is made towards the time performance and memory efficiency of the simulation. As an issue with the numerical simulation, even with a high level of mesh refinement, it does not show any satellite droplets (the small droplets between two large droplets or ligaments) after the first break up of the jet, while in some Weber numbers in the experimental images, satellite droplets are demonstrated. This study serves a fundamental numerical simulation of the elliptical jets in still air. Satellite droplet capturing and finding the natural frequency of elliptical jets are proposed as a future work.

# Chapter 5

# Simulation of the Breakup of Elliptical Liquid Jet in Gaseous Crossflow


## Abstract

In this study, a set of elliptical liquid jets in gaseous crossflow is investigated, numerically and experimentally. The Volume of Fluid (VOF) method coupled with the Large Eddy Simulation (LES) turbulence model have been used in order to simulate the near field primary breakup of liquid. On the other hand, the shadowgraph technique has been used to investigate the liquid breakup phenomenon from the liquid jet to small droplets downstream. The shadowgraph images visualize different characteristics of this flow, such as trajectory, surface waves and liquid column slope. Several elliptical geometries with different aspect ratios between 0.25 and 4, including the cylindrical shape, were considered as the liquid jet nozzle exit. The simulations were performed with relative gas–liquid Weber numbers (11, 18 and 30) which cover the bag and multimode primary breakup regimes in crossflow. In addition, the liquid-to-gas momentum ratio is kept at 50 and 100. The results show remarkable changes in liquid shapes before

disintegration for different aspect ratios. Also the penetration depth, droplet size distribution and spray spreading angle have been affected by the change of disintegration model.

## 5.1 Introduction

Atomizing a bulk liquid jet to fine droplets, using gaseous crossflow, has a vast variety of applications, such as coating, spray drying, gas turbine combustion chamber, ramjets, scramjets and the agriculture industry [25], [32], [33], [34], [35], [36], [37], [38]. Near field behavior of the transverse liquid jets in crossflow (i.e. deformation, surface waves, and primary breakup) apparently has crucial effects on spray characteristics such as penetration depth, spray spread angle, breakup phenomena, and final droplet size distribution. One of the simplest ways for controlling these parameters is changing the near field behavior by changing the geometry of spray orifices.

The effect of nozzle geometry on the primary and secondary breakup of liquid jets in still air has been studied in recent decades. Non-circular orifices have attracted many researchers due to the fact that their jets may break up earlier than circular jets. Elliptical orifices have rapidly found a place among other non-circular orifices. Elliptical liquid jets emanating from these types of orifices always tend to configurations with minimum surface energy. Consequently, several inherent instabilities such as axis-switching lead to breakup of these jets with less energy. In addition, the surface area of an elliptical jet is larger than the equivalent diameter circular jet. These effects result in faster disintegration of liquid jets. Husain and Hussain [26] found that in the atomization mode, the jets issued from elliptical jets show more rapid mixing which is a remarkable advantage in many combustor applications. Liquid jets emanating from elliptical orifices

in air crossflow also have been studied by a few researchers including but not limited to Song et al. [27]. They found that flames issuing from elliptical nozzles with major axis perpendicular to the crossflow have wider stability limits compared to flames issuing from a circular nozzle or elliptical nozzles with minor axis normal to the crossflow.

From the numerical point of view, working with a circular nozzle, Madabhushi [42] performed a series of Lagrangian particle tracking simulations of droplets in a gaseous crossflow. He used a Reynolds Average Navier-Stokes model coupled with a $k$-$\varepsilon$ turbulence model for the gaseous phase and validated his results with an experimental work. Although a general agreement with the experiment was observed, due to the absence of wakes and vortices which are mostly damped by the $k$-$\varepsilon$ model, some of the droplets' velocity and size were different from the experiment. Subsequently, Ng et al. [43] performed a Volume of Fluid numerical modeling of LJICF. A correlation between the wavelength, jet diameter and Weber number was obtained based on their study. Later on, Hermann [44] developed a Refined Level Set Grid (RLSG) method, which is coupled with the Large Eddy Simulation (LES) turbulence model for capturing the liquid interface of the jet in crossflow. He also has added on a Lagrangian two-way coupled simulation for small and spherical droplets downstream of the jet's primary breakup. Marzbali [24] simulated the elliptical jets in crossflow, in addition to his theoretical work. He used the VOF method in order to find the liquid interface. Additionally, he applied an analytical approach to balance the forces on the liquid jet column and finally correlated the trajectory of the elliptical jet by using a logarithmic formula. Finally, he demonstrated a relatively good agreement between his numerical and experimental results. It should be mentioned that the work of Marzbali [24] has been performed without any dynamic mesh

refinement. Lack of mesh refinement, especially in the vicinity of the interface, results in capturing interfaces that might be erratic.

In the numerical study, deformation, disintegration, droplet size distribution and spread angle of a set of liquid jets issued from elliptical orifices are compared with those of a circular jet having the same cross-sectional area. The Weber number range of this study is 11–30, which represents the bag and multimode regimes of liquid breakup in gaseous crossflow. Furthermore, shadowgraph images are used to visualize the characteristics of these jets and finally can be generalized to different liquids such as biodiesel and diesel.

## 5.2 Experimental Setup

Except for the new elliptical nozzles, the experimental setup used in this work is similar to the previous work of the author [51]. It consists of an open loop subsonic wind tunnel with a test section of 100×100×750 mm and free stream velocity up to 58 m/s. The flow field in the test section has been characterized using PIV to find the velocity profile and turbulence kinetic energy intensity. The injector is a plain orifice with length-to-diameter ratio of 10. Different orifice shapes are machined on aluminum plates, using the electro discharge method. Equivalent diameters of different nozzles are 0.5 mm. The injector is mounted perpendicular to the top of the test section at an axial position of 200 mm from its inlet plane. The center of the 0.5 mm diameter lies on the symmetry plane of the test section.

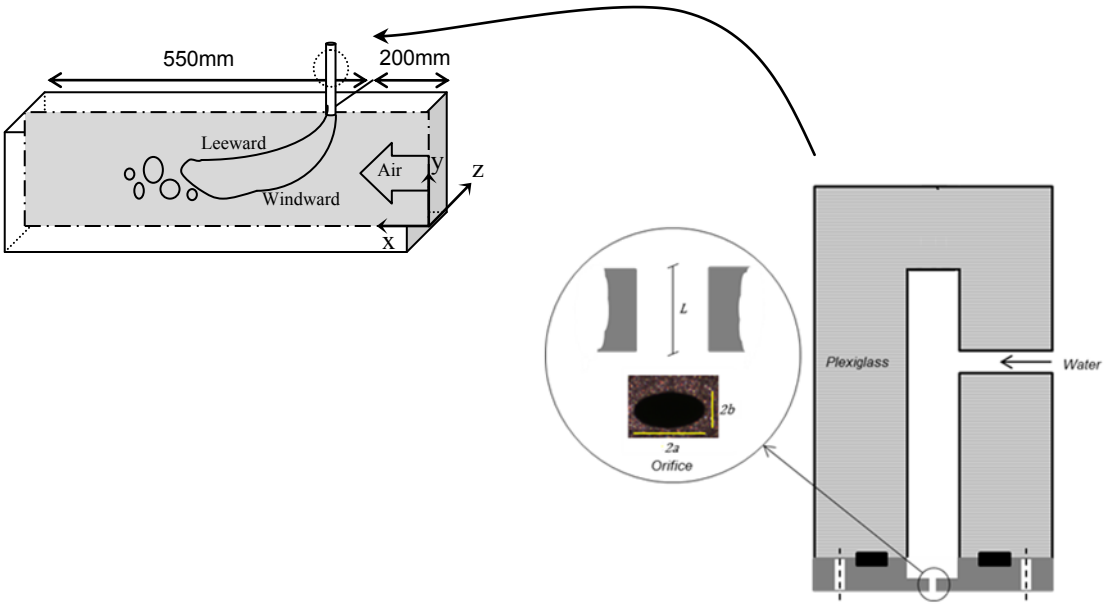


**Figure 5.1 Schematic of the wind tunnel test section and injector**

Shadowgraph technique with a high-speed camera (Photron SA1.1, USA) has been used for capturing images of the spray side view (x–y plane in Figure 5.1). In order to have images with good contrast even for the smallest droplets on the windward edge of the spray, the trajectory was captured at 250 frames per second and the shutter speed was set at 1/593000 sec. With this configuration, 500 images were captured for each test (Figure 5.2 a shows a snapshot of LJICF). In addition, 500 images were captured from the background without any liquid spray. In order to eliminate the background noise from the spray images, and digitizing the images to find the spray windward trajectory, a code was written using the image processing toolbox of MATLAB. The minimum value of each pixel, among 500 background images, creates the background image. The final step in the image processing code is to eliminate the background image from the spray image as shown in Figure 5.2 b.

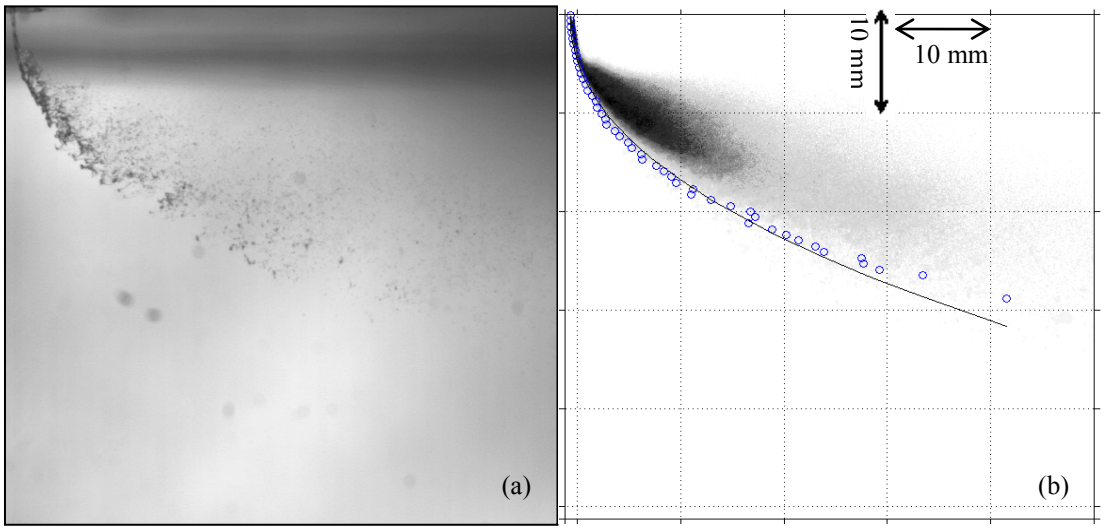


**Figure 5.2 a) A snapshot of liquid spray in crossflow, b) Filtered and averaged image of 500 snapshots**

## 5.3 Boundary Conditions

Several test cases for elliptical jets with the cross section's major axis parallel to the gaseous flow and major axis perpendicular to the gaseous flow are simulated in this study. Figure 5.3 schematically shows the geometry configuration and the top view of different orifices used in this work. As can be seen in this figure, in order to account for the jet ellipticity and its direction with respect to the free stream gas flow, an aspect ratio (*AR*) is defined as the ratio of the jet axis perpendicular to the gas flow to the jet axis parallel to the gas flow. Water is considered as the liquid medium and air is considered as the gaseous flow. The relative gaseous Weber numbers of these cases are 18 or 30 and momentum ratios are 50 and 100, as tabulated in Table 5.1.

**Table 5.1 Simulation parameters**

| | |
|---|---|
| $AR$ | 0.25, 0.33, 0.66, 1, 1.5, 2, 3, 4 |
| $V_g$ (m/s) | 45, 58 |
| $We_g$ | 18, 30 |
| $q$ | 50, 100 |
| $I_g$ | 10% |

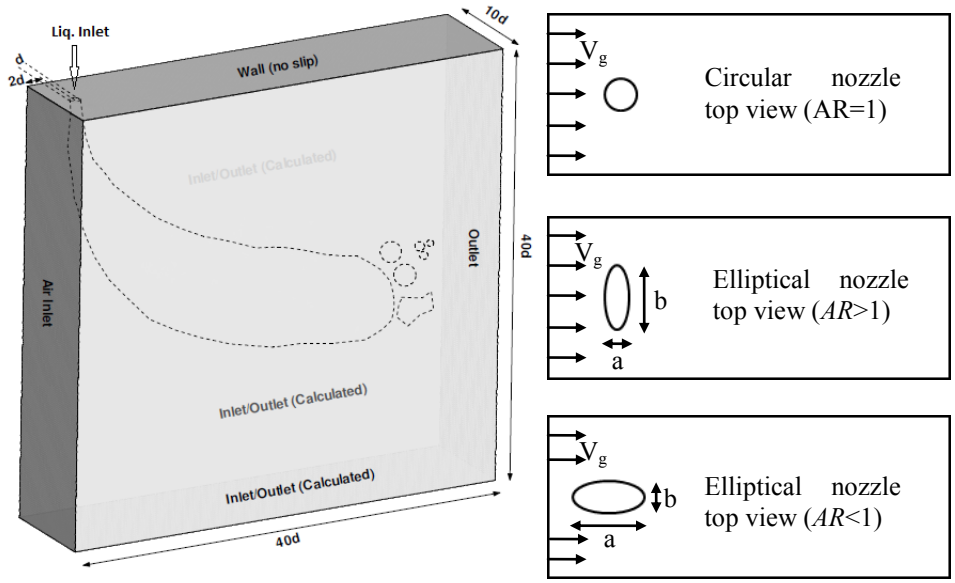


**Figure 5.3 Geometry and top view of different jet configurations (Not to scale)**

## 5.4 Numerical Methodology

The computational fluid dynamics simulation is performed using OpenFOAM code [53]. The solver is an incompressible, three-dimensional, Volume of Fluid (VOF) for two immisible fluids using the MULES (Multidimensional Universal Limiter with Explicit Solution) scheme [55] [73]. Air and liquid with surface tension of 0.0728 N/m are considered Newtonian fluid phase one and two, respectively. Consequently, each cell at any instance has a value of alpha equal to the volume fraction of liquid to gas. For example at the initial time, the value of alpha for the whole domain except the cells on the injector face is zero. The turbulence model used in this study is the Large Eddy Simulation (LES) model using one equation for finding Sub-Grid Scale (SGS) kinetic energy, and a smooth filtering delta coefficient of 1 with maximum delta ratio of 1.1. The gravity force is included in the Navier-Stokes equations. A coupled set of Navier-Stokes equations is solved implicitly by the PISO (Pressure Implicit with Splitting of Operators)

method at each time step. The default time step of $1\times10^{-5}$ s is taken into account with the possibility of adjustments with a Courant number. In this regard, the maximum Courant number which restricts the time step adjustment is 0.5 and the upper limit of the time step is $1\times10^{-5}$ s. Subsequently, the chosen time step is less than $1\times10^{-5}$ s, which facilitates the simulation of even the smallest perturbations on the jet surface and the breakup phenomenon. In terms of the total simulation time, the results serve the simulation of jet evolution through the domain from time zero to 0.1 s. The solution is saved after each $5\times10^{-4}$ s.

A dynamic mesh refinement method is used to solve the liquid flow on a fine mesh to capture the small-scale perturbations on the liquid, while there is no necessity to solve the air on such a fine mesh as the liquid part requires. Thus, the whole mesh is coarse in order to solve the gaseous part, while after each iteration and liquid advancement in the domain, the refinement is solely performed on the cells that contain liquid. The dynamic mesh refinement process is controlled by the value of alpha. Consequently, the cells, which have alpha between 0.001 and 1, inclusively, are refined one level in the x, y and z direction (see Figure 5.4). At the next iteration, again the cells which contain liquid are refined. In this manner, the liquid containing cells become finer at each iteration. However, in order to render the numerical problem timely and cost-effectively, a maximum of three refinement levels for each cell and a limit of 10,000,000 cells for the entire computational domain after each refinement were implemented.

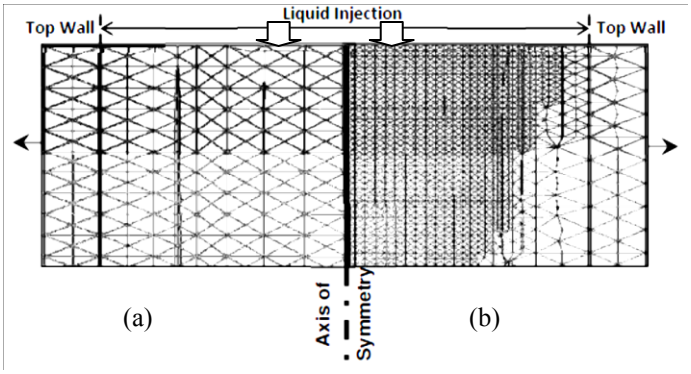


**Figure 5.4 a) Initial mesh, and b) dynamic mesh after 3 level refinements**

Finally, in order to fully exploit the detailed simulations obtained by the VOF-LES solver, the results are post-processed with ParaFoam software [57] and the liquid interface mesh is rendered by Blender open-source software [58].

## 5.5 Results and Discussion

Figure 5.5, shows the iso-surface of liquid volume fraction (α=0.5, as the representative of liquid-gas interface) at a gas Weber number of 35 and momentum flux ratio of 50 for circular and elliptical jets. In addition to the penetration depth and detached ligaments, the unstable waves on the jet windward and leeward surfaces can be clearly identified. It should be noticed that the jet with $AR$ = 1.5 (Figure 5.5b) is deflected more toward the gas flow direction. This is expected since it has a blunter shape at the port of injection and has higher drag, while the jets with $AR$ = 1 and $AR$ = 0.66 have cylindrical and even slimmer shapes respectively and therefore experience smaller drag force.

In general, before fragmentation, the circular jets become blunt and then the droplets shed from the sides, while the jets with AR > 1 already have the blunt shapes right after

the injection. This scenario happens with more delay in the case of jets with AR smaller than one. The first point of droplet separation (fragmentation) from the sides of the jet is shown in Figure 5.5. Apparently, droplets separate earlier from the sides of the elliptical jets with *AR* greater than one. In other words, the jets with *AR* greater than one have a shape closer to liquid sheets compared to the circular nozzle jets, and the jet can disintegrate easier from the sides.

Figure 5.6 shows the jet cross section for various aspect ratios at different locations ($y/d$ = 1 to $y/d$ = 6). As shown in this figure, for cases with $AR < 1$, the jet first shapes itself to the circular form due to surface tension and drag forces. Then in the middle of the way, the sides start to shear away and form a bell-shaped cross section. Consequently, the sides start to disintegrate to form droplets and ligaments. Once again, Figure 5.6 shows that the droplets shedding from the jet sides start earlier in case of elliptical jets with $AR > 1$.

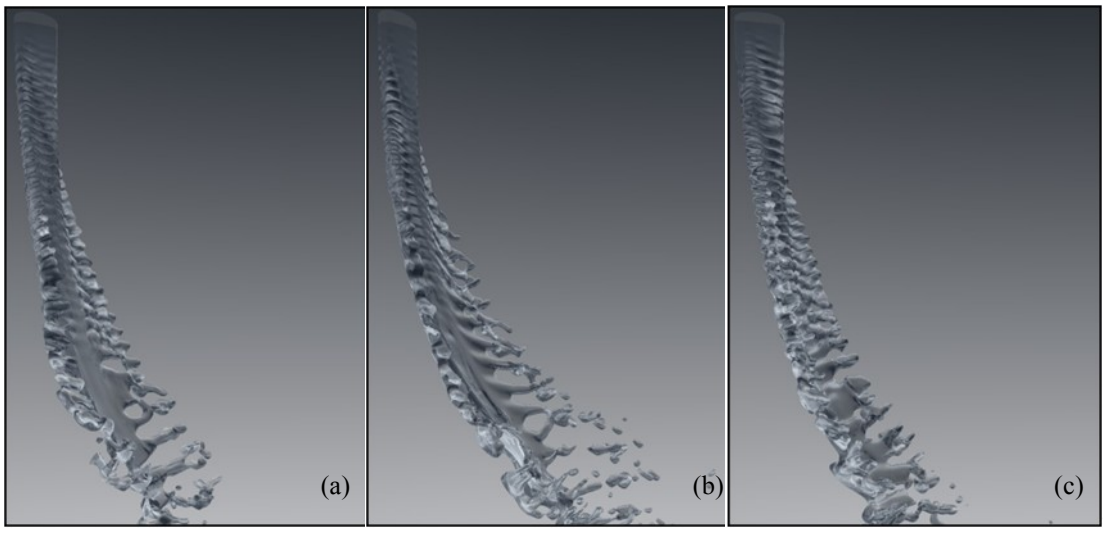


**Figure 5.5 Numerical results of liquid jet in cross flow for $We_g$ = 35 and $q$ = 50, a) circular jet, b) elliptical jet with *AR*=1.5, and c) elliptical jet with *AR*=0.66**

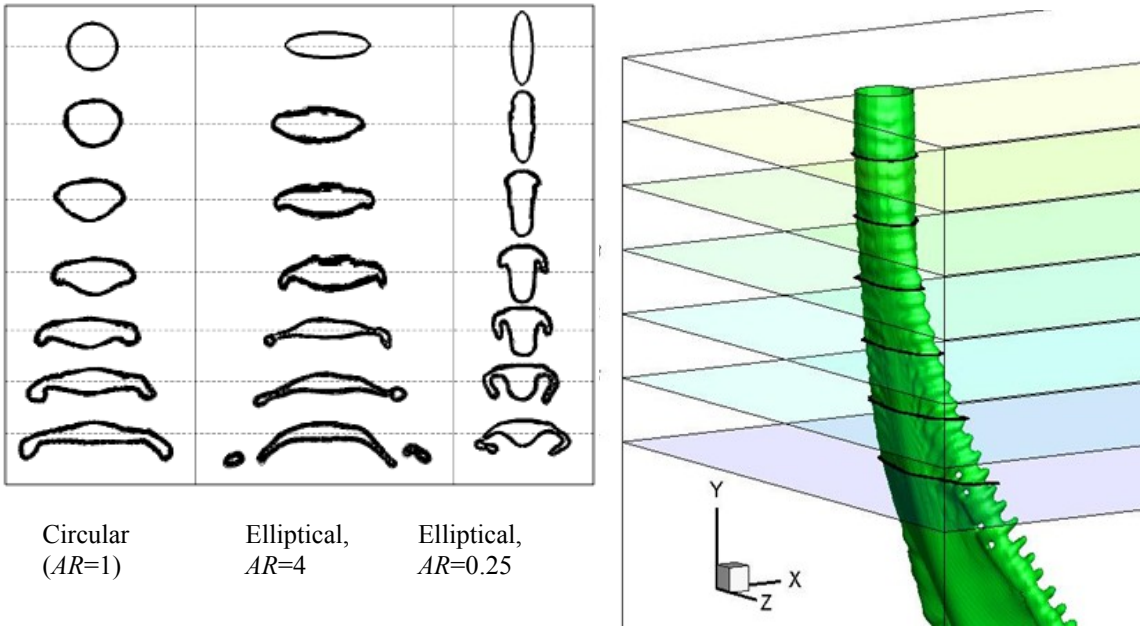


**Figure 5.6 Comparison of jet's cross sections before breakup, $We_g$=30, $q$=50**

Figure 5.7 depicts the windward trajectory of various jets in crossflow at different Weber numbers for a momentum flux ratio of $q$ = 50. The solid lines represent the experimental trajectories of the liquid jets and the marker points represent the numerical simulation results. A good agreement exists between the experimental and numerical results for the cases of this study. It should be mentioned that in addition to the cases presented here (i.e. $We$=18 and 30) the experimental tests are also performed for three other Weber numbers including $We$=5, 10 and 35. At high Weber numbers ($We$>30) or very low Weber numbers ($We$≤10), the experimental and numerical results do not conform well, due to swirling of the jet around itself (in high Weber number cases) or existence of axis switching phenomenon (in low Weber number cases). In other words, in additional experimental test cases, the penetration depth and aspect ratio of the orifice

behave randomly. However in mid range Weber numbers (10<*We*<30), which is mainly addressed in this study, a unique behavior exists between the aspect ratio and the trajectory of a jet, i.e. jet penetration. The higher the aspect ratio, the lower is the penetration of the jet into the gas crossflow. Apparently, this behavior is a result of having wider jet shapes before disintegration and consequently, higher drag for higher aspect ratio jets.

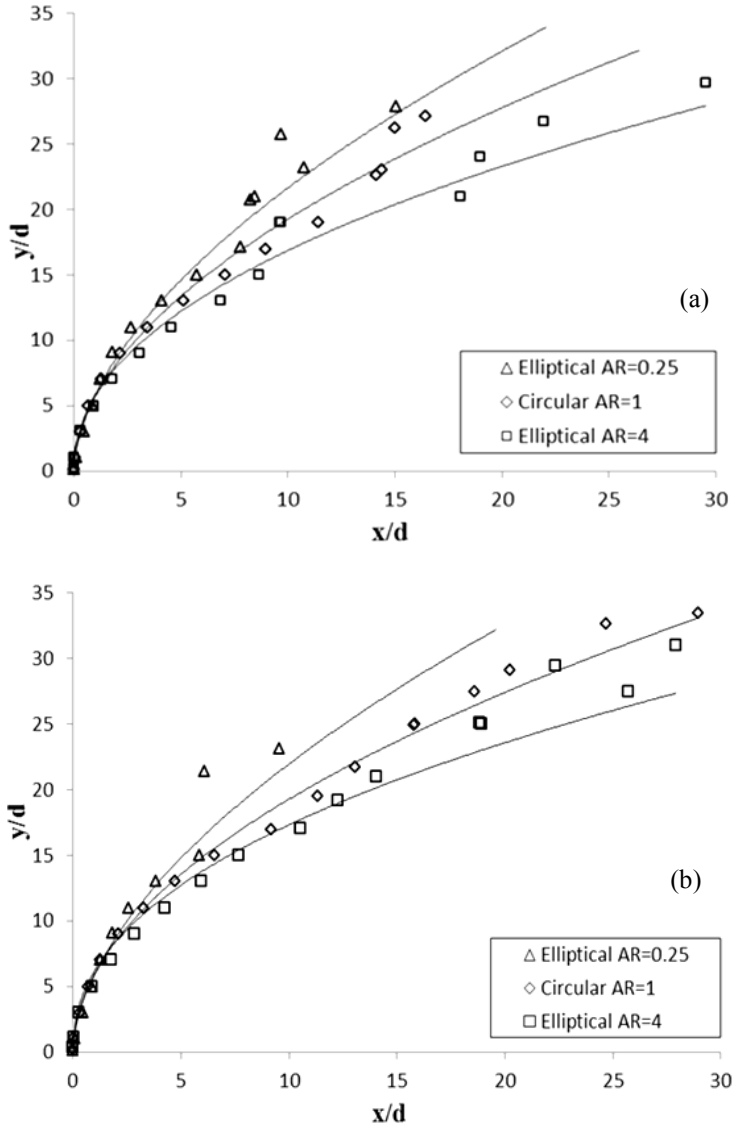


**Figure 5.7 Windward trajectory of liquid jet for elliptical and circular nozzle, a) $We_g$=18, $q$=50 and b) $We_g$=30, $q$=50**

In addition to jet shape and windward trajectory which together represent the jet penetration, one of the main characteristics of any spray is the droplet size distribution. Figure 5.8 shows cumulative volume percent of the droplets versus their diameters. For example, in the circular jet, the droplets with 50% cumulative volume have diameters less than 74 μm. Based on the droplet size distribution, different methods are available in order to find the mean droplet size. Two most useful definitions for the mean droplet size are Mass Median Diameter (MMD) and Sauter Mean Diameter (SMD). The value of MMD, by definition, is the size of droplet such that 50% of total liquid volume is in droplets of smaller diameter. SMD is defined as the sum of the total volume of droplets divided by the sum of total surface of droplets. Having in mind these definitions, Figure 5.8 and Table 5.2 show that the elliptical nozzle with $AR > 1$ has the smallest mean droplet size (MMD), compared to the circular nozzle and the elliptical nozzle with $AR < 1$. Another aspect of this figure is to compare how evenly the droplets are distributed. According to this figure, the jets with higher aspect ratio (e.g. $AR = 4$) have more widely distributed droplet sizes, while the jets with lower aspect ratio (e.g. $AR = 0.25$) have a more slender droplet size distribution with higher peak.

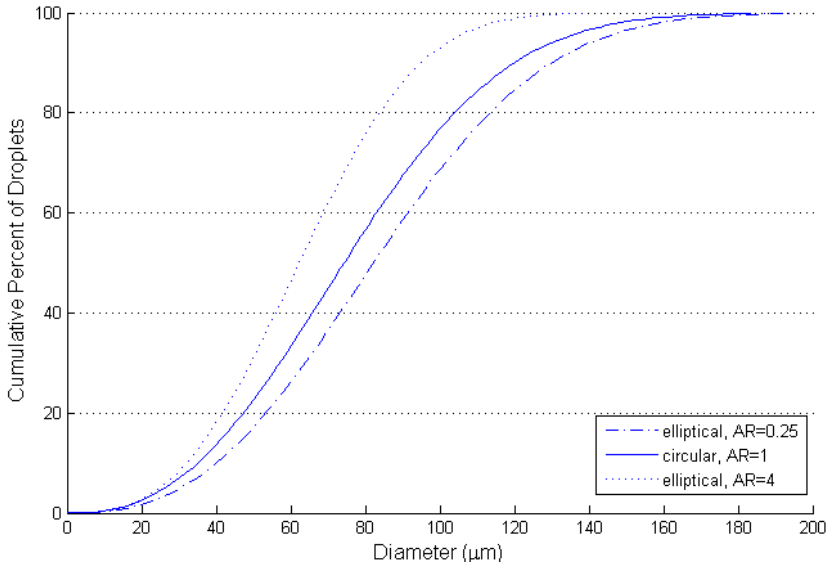


**Figure 5.8 Droplet size distribution of circular and elliptical jets in crossflow (40×diameters downstream of the nozzle), $We_g = 30$, $q = 50$**

**Table 5.2 Mean diameters at $We_g$=30, $q$=50**

| *AR* | SMD, *d32* ($\mu m$) | MMD, *d50* ($\mu m$) |
|---|---|---|
| 0.25 | 65 | 82 |
| 1 | 58 | 74 |
| 4 | 51 | 62 |

One of the important characteristics of a liquid jet in crossflow and its spray is its spreading angle. Simply, it affects the flame fronts in combustion chamber applications or the coverage area in agricultural applications. To this end, in some cases, having the wider spread angle is favorable and in some cases vice versa. Figure 5.9 shows the spread angle for different aspect ratio nozzles as follows. It shows that the circular jet has the widest spread angle compared to the elliptical jets ($AR > 1$ or $AR < 1$); and by increasing or decreasing the aspect ratio from the circular cross section to the elliptical, the spread angle narrows. The reason for this phenomenon can be better understood by considering

the shape of the jet surface shown in Figure 5.6 and the gas flow around it. Apparently, in cases of the elliptical jets, the droplets fragmented from the sides move more in the axial direction.

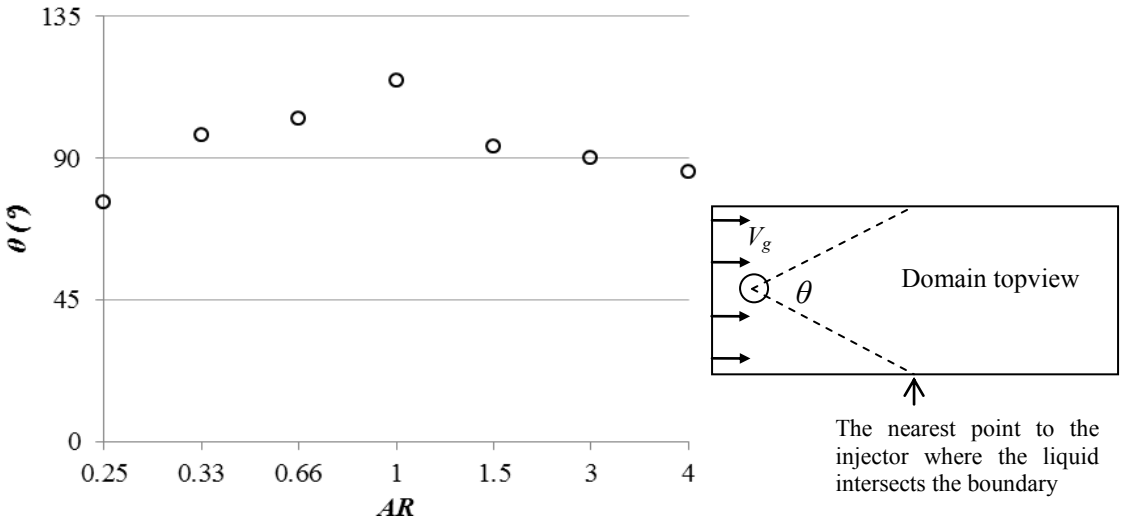


**Figure 5.9 Spray spread angle of circular and elliptical jets for $We_g$ = 30 and $q$ = 50**

## 5.6 Conclusion

Liquid jets in crossflow (LJICF) emanating from orifices with various geometries (i.e. circular and elliptical with various aspect ratios, $AR$ = 0.25–4) are experimentally tested and numerically simulated by the VOF-LES model. The spray characteristics including the windward trajectory, jet's cross section, droplet size distribution and spray spread angle have been compared for different jets at Weber numbers of 18 and 30 and a momentum flux ratio of 50. The results show clear changes in different characteristics of the LJICF. The penetration of the spray in crossflow is decreased by increasing the $AR$, and the droplet mean size also decreases by increasing the $AR$. Furthermore it is

concluded that the circular jet has the widest spreading angle compared to the elliptical ones, no matter the $AR$.

# Chapter 6

# Conclusions and Suggestions for Future Work

## 6.1 Summary

In the first part of this work, biodiesel atomization has been characterized experimentally and numerically. The trajectories, penetration depth, primary breakup, secondary breakup, jet column length, jet column slope, droplet size distribution, droplet velocity and volume flux near the windward position of the spray are obtained and compared experimentally for biodiesel blends and diesel liquid jets traversing subsonic air. The tests are performed for Weber numbers ranging from 10 to 82 and liquid to gas momentum flux ratios between 10 and 133.

The experimental results show lower penetration depth of biodiesel compared to the diesel jet. In other words there is a different breakup regime of biodiesel due to much higher viscosity, which can damp the breakup instabilities considerably. This is clear through the comparison of surface wavelengths produces by biodiesel and diesel. As a consequence of damping the instabilities, biodiesel jet column forms more bag shapes, compared to diesel, even at Weber numbers as high as 80. This behavior is illustrated visually by shadowgraphs, and quantitatively, by increasing the surface wavelengths

along the jet. The bag shape formation at large gas–liquid Weber numbers can raise the drag force on the biodiesel liquid jet column, which results in further deflection of the jet toward downstream. The slope of the liquid jet column for biodiesel and diesel clearly shows this behavior.

Based on the experimental results of shadowgraphs and PDPA, an improved correlation is found for the penetration of biodiesel or any other liquids within the same range of viscosity and surface tension. Within this range the effect of viscosity is more pronounced compared to liquids such as water, diesel and kerosene. In terms of droplet size near the windward locus of the spray, the droplet sizes have the identical distributions and the same value with a variation range of ± 10%. Having the same droplet size and distribution for various blends shows the same spray refinement quality after the secondary breakup, while having different primary breakup and penetration depths. In this vein, it is found that higher concentration biodiesel blends' droplets have lower downstream velocities. This shows that droplets have experienced a lower drag for biodiesel blends, which is due to wider wakes after the biodiesel jet's primary breakup.

Furthermore, the volume flux of biodiesel spray is higher near the windward trajectory compared to that of diesel spray; however a lower volume flux is captured near the leeward trajectory. The cause of this flux distribution, droplet velocity trend and penetration is that the primary breakup regime of high viscosity fuels such as high concentration biodiesel blends totally differs from that of regular fuels such as diesel or kerosene.

Additionally Lagrangian and Eulerian numerical studies are performed in order to find an appropriate model that can simulate biodiesel breakup and can be validated by the

experimental results. Since some differences are found in the biodiesel's trajectory, primary breakup regime and surface waves, the two numerical models are mainly validated to demonstrate these differences accurately.

The results of DPM simulation for diesel match the penetration depth and droplet size distribution; however for biodiesel, the numerical trajectories do not agree well with the experimental tests. In fact, this is due to the nature of discrete phase modeling, where a jet is replaced with a set of droplets and the Taylor Analogy Breakup (TAB) model is used to model the secondary breakups. Since the TAB model simulates the breakup of droplets by a spring-mass equation, viscosity serves as a damper, a role which is not dominant in the spring-mass equation. Therefore for liquids such as biodiesel with very high viscosity, which plays an eminent role in the breakup, the TAB model cannot result in good trajectories. In addition, DPM models a bulk jet as a set of discrete droplets. Therefore the primary breakup that has a crucial role in the biodiesel atomization is not simulated by DPM. As a result, it is concluded that DPM simulation cannot represent the breakup of high viscosity fuels such as biodiesel and its blends.

The other numerical method used to simulate the breakup of B100, B50 and diesel jets in crossflow is a coupled VOF-LES simulation. The numerical results are validated by the same-condition experimental results and show good agreement. The results present lower penetration depth of the biodiesel jet compared to the diesel jet. As expected in the experimental tests, the key to this behavior can be found by calculation of the jet column drag. It is shown, numerically, that the larger drag acting on biodiesel liquid columns causes bending of the jet more toward the downstream. This occurs in a manner such that the diesel jet, owing to smaller drag, penetrates more inside the crossflow of air before

completely bending toward the crossflowing air. Several bag shapes are observed after the primary breakup of biodiesel jets at large Weber numbers for atomization, which argues against the common classification of primary breakup regimes. At the same Weber numbers, diesel shows the multimode or atomization mode of breakup. On the other hand, biodiesel droplets downstream of the domain have lower velocities, which can be as a result of having wider wakes surrounding the biodiesel column. Wider wakes are illustrated in the numerical results for biodiesel compared to diesel. Ultimately, the windward trajectory of VOF-LES simulation is compared with the DPM simulation results. Apparently, the results of VOF-LES seem to be in better agreement with the experimental shadowgraph results, in comparison with the DPM trajectories. This is due to direct modeling of the primary atomization by VOF and also the turbulence flow and its inherent oscillatory behavior, which is captured by LES.

In the latter part of the thesis, elliptical liquid jets are introduced as a means of controlling the liquid atomization process. Since elliptical jets have larger peripheries than the circular jets, they inherently have more instabilities than the conventional circular counterparts. For example, they have an axis-switching phenomenon which shifts the major and minor axes of the elliptical cross section alternately. In this vein, first the elliptical jets' capillary and Rayleigh-Taylor instabilities are characterized without the crossflow effect. These instabilities are simulated using a VOF-LES coupled method with dynamic mesh refinement at each iteration. In order to capture the small internal sources of perturbations, both the liquid interface and liquid filling cells are refined. The axis-switching phenomenon is described by measuring the surface wave growth rate, axis-switching number and liquid jet breakup length. It is observed that the axis-switching

wavelength increases by increasing the liquid jet Weber number. Also at all the simulation conditions, the wavelengths are prolonged monotonically along the jet for low aspect ratio elliptical orifices. On the other hand for high aspect ratio orifices, the wavelengths reach a peak along the jet and then decrease. In general for elliptical orifices, the liquid jet breakup length increases at the Rayleigh regime of breakup, reaches a peak and then decreases drastically at the first wind-induced regime; and following the second wind induced regime, it increases again.

Finally, the liquid jets emanating from an elliptical orifice in gaseous crossflow are compared to circular-orifice jets. The gas–liquid shearing layer, Kelvin-Helmholtz and turbulence instabilities are investigated using a dynamic mesh refinement at the interface. The coupled VOF-LES solver is used in this simulation in order to capture the liquid jet surface instabilities and their effect on the primary breakup. Each elliptical jet in gaseous crossflow may have two possible configurations, one with the major axis parallel to the gas flow direction and the other with the major axis normal to the flow direction. It is found that the elliptical liquid jets with major axis parallel to the flow direction first reach a circular jet cross section then the droplets and ligaments start to shear off the jet surface. Having an additional process of converting elliptical to circular jets just after the exit causes a delay in the atomization process compared to strictly circular ones. Therefore they generally penetrate more than the circular ones. On the other hand, the elliptical jets with major axis normal to the gas flow direction are ahead of the circular jets in terms of being ready to be sheared off from the sides. Therefore their penetrations are generally less than the circular ones. The term “generally” is used, since at some conditions such as high or very low gas–liquid Weber numbers, there are exceptions due

to the meddling of axis-switching instabilities in their primary breakup process. Therefore in general, by using an elliptical orifice instead of a circular orifice, one can control the penetration depth, size of droplets and ligaments and breakup modes of LJICF.

## 6.2 Scope for Research and Future Work

Application of biodiesel fuel as an alternative of diesel, especially for transportation and energy purposes, nowadays is a fast-growing attraction in favor of reducing the dependency on fossil fuels, increasing sustainability and decreasing pollution. Although using biodiesel has several benefits, there are some critiques of its atomization and ignition in combustion chambers. The present thesis serves as a fundamental study of atomization of biodiesel. Various improvements can be suggested as well as deeper and targeted studies. Hence the following is a list of proposed future research.

- *Time-Resolved Shadowgraph Technique:* Due to the restrictions of experimental setup, the shadowgraph images in this study capture a large area of the LJICF, namely 100×100 times the jet diameter. The near field of injection (i.e., 10×10 times the jet diameter), however, can illustrate the liquid surface waves and onset of breakup clearly. In order to study the near field of injection for LJICF, not only is a high-speed camera is required, but also a focused light source is needed that can penetrate through the wind tunnel test section and emit a synchronized light. It is suggested to use a time-resolved laser synchronized with a high-speed camera in order to capture a set of high-quality pictures in a time series.
- *Finding the Liquid Jet Drag by PIV of the Upstream Gas:* In this study, the gas field is characterized by numerical simulation. It is considered that since the

liquid jet trajectory, penetration and surface waves are validated by the experiments, the simulation-obtained drag, gas fields and wakes represent the experiments as well. In fact this should be conveniently proved by having the PIV of gaseous flow upstream of the jet. The study, however, is not straightforward in terms of PIV laser diagnostics, since both liquid jet droplets and gas seeding droplets are present in the wind tunnel test section. It is suggested to use a different material such as very fine sprays of olive oil for the purpose of gas field PIV. In this way, the fine droplets of olive oil can be filtered from the large droplets of liquid jet with different emissivity. PIV laser diagnostics of the gas field just upstream of the liquid jet can verify the hypothesis of having higher drag for the biodiesel jet, as the simulation results depict.

- *Improving the DPM Breakup Model:* It is found that DPM trajectories of diesel agree well with the experimental results, while the biodiesel jet trajectories do not. One of the most important factors in DPM simulation is to find a promising droplet breakup model, since the bulk liquid jet is modeled with a set of discrete droplets at the injector exit. Then the large droplets break up to smaller ones along the spray trajectory. Hence a breakup model such as TAB plays an important role in finding the trajectories. As explained in the preceding chapters, the viscosity force has a crucial role on the primary breakup of biodiesel, while in the TAB model, viscosity is not a dominant term. Therefore some improvements can be performed on modeling of the droplet breakup in DPM. Using the same analogy as the mass-spring system of

TAB, one can improve the damper role and make it more dominant by considering different configurations of the spring-mass system, such as parallel and series. These options, however, should be carefully studied with a set of one-to-one experiments with a needle-suspended droplet in gas crossflow.

- *Hybrid DPM-VOF Simulation:* Although the results of DPM do not match the trajectory of biodiesel well, it can predict the secondary breakup, heat and mass transfer in agreement with experimental results [74] [75]. On the other hand, VOF simulation does not model the heat and mass transfer, although its results are precisely validated with the experimental tests of biodiesel and diesel. Consequently, a hybrid model is proposed to simulate the liquid jet primary breakup by VOF and the secondary breakup, heat and mass transfer by DPM simulation. This new hybrid model has been used in a few other researches recently [44]. The difficulty in these types of hybrid models, though, is to distinguish where the transition from VOF to DPM should be considered. For example, many researchers use the surface-to-volume factor to find the sphericity of the ligaments. If the ligaments are found as small droplets, afterwards the DPM will be taken into account.
- *Ligament Topology:* The liquid segments separated from any LJICF form various shapes of ligaments. The more the ligaments are shaped spherically, the more the effect of the gas–liquid shear force. In other words, the high gas-shear forces dominate the surface tension of a small portion of the liquids on the periphery of the jet. Therefore the breakup happens in a catastrophic form, which shows that the breakup regime is close to the atomization mode. On the

other hand, the more the ligaments are long narrow ones, the more the effect of viscosity on damping the surface tension force. In other words, the breakup regime is close to bag-multimode regimes of breakup. Hence it is suggested to have a stereoscopic time-resolved shadowgraphy together with a very refined numerical VOF-LES modeling in order to capture the ligament topologies.

- *Biodiesel Atomization in a Pressure Swirl Atomizer:* Pressure swirl atomizers are one of the most common atomizers in industrial applications such as gas turbines engines. In these atomizers, the liquid forms a swirling thin film in a confined environment. The swirling film then exits the atomizers and converts to fine droplets in a coflow or crossflow ambient gas. The effect of swirl and thin film on the liquid breakup completely changes the breakup behavior. It is suggested to study the atomization of biodiesel in those types of atomizers both numerically and experimentally.

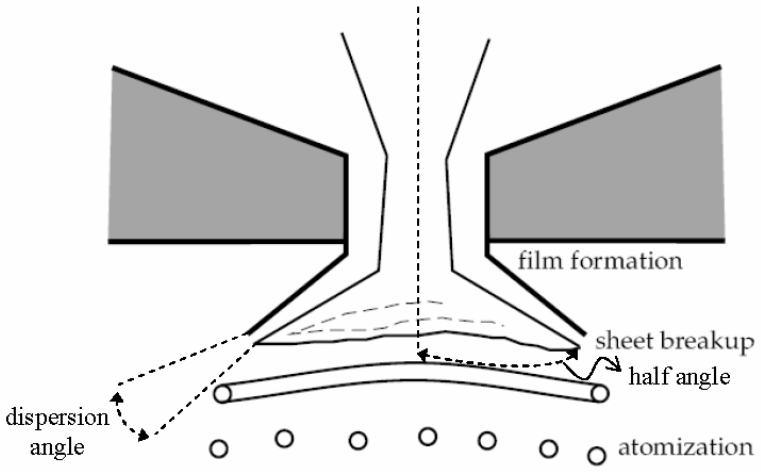


**Figure 6.1 Pressure swirl atomizer [76]**

- *Capturing Satellite Droplets from an Elliptical Free Jet:* The experimental results of free liquid jets from an elliptical nozzle sometimes show some small-diameter droplets between each pair of large droplets in the capillary-Rayleigh regimes of breakup [21]. These droplets are called Satellite droplets; they form in such a manner that the VOF-LES simulations in this thesis did not capture any. It is suggested to use different refinement techniques or other interface tracking methods (e.g. the octree method) to capture the satellite droplets.
-

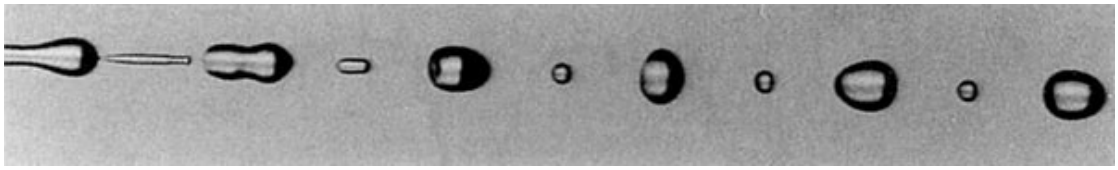

**Figure 6.2 Satellite droplet formation [77]**

- *Extensive Study of Elliptical LJICF:* In this thesis, the elliptical liquid jets in crossflow are studied for a limited range of Weber number, momentum flux ratios and liquid materials. The shadowgraph images for few cases out of this range show complicated behaviors. Especially the axis-switching phenomenon in some Weber ranges adds to this complexity. For example in some tests, it is observed that when the major axis of the ellipse is perpendicular to the flow direction, the liquid jet starts to swirl due to drag force. This swirling phenomenon happens at low (We = 10) or high Weber numbers (82), while the intermediate results do not show this behavior. Consequently, a near field study of elliptical jets in crossflow is a valuable research scope for further investigations.

# 7 Bibliography


[1] A. Demirbas, "Political, economic and environmental impacts of biofuels: A review," *Applied Energy,* vol. 86, pp. S108-S117, 2009.

[2] Z. Specht, "Biofuels History and Review," San Diego State University, San Diego, CA, 2011.

[3] Biofuels.org.uk, "History of Biofuels," 2010. [Online]. Available: http://biofuel.org.uk/history-of-biofuels.html. [Accessed 01 04 2013].

[4] D. Hammes and D. Wills, "Black Gold: The End of Bretton Woods and the Oil-Price Shocks of the 1970s," *The Independent Review,* vol. 9, no. 4, pp. 501-511, 2005.

[5] Wikipedia, "Biofuel, Wikipedia," 2013. [Online]. Available: http://en.wikipedia.org/wiki/Biofuel#First-generation_biofuels. [Accessed 18 07 2013].

[6] N. National Biodiesel Board, "Home: Biodiesel.org," 2013. [Online]. Available: http://biodiesel.org/what-is-biodiesel/biodiesel-basics. [Accessed 18 07 2013].

[7] A. Demirbas, Biodiesel, A Realistic Fuel Alternative for Diesel Engines, London, UK: Springer, 2008.

[8] F. Ma and M. A. Hanna, " Biodiesel production: a review," *Bioresource Technology,* vol. 70, pp. 1-15, 1999.

[9] G. Knothe, C. A. Sharp and T. W. Ryan, "Exhaust Emissions of Biodiesel, Petrodiesel, Neat Methyl Esters, and Alkanes in A New Technology Engine," *Energy Fuels,* vol. 20, pp. 403-408, 2006.

[10] S. M. Mudge and G. Pereira, "Stimulating the biodegradation of crude oil with biodiesel: preliminary results," *Spill Sci Technol Bull,* vol. 5, pp. 353-355, 1999.

[11] H. K. Speidel, R. L. Lightner and I. Ahmed, "Biodegradability of new engineered fuels compared to conventional petroleum fuels and alternative fuels in current use," *Appl Biochem Biotechnol ,* Vols. 84-86, pp. 879-897, 2000.

[12] M. Mittelbach and C. Remschmidt, "Biodiesels–The Comprehensive Handbook," Karl-Franzens University, Graz, Austria, 2004.

[13] G. Knothe, J. Krahl and J. Van Gerpen, "The Biodiesel Handbook," AOCS Press, Chicago, IL, 2005.

[14] W. Ohnesorge, "Formation of Drops by Nozzles and the Breakup of Liquid Jets," *Z. Angew. Math. Mech.,* vol. 16, pp. 355-358, 1936.

[15] L. Rayleigh, "On the Capillary Phenomena of Jets," *Proc. R. Soc.,* vol. 29, pp. 71-97, 1879.

[16] C. Z. Weber, "On the Breakdown of A Liquid Jet," *Z. Angew Math. Mech.,* vol. 11, pp. 136-154, 1931.

[17] G. I. Taylor, "Generation of ripples by wind blowing over viscous fluids," in *The Scientific Papers of G.I. Taylor*, Batchelor, Ed., Cambrige, UK, Cambrige University Press, 1971.

[18] R. D. Reitz and F. V. Bracco, "Mechanisms of breakup of round liquid jets," *Encyclopedia of Fluid Mechanics,* vol. 3, pp. 233-249, 1986.

[19] C. C. Miesse, "Correlation of Experimental Data on the Disintegration of Liquid Jets," *Industrial Engineering Chemistry,* vol. 47, p. 1690–1695, 1955.

[20] C. Dumouchel, "On the Experimental Investigation on Primary Atomization of Liquid Streams," *Exp. Fluids,* vol. 45, pp. 371-422, 2008.

[21] G. Amini, Instability of Elliptic Liquid Jets, Montreal, QC: Concordia University, 2011.

[22] K. A. Sallam, C. Aalburg and G. M. Faeth, "Breakup of Round Nonturbulent Liquid Jets in Gaseous Crossflow," *AIAA J.,* vol. 42, pp. 2529-2540, 2004.

[23] A. Belfiore, "Experimental and Numerical Study of Liquid Jets Injected in High Density Air Crossflow," University of Naples Federico II, Naples, Italy, 2006.

[24] S. N. Marzbali, "Penetration of Circular and Elliptical Liquid Jets into Gaseous Crossflow: A Combined Theoretical and Numerical Study," Concordia University, Montreal, QC, 2011.

[25] O. M. Elshamy, "Experimental Investigations of Steady and Dynamic Behavior of Transverse Liquid Jets," in *PhD Dissertation*, Cincinnati, OH, University of Cincinnati, 2006.

[26] H. S. Husain and F. Hussain, "Elliptic Jets. Part3: Dynamics of Preferred Mode Coherent Structure," *J. Fluid Mech.,* vol. 248, pp. 315-361, 1993.

[27] J. Song, K. K. M. K. Ahn and Y. Yoon, "The Spray Plume Characteristics of Liquid Jet in Subsonic Crossflow," *Proceedings of 43rd AIAA/ASME/SAE/ASEE Joint Propulsion Conference,* pp. 3976-3983, 2007.

[28] G. I. Taylor, "Formation of thin flat sheets of water," *Proceedings of Royal Society of London,* vol. 259, pp. 1-17, 1960.

[29] T. V. Kasyap, D. Sivakumar and B. N. Raghunandan, "Flow and Breakup

Characteristics of Elliptical Liquid Jets," *Int. J. Multip. Flow,* vol. 35, pp. 8-19, 2009.

[30] A. K. Agarwal, "Biofuels (alcohols and biodiesel) Applications as Fuels for Internal Combustion Engines," *Prog. in Energy and Combstion Science,* vol. 33, pp. 233-271, 2007.

[31] J. P. Szybista, J. Songa, M. Alama and A. L. Boehman, "Biodiesel Combustion, Emissions and Emission Control," *Fuel Proc. Tech.,* vol. 88, pp. 679-691, 2007.

[32] J. A. Schetz and A. Padhye, "Penetration and Breakup of Liquids in Subsonic Airstreams," *AIAA Journal,* vol. 15, pp. 1385-1390, 1977.

[33] P. K. Wu, K. A. Kirkendall, R. P. Fuller and A. S. Nejad, "Breakup Processes of Liquid Jets in Subsonic Crossflows," *J. Prop. and Power,* vol. 13, pp. 64-73, 1997.

[34] P. K. Wu, K. A. Kirkendall, R. P. Fuller and A. S. Nejad, "Spray Structures of Liquid Jets Atomized in Subsonic Crossflows," *J. Prop. and Power,* vol. 14, pp. 173-182, 1998.

[35] P. K. Wu, L. K. Tseng and G. M. Faeth, "Primary Breakup in Gas/Liquid Mixing Layers for Turbulent Liquids," *Atomization and Sprays,* vol. 2, pp. 295-317, 1992.

[36] J. Becker and C. Hassa, "Breakup and Atomization of a Keroscene Jet in Crossflow at Elevated Pressure," *Atomization and Sprays,* vol. 11, pp. 49-67, 2002.

[37] C. O. Iyogun, M. Birouk and N. Popplewell, "Trajectory of Water Jet Exposed to Low Subsonic Crossflow," *Atomization and Sprays,* vol. 16, pp. 963-979, 2006.

[38] J. Stenzler, J. G. Lee, D. Santavicca and W. Lee, "Penetration of Liquid Jets in A Crossflow," *Atomization and Sprays,* vol. 16, pp. 887-906, 2006.

[39] J. Mazallon, Z. Dai and G. M. Faeth, "Primary Breakup of Nonturbulent Round Liquid Jets in Gas Crossflows," *Atomization and Sprays,* vol. 9, pp. 299-311, 1999.

[40] M. Birouk, B. Azzopardi and T. Stabler, "Primary Break Up of A Viscous Liquid Jet in a Cross Airflow," *Particle and Particle Systems Characterization,* vol. 20, pp. 283-289, 2003.

[41] M. Birouk, C. O. Iyogun and N. Popplewell, "Role of Viscosity on Trajectory of Liquid Jets in A Cross Airflow," *Atomization and Sprays,* vol. 17, pp. 267-287, 2007.

[42] R. K. Madabhushi, "A Model for Numerical Simulation of Breakup of A Liquid Jet in Crossflow," *Atomization and Sprays,* vol. 13, pp. 413-424, 2003.

[43] C. L. Ng, K. A. Sallam, H. M. Metwally and C. Aalburg, "Deformation and Surface Waves Properties of Round Nonturbulent Liquid Jets in Gaseous Crossflow," Houston, TX, 2005.

[44] M. Hermann, "Detailed Numerical Simulations of the Primary Atomization of a Turbulent Liquid Jet in Crossflow," *ASME J. Eng. Gas Turb. Power,* vol. 132, p. 061506, 2010.

[45] M. Hermann, "The Impact of Density Ratio on the Liquid Core Dynamics of a Turbulent Liquid Jet Injected Into a Crossflow," *ASME J. Eng. Gas Turb. Power,* vol. 133, p. 061501, 2011.

[46] M. G. Pai, H. Pitsch and O. Desjardins, "Detailed Numerical Simulations of Primary Atomization of Liquid Jets in Crossflow," Orlando, FL, 2009.

[47] A. Amighi, M. Eslamian and N. Ashgriz, "Trajectory of a Liquid Jet in High

Pressure and High Temperature Subsonic Air Crossflow," Vail, CO, 2009.

[48] L. Araneo, V. Soare, R. Payri and J. Shakal, "Setting up A PDPA System for Measurements in A Diesel Spray," *J. Phys.: Conf. Ser.,* vol. 45, pp. 85-93, 2006.

[49] L. Schumacher, "The Physical and Chemical Characterization of Biodiesel Low Sulfur Blends," University of Missouri, Missouri, MO, 1995.

[50] A. Ahmed, C. E. Ejim, B. A. Fleck and A. Amirfazli, "Effect of Biodiesel Fuel Properties and Its Blends on Atomization," in *SAE World Congress*, Detroit, MI, 2006.

[51] E. Farvardin, M. Johnson, H. Alaee, A. Martinez and A. Dolatabadi, "Comparative Study of Biodiesel and Diesel Jets in Gaseous Crossflow," *Journal of Propulsion and Power,* In Press, p. B34743, 2013.

[52] R. Scardovelli and S. Zaleski, "Direct Numerical Simulation of Free-Surface and Interfacial Flow," *Annual Review of Fluid Mechanics,* vol. 31, pp. 567-603, 1999.

[53] ESI-OpenCFD, "Home OpenFOAM," 2012. [Online]. Available: http://www.openfoam.com. [Accessed 1 April 2013].

[54] A. Yoshizawa and K. Horiuti, "A Statistically-Derived Sub-Grid Scale Model for the Large Eddy Simulation of Turbulent Flows," *J. of the Physical Society of Japan,* vol. 54, pp. 2834-2839, 1985.

[55] H. Rusche, Computational Fluid Dynamics of Dispersed Two Phase Flows at High Phase Fractions, London: Imperial College University of London, 2002.

[56] N. Spyrou, D. Choi, A. Sadiki and J. Janicka, "Large Eddy Simulation of the Breakup of a Kerosene Jet in Crossflow," Tampa, FL, 2010.

[57] Kitware, "Home Paraview," 2012. [Online]. Available: http://www.paraview.org. [Accessed 01 04 2013].

[58] F. Blender, "Home Blender.org," 2012. [Online]. Available: http://www.blender.org. [Accessed 01 04 2013].

[59] E. Farvardin, M. Johnson, P. Q. Gauthier and A. Dolatabadi, "Comparative Study of Penetration of Biodiesel and Diesel Jets in Gaseous Crossflow," Winnipeg, MB, 2011.

[60] G. Amini and A. Dolatabadi, "Axis-Switching and Breakup of Low-Speed Elliptic Liquid Jets," *Int. J. of Multiphase Flow,* vol. 42, pp. 96-103, 2012.

[61] Y. F. Dityakin, "On the Stability and Breakup Into Drops of A Liquid Jet of Elliptical Cross Section," *Izv. Akad. Nauk SSSR, Otdel. Tekhn Nauk,* vol. 10, pp. 124-130, 1954.

[62] S. E. Bechtel, "The Oscillation of Slender Elliptical Inviscid and Newtonian Jets: Effects of Surface Tension, Inertia, Viscosity and Gravity," *J. Applied Mechanics,* vol. 56, pp. 968-974, 1989.

[63] S. E. Bechtel, M. G. Forest, D. D. Holm and K. J. Lin, "1-D Closure Models for 3-D Incompressible Viscoelastic Free Jets: Von Karman Flow Geometry and Elliptical Cross Section," *J. Fluid Mech.,* vol. 196, pp. 241-262, 1988.

[64] D. A. Caulk and P. M. Naghdi, "The Influence of Twist on the Motion of A Straight Jet," Univ. Calif., Berkeley, Dep. Mech. Eng., Berkeley, CA, 1977.

[65] G. Amini and A. Dolatabadi, "Capillary Instability of Elliptic Liquid Jets," *Physics of Fluids,* vol. 23, p. 084109, 2011.

[66] D. A. Caulk and P. M. Naghdi, "On the Onset of Breakup in Inviscid and Viscous Jets," *J. Applied Mechanics,* vol. 46, pp. 291-297, 1979.

[67] E. F. Brown and J. P. Boris, "A Numerical Simulation of Circular and Elliptic Free Jets," New York, NY, 1990.

[68] R. S. Miller, C. K. Madnia and P. Givi, "Numerical Simulation of Non-Circular Jets," *Computers & Fluids,* vol. 24, pp. 1-25, 1995.

[69] Y. Pan and K. Suga, "A Numerical Study of The Breakup Process of Laminar Liquid Jets into A Gas," *Phys. Fluids,* vol. 18, pp. 1-11, 2006.

[70] R. D. Reitz, Atomization and other breakup regimes of a liquid jet, Princeton, NJ: Princeton University, 1978.

[71] J. Geer and J. C. Strikwerda, "Vertical Slender Jets with Surface Tension," *J. Fluid Mech.,* vol. 135, pp. 155-169, 1983.

[72] N. Bohr, "Determination of Dynamic Surface Tension by The Method of Jet Vibration," *Philos. Trans. Roy. Soc. Lond.,* vol. 209, pp. 281-317, 1909.

[73] S. Zalesak, "Fully Multidimensional Flux-Corrected Transport Algorithms for Fluids," *Journal of Computational Physics,* vol. 31, pp. 351-362, 1979.

[74] E. Farvardin, O. Stier, V. Luthen and A. Dolatabadi, "Effect of Liquid Feedstock in A High Pressure Cold Spray Nozzle," *Journal of Thermal Spray Technology,* Vols. 1-2, pp. 307-316, 2011.

[75] E. Farvardin, O. Stier, V. Luthen and A. Dolatabadi, "Effect of Liquid Feedstock in A High Pressure Cold Spray Nozzle," Boucherville, QC, 2010.

[76] Ansys, "Documentation, Ansys-Fluent," 2013. [Online]. Available:

http://www.ansys.com/Support/Documentation. [Accessed 20 07 2013].

[77] P. Vassallo and N. Ashgriz, "Satellite formation and merging in liquid jet breakup," *Proceedings of Royal Society of London,* vol. A433, pp. 269–286, 1991.

[78] E. Farvardin and A. Dolatabadi, "Numerical Simulation of Breakup of Elliptical Liquid Jet in Still Air," *ASME Journal of Fluids Engineering,* FE12-1515, 2013.

[79] E. Farvardin and A. Dolatabadi, "Simulation of Biodiesel Jet in Crossflow," *Atomization and Sprays,* under review, 2013.

[80] E. Farvardin and A. Dolatabadi, "Simulation of Biodiesel Jet in Crossflow," Heidelberg, Germany, 2012.

[81] E. Farvardin and A. Dolatabadi, "Numerical Simulation of Breakup of Elliptical Liquid Jet in Still Air," Rio Grande, PR, 2012.

[82] E. Farvardin and A. Dolatabadi, "Breakup Simulation of Elliptical Liquid Jet in Gaseous Crossflow," New Orleans, LA, 2012.

[83] E. Farvardin and A. Dolatabadi, "Primary Breakup Simulation of Biodiesel Jet in Gaseous Crossflow," Toronto, ON, 2012.

[84] A. Dolatabadi, B. Samareh and E. Farvardin, "Simulation of Cold Spray Process: A Comparative Study of Particle Drag Laws," Windsor, ON, 2011.

[85] A. Dolatabadi, E. Farvardin and B. Samareh, "CFD Modeling and Flow Visualization in Cold Spray Process," Boucherville, QC, 2010.

[86] E. Farvardin and A. Dolatabadi, "Breakup of Elliptical Liquid Jet in Gaseous Crossflow," *Atomization and Sprays,* to be submitted, 2013.